Hybrid Switch Reluctance Drives For Pump Applications

Jakobsen, Uffe

Publication date:
2011

Document Version
Publisher's PDF, also known as Version of record

Hybrid Switch Reluctance Drives For Pump Applications

Uffe Jakobsen

AALBORG UNIVERSITY

SMEDEGAARD OF DENMARK

Preface

This thesis is written under the framework of the Danish PhD Research school EnergyLab DK. The research project was carried out under the supervision of Associate Prof. Peter Omand Rasmussen and Associate Prof. Kaiyuan Lu from Department of Energy Technology (DET) at Aalborg University; and respectively MSc.EE. Jan L. Mose from T.Smedegaard A/S. My gratitude goes to my steering committee for their guidance and professional support during the work on this thesis. I would like to thank to Kurt Haller of T.Smedegaard for providing the important assistance with the manufacturing of the prototypes used for this project, absolutely necessary for the experimental tests. Similarly a thank you should go to Densit ApS for the excellent concrete used in this project, as well as a thank you to AAG Aalborg Gummivarefabrik A/S for some EPDM used in the tests. I would like to express my sincere thanks to Prof. Ahn from Kyungsung University, Korea for all the professional support he gave during my stay in Korea. Special thanks for all my colleges from DET for their friendly companionship, espe- cially to Dezso Sera, Mihai Ciobotaru, RamKrishan Maheshwari, Tamas Kerekes, László Máthé, Torben Matzen, Erik Schaltz, Søren Juhl Andreasen , Yash Veer Singh and Unnur Stella Gudmundsdottir. Honourable mention goes to D.D.Å.

Ishøj, 10. September, 2011

Uffe Jakobsen

Abstract

The initial research problem is to investigate an alternative motor drive to the existing permanent magnet synchronous and brushless DC-motor drives for pump applications. A review of different motor types showed that a possible candidate for another low cost permanent magnet motor may be the single phase hybrid switched reluctance motor (HSRM). Due to the simple construction of the single phase HSRM, manufacturing may be simplified compared to a three phase permanent magnet motor and consumption of copper may be lowered when compared to both the induction motor and some three phase permanent magnet motors.

The focus of this thesis is regarding the design and control of a single phase hybrid switched reluctance motor (HSRM) intended to drive e.g. a centrifugal pump. A single phase hybrid switched reluctance motor was designed with a novel stator pole shaping method and a new arrangement of permanent magnets for flux concentration was presented. It was shown how stator pole shaping can improve starting torque for a single phase hybrid switched reluctance motor. It was demonstrated that the configuration of permanent magnets in different flux concentration arrangements influences the shape and magnitude of the torque. This first prototype is used for most of the experiments presented in the thesis. The motor achieves an efficiency of close to 77% at an output power of 72 W, comparable to a BLDC or PMSM in a similar power range.

An alternative speed control method suitable for control of motor drives with a high periodic torque ripple is used to control the HSRM. The torque of a single phase HSRM has a non-linear dependency on both current and the angle, where active torque control is not possible for the entire stroke. The torque produced has a periodic ripple, with a period of four times the rotational frequency, which is also giving a periodic ripple in the speed. This speed ripple may

affect the input to a time invariant speed controller if it is not low pass filtered. If the speed controller updates are also not synchronized with the strokes, the speed controller outputs may change during a stroke. The changes of speed controller output during a stroke, may give rise to undesired low frequency oscillations in the speed controller output. A time variant speed controller is presented in the thesis that does not suffer from these issues.

Like the brushless DC-motor (BLDC) and the permanent magnet synchronous motor (PMSM), the HSRM needs information about rotor position to be properly controlled. For BLDC, PMSM, induction motors, and the normal SRM position sensorless methods are relatively well established and have been used for some time. For the single phase switched reluctance motor several methods have been used, however for the single phase hybrid switched reluctance motor there seems to be no known methods. The presented position sensorless method is simple, robust towards parameter changes and thus suitable for implementation in a mass produced low cost drive.

A method to protect windings in a HSRM, flooded with boiling water, is also presented but has yet to be tested for its lifetime performance.

Dansk resumé

Emnet for afhandlingen er at undersøge en alternativ motor til eksisterende permanent magnet synkron motorer og børsteløs DC-motorer som centrifugalpumpemotor. En gennemgang af forskellige motortyper viste, at en mulig kandidat til en lav pris permanent magnet motor kan være den enfasede hybrid reluktans motor (HSRM). På grund af den enkle konstruktion af den enfasede HSRM, kan fremstilling være forenklet i forhold til et trefaset permanent magnet motor og forbruget af kobber kan sænkes i forhold til både induktionsmotorer og nogle trefasede permanent magnet motorer.

Fokus i denne afhandlinger på design og kontrol af enfasede hybrid reluktans motorer (HSRM), der har til formål at drive blandt andet en centrifugalpumpe. En enfaset hybrid reluktans motor er designet med en speciel statorpolsudformning og en indretning af permanente magneter til flux koncentration. Det blev vist hvordan statorpolformen kan forbedre startmomentet for en enfaset hybrid reluktans motor. Det blev demonstreret, at konfigurationen af permanente magneter i forskellige flux koncentration arrangementer påvirker formen og størrelsen af drejningsmomentet. Denne første prototype motor bruges til de fleste af forsøgene præsenteres i specialet. Motoren opnår en virkningsgrad på tæt ved 77% ved en udgangseffekt på 72 W, kan sammenlignes med en BLDC eller PMSM i et lignende effektområde.

Alternative hastighedskontrolmetoder egnet til styring af motordrev med stor periodisk variation i drejningsmomentet blev udviklet og brugt til at styre HSRM. Det producerede motormoment er periodisk, med en periode på fire gange rotationsfrekvensen, som også giver en periodisk variation i rotorhastigheden. Periodiske hastighedsvariationer i indgangssignalet til en tidsinvariant hastighedsregulator kan give anledning til uønskede lavfrekvente svingninger i hastighedsregula-

torens output, hvis dette indgangssignal ikke lavpas filtreres. Tidsvariante hastighedsregulatorer præsenteres, der ikke behøver en sådan lavpas filtrering.

Ligesom en børsteløs DC-motor (BLDC) og permanent magnet synkron motor (PMSM) er der behov for HSRM oplysninger om rotorpositionen, hvis HSRM skal kontrolleres korrekt. For BLDC er PMSM, asynkronmotorer, og den normale SRM er positionssensorløse metoder relativt veletablerede og har været brugt i nogen tid. For enfasede reluktans motorer har flere metoder allerede været brugt, men for den enfasede hybride reluktans motor synes der ikke at være nogle kendte metoder. Den præsenterede positionssensorløse metode er enkel, robust over for parameter ændringer og dermed egnet til implementering i et masse produceret motordrev.

En metode til at beskytte viklingerne i en HSRM oversvømmet med kogende vand er også præsenteret, men mangler endnu at blive testet for levetid.

Contents

Part I - Preliminaries

Chapter 1

Introduction

The focus of this thesis is regarding the design and control of a single phase hybrid switched reluctance motor (HSRM) intended to drive a small centrifugal pump. Approximately 75% of electrical drives in U.S.A. are uni-directional drives such as pump-, fan-, and compressor-type drives [1]. For low power uni-directional drives, the two phase induction motor has long been the preferred motor[2] along with the universal motor. To increase efficiency, three phase permanent magnet motors may be used as replacement for the induction motor in pump applications[3]. The initial research problem is to investigate an alternative motor drive to the existing permanent magnet synchronous and brushless DC-motor drives for pump applications. A review of different motor types showed that a possible candidate for another low cost permanent magnet motor may be the single phase hybrid switched reluctance motor (HSRM). Due to the simple construction of the single phase HSRM, manufacturing may be simplified compared to a three phase permanent magnet motor and consumption of copper may be lowered when compared to both the induction motor and some three phase permanent magnet motors. The cost and complexity of the needed electronic control is assumed to be of a similar to the cost and complexity of a brushless DC-motor drive.

To achieve lower cost, several aspects are considered in this thesis: reduction in sensor requirements by developing a position sensorless control, a lower cost alternative to protect the windings of the motor from water, a motor design that can use simple coils for the windings and thus use

less copper than an existing induction motor drive, a motor design that has full torque during start up also when running position sensorless.

More information regarding the background and motivation for the project is presented in the following sections. This is followed by a short introduction to the hybrid switched reluctance motor. The scope of the thesis is also defined and an outline of the thesis finishes the chapter.

1.1 Pump Motor Drives

A pump motor drive is in this thesis defined to consist of an impeller, a pump housing, and an electrical motor with suitable drive electronics and control. This thesis only focuses on the electrical motor and its control. Varying the speed allows for significant energy savings [4], and thus it is in the following assumed that electronic control is required. The classical approach is to control the torque of a motor is by controlling the current, since the current directly is linked to the torque production. A variable speed pump drive, without drive electronics, may be composed of the components shown in Fig. 1.1.

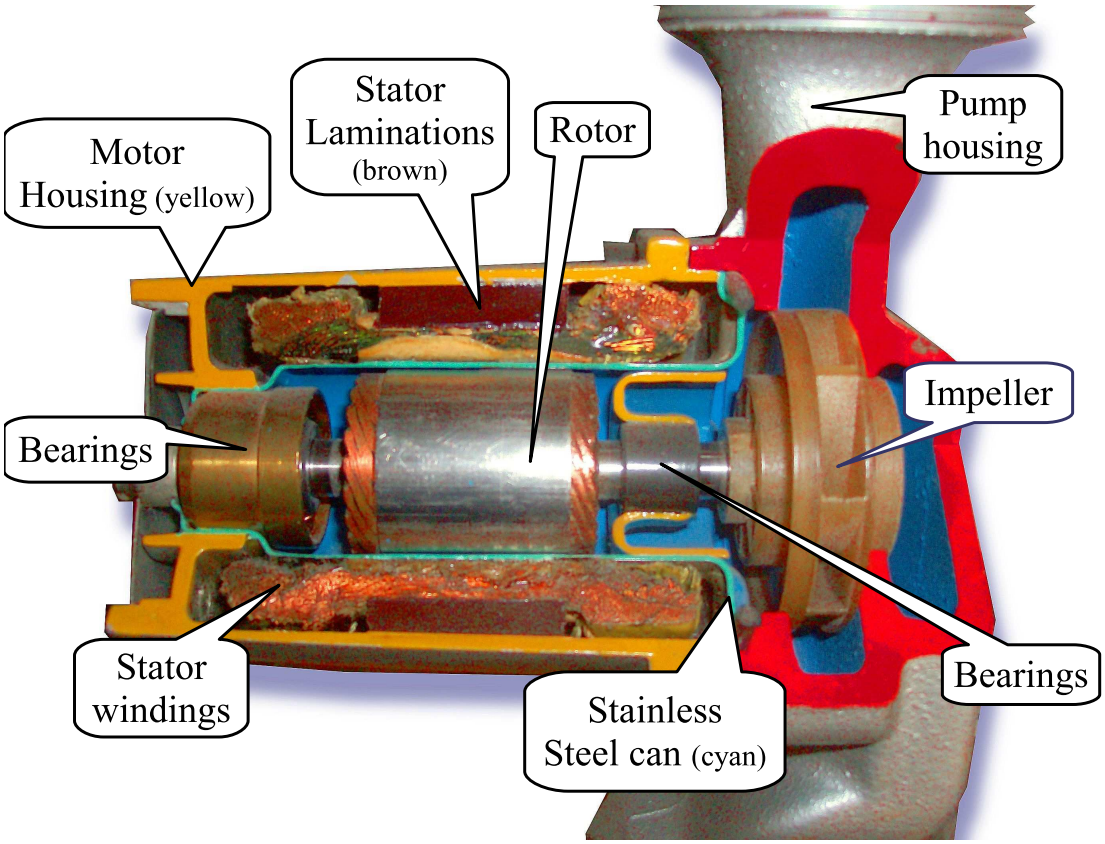

Figure 1.1: The pump is made of a pump housing, an impeller, a rotor, bearings, a stator (with windings), and control electronics (not shown). The areas marked with blue in the pump and motor are normally flooded with water. The motor shown here is a squirrel cage induction motor.

In pump drives of this type, the airgap between the rotor and the stator is flooded with water. Since the airgap is flooded, brushless motors are preferred to brushed DC-motors in pump

drives. The availability of compact and low-priced power semiconductor devices and the drop in the price for computational power made brushless drives possible in low cost applications[5]. However power electronics and micro controllers still adds to the cost of a complete drive and needs to be included with the price of other components when the complete price is determined.

1.2 Low cost motor drives

The main cost-influencing factors are[5]:

- The number of motor strands and windings
- How the type of windings and how the windings are manufactured
- The amount and quality of the built-in permanent magnets
- The number and size of semiconductors in the inverter bridge
- The complexity of the control algorithm and the number and type of sensors needed

But drive cost is also affected by other factors, such as raw materials cost, tooling cost, labour cost, production volume, and the degree of in-house know-how. The motor type is often dictated by a motor designers previous exposure to, and understanding of, different motor types. So the low cost motors considered for pump drives in this section, are mainly brushless motors with no more than three phases, suitable for variable speed control.

The classical motor for low cost pump drives, with a flooded air gap, is the induction motor. For fixed speed, fixed load applications it also does not need electronic control if it is supplied from an AC-supply. The single phase induction motor may be speed controlled by a single triac, where variable speed is achieved by simply shutting down the current for the desired number of periods of the fundamental frequency of the supply or by controlling the turn on angle. Since the load in a pump drive is of a dissipative nature, the speed naturally decreases if no power is supplied to the motor. The single phase induction motor needs to have distributed windings. It

can only supply the second phase at one specific excitation frequency, and has a rotor structure that requires copper or aluminium bars adding cost and losses. A single phase induction motor have been proposed modified with permanent magnets on the rotor to increase efficiency[6], but the copper bars for the squirrel cage rotor are still present. Adding permanent magnets to the induction motor structure will not decrease the cost of this motor type.

The single phase induction motor drive has been used in the pump drives for a long time. The main reasons for this are:

Low Cost: The single phase induction motor requires no or only little electronics for low performance operation. The single phase induction motor is generally considered robust and thus reliable. The facilities that produces these machines have now, in many case, been fully amortized

Simple Control: The single phase induction motor requires little or no control.

The single phase induction motor does however have one important weak point: efficiency is insufficient to current legal requirements, when operated at variable speeds. Part of the problems for the single phase induction motor has to do with the motor construction used in making the wet runner pumps. In wet runner pump motor drives, the windings have to be protected against the water. To achieve this a steel can is inserted in the air gap between the rotor and the stator. This does however increase the length of the air gap, which also increases the reluctance in the flux path. This impacts the induction motor since the current in the rotor is induced from the stator side to the rotor. This means that if the airgap increases the magnetizing current also has to increase to maintain the desired flux linkage. This will give larger losses on the stator side in the induction motor. This increase in current on the stator side also increases eddy current losses in the stainless steel can.

Another simple motor type is the single phase synchronous motor or its close relative the single phase brushless DC-motor. Both motor types has a simple construction as it is shown in Fig. 1.2, however since the rotor is non-salient this may complicate efficient position sensorless control at low speed. When no saliency is present, rotor detection normally relies mostly on the electro-

motoric force of the rotor (back-EMF) for detection of rotor angle. This motor type is however very insensitive to the length of the air gap, may use simple coils, and obviously has little rotor power losses.

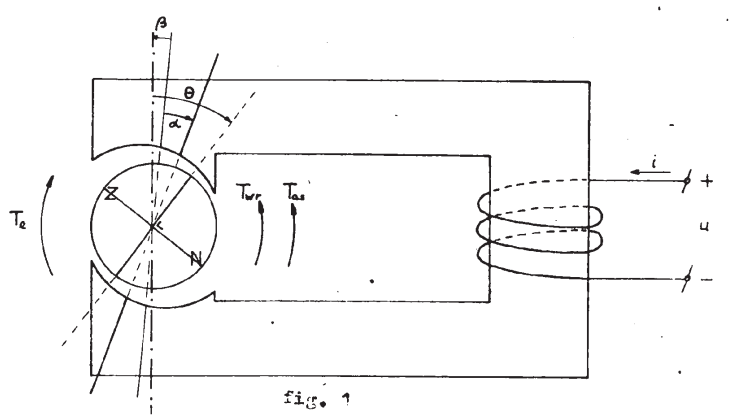

Figure 1.2: A single phase synchronous motor as it was presented in [7, 8].

During the 1970's and early 1980's the introduction of power semiconductors and microprocessors started a new era of research in new topologies[1]. New motor types were introduced, such as the brushless DC-motor and others were re-introduced such as the switched reluctance motor. Since electronic control enables a much more flexible control over the phase currents, motors that were not practical previously are now more interesting.

Permanent magnet motor types are considered to achieve the highest efficiency in low power drives, despite a relatively large air gap[9]. The high efficiency for permanent magnet motors may be achieved since large parts of the flux is supplied by the permanent magnets. The discussion that follows will therefore only focus on the permanent magnet motors, since efficiency is a key concern in the desired motor drive for this thesis.

1.2.1 Components of the electrical motor

The electrical motor is a combination of several components:

Laminations: Except for coreless drives, most electrical motors use steel laminations made of

silicon doped iron. The inclusion of silicon is to reduce iron losses due to eddy currents and to reduce hysteresis losses by making the hysteresis loop more narrow. The increased silicon content does however make the steel laminations more brittle. The price for steel laminations is continously increasing [10].

Iron can be recycled virtually indefinitely with no degradation of properties and thus part of the iron supply is existing iron based structures. Furthermore there are several countries worldwide that has significant iron reserves and this ensures healthy competition in the foreseeable future. Threats however exists to continued access to low cost iron: the recent collapse of the established steel trade system[11], and the current increase in steel consumption[11].

Coils: Windings in electrical motors are typically wound in the stator as either distributed or short turn windings. Sinusoidally distributed windings produce less harmonics and thus reduces motor losses, but are also more complicated and costly [12]. Concentrated windings are typically found in cost sensitive commercial motors in the forms of PMSM, BLDC as well as SRM.

Two materials are used for machine windings: aluminium and copper. Aluminium is sometimes used as a conductor due to lower cost as compared to copper. However aluminium has a significantly poorer thermal conductivity than copper and should therefore be disregarded as a winding material for small low power motors[13].

The copper price has increased since the turn of the century until the economic crisis appeared. The economic crisis forced a dip in the prices, but the copper price has since rebounded and currently headed towards the pre crisis price again as it can be seen in Fig. 1.3. This means that the long term outlook for copper is most probably a continued increase in prices given the continued growth in the emerging markets. This means that the motor design should seek to minimize the use of copper.

.

Magnets: Permanent magnets comes in many shapes, sizes, and materials. The most used permanent magnet materials are neodymium-iron-boron (NdFeB) magnets and ferrite mag-

Figure 1.3: The copper price for cash purchase of copper as seen on London Metal Exchange from 16/01-1998 to 16/01-2011[14]. The dates on the graph have been edited to increase readability.

nets of various types. The NdFeB magnets has the highest remanent flux and best resistance against demagnetization. When a motor has permanent magnets, demagnetization has to be avoided through design and by monitoring the currents in the coils. Ferrite magnets have the best resistance against corrosion (including water) and tolerates higher temperatures than NdFeB magnets, and quite importantly it also has lower cost. But since the flux density is so low, and to increase resistance against demagnetization more permanent magnet material has to be used when the magnets are ferrite magnets instead of NdFeB magnets. This in turn also means that the machine increases in size, potentially increasing the consumption of other materials, like iron laminations and copper for the windings. The prices for NdFeB dropped since the turn of the millennium, but prices for the raw materials neodymium and dysprosium has more than doubled from 2005 to 2010[15]. The long term outlook for prices for NdFeB is subject to the availability at the dominant source of the rare earth materials neodymium and dysprosium, namely Chinese mining companies. The Ministry of Land and Resources of the Peoples Republic of China has stated that the prices of rare earths probably will continue to increase and has urged other countries to diversify their sources of rare earth metals to reduce the burden on Chinese resources[16]. The Chinese government decided to decrease export of neodymium in the second half of 2010 by 72%[17] and to have an export sales tax of 25%[18]. This move probably comes

to protect the domestic Chinese market, since the Chinese demand is expected to equal its supply by 2012 [19]. Since more than 97% of the rare earths used in production is coming from China, the prices are expected to continue to increase in the foreseeable future[20]. At the time of the writing, a sharp increase in magnets is seen from some magnet producers such as the announced price increase by Shin-Etsu of 40 % compared to two month before, which was even preceded by similar price increases since 2010[21]. This makes ferrite magnets an interesting alternative to NdFeB.

1.2.2 Drive electronics

The key components in a line connected permanent magnet motor drive are:

Line interference suppression filter: To reduce line interference to stay within EEC directive 2006/95/EC. Typically made of a choke-coil and capacitors to remove high-frequency content from the line current.

Varistor: Varistor may be used to protect against surge voltages, but is not mandatory.

Rectifier: Since most permanent magnet motors actually need a DC-source

DC-link capacitor: Both as a filter and as an energy storage element

Integrated power module or discrete power components: To control the phase currents, and thus control the motor.

Current measurements shunts: To measure phase currents accurately, proper current shunts may be necessary to measure currents at a wide range of temperatures.

Microcontroller: To actively control the motor and is indeed required for a variable speed pump drive, since speed is controlled based on knowledge of the impeller characteristics.

The cost of the permanent magnet motor drive could possibly be reduced by optimizing ratio between materials usage and/or drive electronics, but for this thesis these parameters are not

considered with regards to optimization. It is important to note though that a single phase or three phase motors seems to be the best options for low cost drives. The single phase motors may use few power components, and three phase systems can use standard three phase integrated power modules. Unlike the raw materials for the motor, the price for power electronics is expected to decrease and the performance is expected to improve. So it may be desirable to "‘move"’ some of the losses from the motor to the power electronics, if possible.

Polyphase machines are considered more complex, and thus potentially more expensive, than single-phase versions. On the other hand polyphase machines may offer better torque density, better efficiency and possibly lower noise than some single phase motors. Motors using magnets may be more expensive than switched reluctance motors[5], but may also be less sensitive to a large airgap. The question then is: Does the simpler motors fullfill the requirements for efficiency, power density, dynamics, torque ripple and noise[5]? The aim of this thesis is to show if these points are fulfilled when a single phase hybrid switched reluctance motor is used in a pump drive.

The presentation of the hybrid switched reluctance motor in the following section also includes a look at the single phase switched reluctance motor, since the switched reluctance motor forms the basis for the motors considered in this thesis.

1.3 Presentation of the hybrid switched reluctance motor

The single phase hybrid switched reluctance motor is developed based on the single phase switched reluctance motor. It is informative to see some of the problems facing a single phase switched can be handled by adding permanent magnets making the motor a hybrid switched reluctance motor.

1.3.1 Single phase SRM

A simple machine can be made of two pieces of iron and a coil as it is shown in Fig. 1.4.

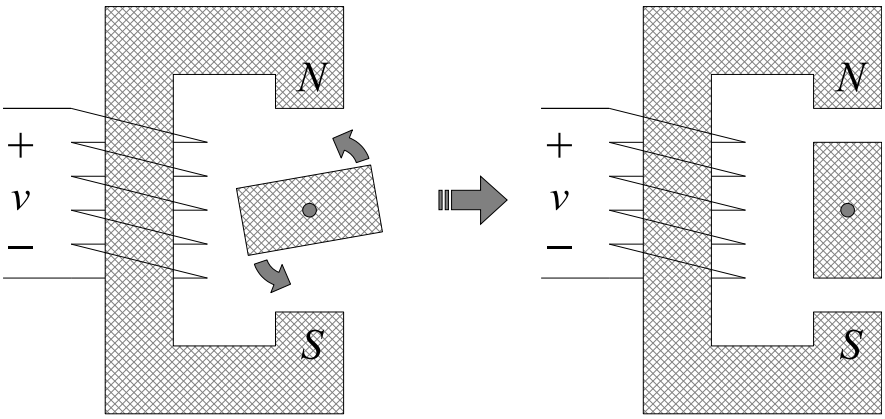

Figure 1.4: Principle of reluctance machine, with one phase winding and two stator poles and two rotor poles. First the machine is in an unaligned position, and later the machine is in the aligned position.

When the coil is energized, the rotor is attracted to the stator. The rotor starts to rotate until the rotor is aligned with stator, and the rotor thus moves from near unaligned position to aligned position. It is obvious that the motor in Fig. 1.4 cannot produce torque with same direction as the rotation for all rotor angles. At some angles the torque may have an opposite direction of the rotation and at some angles the torque production may be close to zero or zero.

The phase inductance varies based on the position of the rotor[22]. Assuming a simplified model of a single phase reluctance machine the torque production can be described as[22, 23]:

$$\tau = \frac{1}{2} i^2 \frac{dL}{d\theta} \tag{1.1}$$

where τ is the instantaneous torque, i is the instantaneous coil current, L is the coil inductance, and θ is the instantaneous rotor angle. Equation (1.1) and Fig. 1.4 shows several important points:

- The direction of the torque is only dependent on the change in the inductance, but not the direction of the current. This also means that it can only produce torque in the same direction as the rotation in a particular range of rotor angles.
- Zero torque zones are unavoidable for a single phase machine.
- The initial position is important to determine the direction of the initial rotation.
- Torque production is dependent on saliency on the rotor and the stator. This means that the torque production may be shaped by the designed saliency on the rotor and the stator.

To ensure that the single phase switched reluctance motor is starting in the correct direction, some kind of asymmetrical elements in either the rotor or the stator has to be added to ensure that the rotation goes in the desired direction only[5] or by adding a parking method. The parking is typically achieved by mechanical means or by using permanent magnets.

1.3.2 Single phase HSRM

The HSRM considered in this project has permanent magnets embedded in the stator, thus being a hybrid between a pure switched reluctance motor (SRM) and a permanent magnet machine.

The main problem for all single or even two phase SRM is to start rotating in the intended direction of rotation[5]. Single phase SRM may use saturation to ensure starting in the correct direction as it was presented in [24]. This makes it possible to make the minimum reluctance position dependent on the current magnitude, but only within a given range of angles. But this only partially ensures a solution since the motor still will only start in the desired direction if the

rotor position is in this range of angles[5]. To avoid the introduction of a second phase, as in the motor presented in [25], but still maintain the simplicity of a single phase motor it is possible to use permanent magnets. The use of permanent magnets to ensure that the rotor is parked in a predefined position when no current is in the coil has been used for clockwork stepper motors as in [26] as it can be seen in Fig. 1.5.

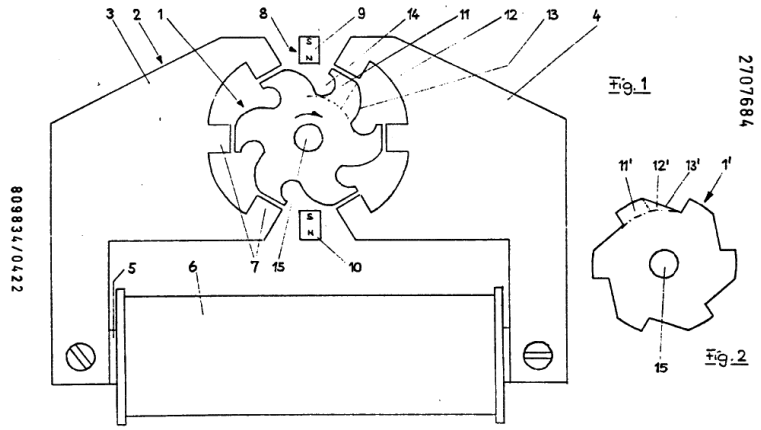

Figure 1.5: An early hybrid switched reluctance motor from a 1978 german patent[26], which is structurally similar to a 1966 american patent of a single phase permanent magnet synchronous motor(see [27]).

The motor shown in Fig. 1.5 [26] has two interesting features: a permanent magnet to ensure parking when there is current in the coil and a kind of electromagnetic gearing by having more teeth on the stator and rotor per flux source. The placement of the coil however means that the stator is not be made of one piece of iron and has to be assembled. Several different single phase SRM used this principle as presented in [28, 29, 30], but without the electromagnetic gearing used in the clockwork motor. These designs has two main problems: firstly the permanent magnet torque has to be overcome by the torque produced when the coil is energized and secondly does the permanent magnets not contribute to the average torque because they are not in the main flux path[5]. If the permanent magnets are put in the flux path the average torque production is indeed increased and the torque from the permanent magnets can also be controlled. This will be described in detail in the motor modelling chapter 3. Such a motor is presented in [31] as it is shown in Fig. 1.6.

In Török's design the flux from the coils has an opposite direction of the flux from the permanent

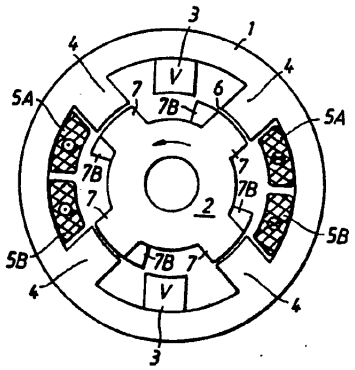

Figure 1.6: The principal drawing of the motor described in Töröks patent from 1992[31].

magnets. The flux from the permanent magnets is directly influenced by the current in the coil, since the permanent magnets are in the main flux path of the coils. Notice that Török also uses the electromagnetic gearing seen in the clockwork motor. Török's is not the only and first design to use permanent magnets in the main flux path. The first use of permanent magnets in the main flux path is presented [32] for a flux switching motor used as a generator, and the flux switching motors form their own branch of single phase doubly salient motors. The flux switching motors, does however require bidirectional current[33] and this increases the number of required transistors in the converter for the motor compared to the single phase hybrid SRM. Similarly if the permanent magnet are placed on the rotor in a SRM, such a motor would also require bidirectional excitation as it is shown in [34]. Yet another design which uses permanent magnets in the flux path of the coils to improve performance is presented in [35], but this design uses a segmented stator very similar to [32].The design presented in [35] however only requires uni-directional current. A simplified hybrid SRM design is presented in [5] to make the hybrid SRM more economical. The main feature is that the motor coils are similar to the simple coils used in single phase universal motors used for low cost drives. The permanent magnets in the design presented by Török and Wissmach are glued to the stator back will thus be exposed to the full normal force from the rotor. One method to protect the permanent magnets against the normal force is to put the magnets in structural "'pockets"' in the iron laminations. Permanent magnets may need to be structurally protected against mechanical forces in a permanent magnet motor design, since permanent magnets may be brittle and prone to cracking. The designs presented by Török and Wissmach does not structurally protect the

permanent magnets, most likely since "'pocketing"' a single magnets in the stator may reduce the amount of permanent magnet flux crossing the airgap. If less permanent magnet flux crosses the airgap, the cogging torque would be reduced and the average torque would also decrease. Lu et. al introduced permanent magnet flux concentration to increase the cogging torque[36], however the design used a segmented stator and does not structurally protect the permanent magnets against the forces acting on the stator. A segmented stator may pose challenges in motor assembly, and this may increase the cost.

So there is a need for a single phase hybrid switched reluctance motor design that pockets the permanent magnets that lie in the main flux path and only use a one segment for stator lamination.

To summarize the hybrid switched reluctance motor strengths and weaknesses:

Strengths

- A single phase hybrid switched reluctance motor is claimed to be the cheapest of all permanent magnet brushless machine types[5].
- Unlike the single phase switched reluctance machine, positive torque may be produced for all angles.

Weaknesses

- The single phase hybrid switched reluctance motor produces a pulsating torque. This is however also a problem for the single phase brushless DC motor[37, 38].
- Needs to be in a predefined starting position, but this may be ensured by permanent magnets if the load torque is not too high.
- The single phase machine may be more noisy[5].

1.4 Problem Formulation

The main idea in this thesis is to design a low power, low cost hybrid switched reluctance motor drive. The drive should be operated in a position sensorless control mode, due to the cost issue.

1.4.1 Motivation

There is a trend towards energy efficiency in pump motor drives, partly driven by increased legal requirements towards minimum energy efficiency. Induction motors struggles to compete with permanent magnet motors regarding efficiency, when the output power is low[39]. This has moved the focus to two classical motor types: the brushless DC-motor (BLDC) and the permanent magnet synchronous motor (PMSM). An interesting motor alternative is the single phase hybrid switched reluctance motor(HSRM), since the HSRM offers a very simple construction that may have lower manufacturing costs.

1.4.2 Objectives

So the main research question is:

Is the hybrid switched reluctance drive suitable as a low cost, low power, variable speed pump drive?

Since this main research question is too large a scope for a single thesis, four key research topics are selected for further investigation:

1. *Can the existing hybrid switched reluctance motor design be simplified to reduce the cost?*

2. *Is it possible to design the motor so it may achieve a full load efficiency similar to a PMSM or BLDC, and still reduce the amount of materials used? The benchmark chosen are motors presented in [40].*

3. *Is it possible to remove the rotor position sensor, to further reduce cost?*

4. *The stainless steel can in the air gap is increasing cost and reducing efficiency, so is it possible to remove the stainless steel can in the airgap and still protect the windings against boiling water?*

1.5 Thesis Outline

The investigations documented in this thesis is organized into four main parts besides appendices. A brief outline of the individual chapters is given below.

- **Part I - Preliminaries**

  1) Introduction

  This chapter.

  2) Pump drive systems

  This chapter deals with the requirements for a low power, low volume, low cost pump motor drive. The chapter introduces a brief review of a simple pump system, an overview of relevant motor types and a review of prices of some key materials in electrical motors.

- **Part II - Motor Design**

  3) HSRM model

  The hybrid switched reluctance motor model is presented here explaining how permanent magnets increase the torque density of this motor type, and how the magnets helps shaping the torque profile.

  4) HSRM design

  The first design introduces pole shaping on the stator to improve starting torque. A new flux concentrating arrangement of the permanent magnets, that increase the flux density in the airgap, is also presented. Different flux concentrating arrangements are compared and evaluated. The motor uses square bobbins for the coils and has coil insertion slots to simplify the motor manufacture.

  5) Pump motor implementation

  The second motor design tries to reduce the number of permanent magnets needed and fit into a conventional pump housing. Still the motor maintains the coil insertion slots introduced in the previous chapter. Here a lower cost alternative is proposed to the stainless steel can that is used in conventional wet-runner pump drives.

- **Part III - Control**

6) Control methods for HSRM

This chapter describes how the cascaded variable speed drive control is implemented for the HSRM. This chapter describes time variant speed control methods suitable for high torque ripple drives.

7) Sensorless Control

The new position sensorless control method presented in this chapter is insensitive to variations in DC-link voltage, phase resistance, temperature, variations in inductance, parameters of the inverter and current control method. The sensorless method requires only simple operations that can be implemented in low cost micro controllers. This chapter describes how the sensorless control is implemented based on back-EMF sensing, including a method for the speed estimation and error recovery. The description includes a detailed description of the implementation and the test results for the position sensorless method in open air and in a pump system.

- **Part IV - Conclusion and Future Work**

8) Conclusion

This chapter is a summary of the conclusions drawn in the previous chapters. Contributions believed to be novel are highlighted.

9) Future work

Some suggestions for further research are proposed here.

Chapter 2

Pump drive systems

This chapter describes a few aspects of the centrifugal pump system used in central heating.

2.1 The pump system

A simplified heating system can be made of a pump, a boiler unit, a radiator, fittings, and the pipes that closes the loop[4]. The primary task of the pump is to compensate for the pressure loss in the radiator, fittings and the pipes to ensure a desired flow of liquid. The liquid is used to circulate the thermal energy from the heater to the radiator through the pipes. A significant performance factor for a controlled pump is its annual energy consumption[4]. A pump is equipped with a controller, may achieve a significant reduction in losses compared to a fixed speed pump[4]. The energy savings of a speed controlled pump mainly comes from its ability to reduce speed at reduced flow[41].

The following tries to establish the relationship between the pressure compensation needed, the mechanical input power needed to drive the impeller, and the relationship between head and flow. It is only intended to clarify the main aspects regarding a centrifugal pump.

Circulation pumps for aquatic facilities are almost exclusively centrifugal pumps, where the water in the impeller is subjected to kinetic energy, of which some is converted into a static

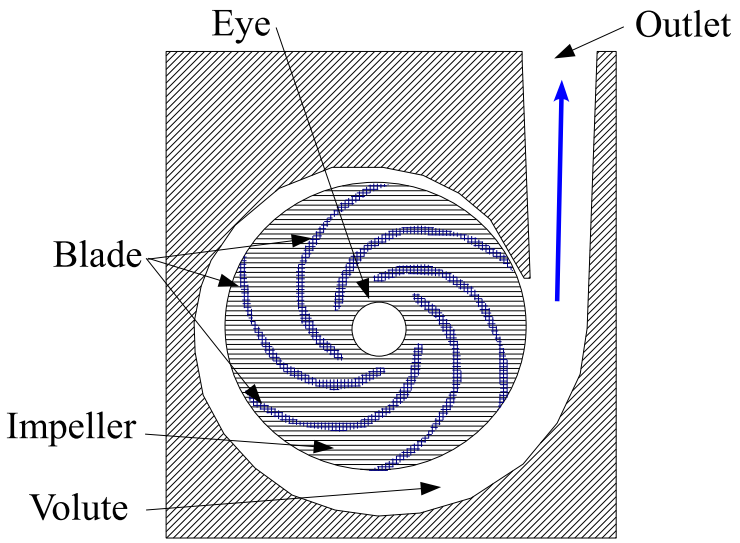

Figure 2.1: Schematic drawing of a centrifugal pump. Based on a drawing in [42]

pressure[43]. The function of a centrifugal pumps is as simple as its design. It is filled with liquid and the impeller is rotated. Rotation gives energy to the liquid causing it to exit the impellers vanes at a greater velocity than the entry velocity. This outward flow reduces the pressure at the impeller eye, allowing more liquid to enter. Rotation of the impeller forces water from its entry point, at the impeller eye, through the impellers vanes and into the volute. The liquid that exits the impeller is collected in the casing (volute) where its velocity is converted to pressure before it leaves the pumps outlet [43].

In the following two assumptions are made[42]:

1. The liquid is incompressible

2. The flow through the pump is without losses.

Furthermore it is assumed that the liquid is homogenous.

The needed input power to move a liquid at a given flowrate and pressure-differential is given by[43]:

$$P = Q \cdot \Delta p \tag{2.1}$$

Where P is the power input on the shaft on the motor to the impeller, Q is the flowrate in m^3/s, and Δp is the pressure-differential in Pa.

The power delivered by the motor and pump is given by:

$$P = \tau_{motor} \cdot \omega_{motor} \tag{2.2}$$

And finally the relationship between the pump head H, the flowrate Q and the input power P:

$$P = \rho \cdot \boldsymbol{g} \cdot Q \cdot H \tag{2.3}$$

Where $\boldsymbol{g}$ is the gravitational constant, and ρ is the density of water.

A centrifugal pump will always develop the same head in meter regardless of a liquids specific gravity.

The head related to the speed of the impeller:

$$H = \frac{v_{impeller}^2}{2 \cdot \boldsymbol{g}} \tag{2.4}$$

Where the speed of the impeller $v_{impeller}$ is given by:

$$v_{impeller} = O \cdot \omega = D \cdot \pi \cdot \omega \tag{2.5}$$

where O is the circumference of the impeller and D is the diameter of the impeller. So the head is given by:

$$H = \frac{(D \cdot \pi \cdot \omega_{motor})^2}{2 \cdot \boldsymbol{g}} \tag{2.6}$$

Inserting equation (2.6) into equation (2.3):

$$P = \rho \cdot \boldsymbol{g} \cdot Q \cdot \frac{(D \cdot \pi \cdot \omega_{motor})^2}{2 \cdot \boldsymbol{g}} = \tau_{motor} \cdot \omega_{motor} \tag{2.7}$$

Bernoullis theorem states that during steady flow the energy at any point in a conduit is the sum of the velocity energy, pressure energy, and the potential energy due to elevation. It also says the the sum will remain constant if there are no losses[42, 44].

$$\varepsilon = \underbrace{\frac{\rho \cdot v^2}{2}}_{velocityenergy} + \underbrace{p}_{pressureenergy} + \underbrace{\rho \cdot \mathbf{g} \cdot h}_{potentialenergy} = constant \tag{2.8}$$

where ε is the local energy density of the liquid, p is the local pressure, $\mathbf{g}$ is the gravitational acceleration, and h is the local height.

Given Bernoullis theorem, Fig. 2.2 shows how energy is transferred from the motor to liquid by increasing the kinetic energy in the flow. The volute then transforms the increased speed to an increased pressure.

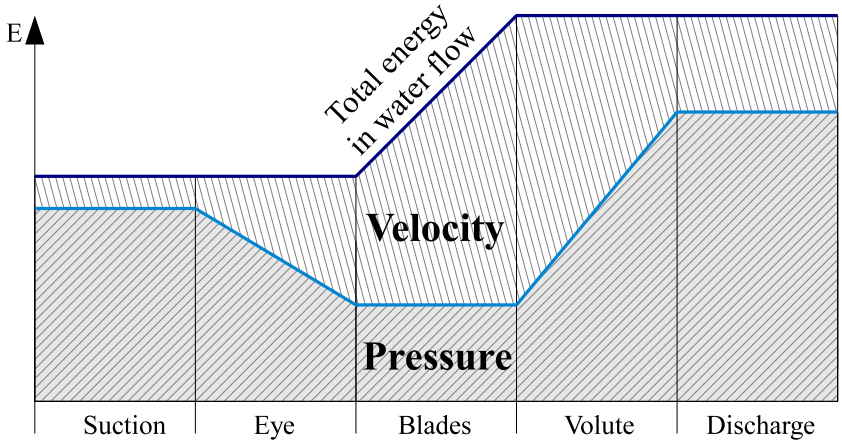

Figure 2.2: The light blue area is velocity energy and the dark blue area is pressure energy. The total energy of the system is represented by the upper edge of the light blue area. Adapted from drawing on [44]

Liquid flow in pipes can take two forms: laminar flow and turbulent flow. Wether the flow in a uniform tube is laminar or turbulent can be determined from its Reynolds number (*Re*)[45]:

$$Re = \frac{\rho \cdot v \cdot D_{pipe}}{\eta_l} = \frac{v \cdot D_{pipe}}{\nu} = \frac{4 \cdot Q}{\pi \cdot D_{pipe} \cdot \nu} \tag{2.9}$$

Where $v = \frac{Q}{\left(\frac{1}{2}D\right)^2 \cdot \pi}$ is the average speed of the liquid, η_l is the dynamic viscousity of the liquid, D_{pipe} is the inner diameter of the pipe, and $\nu = \eta_l / \rho$ is the kinematic viscousity.

If $Re < 2000$ the flow is steady, i.e. laminar. If $Re > 2500$ then the flow is turbulent, i.e. vortexes are formed[45].

The task of the pump is to compensate for the pressure losses in the pipes, caused by laminar and/or turbulent pressure losses.

The laminar loss in pipes (excluding bends and narrowed pipes) is given by[45]:

$$\Delta p_{loss,lam} = \frac{128 \cdot \nu \cdot \rho \cdot L}{\pi \cdot D^4} \cdot Q = \frac{32 \cdot \eta_l \cdot L}{D_{pipe}^2} \tag{2.10}$$

The turbulent loss is given by[45]:

$$\Delta p_{loss,turb} = \frac{\lambda \cdot \rho \cdot L}{2 \cdot D_{pipe}} \cdot v^2 \tag{2.11}$$

The friction coefficient (λ) depends on the roughness of the pipe and the Reynolds number amongst other parameters. Typical range would be:$0.01 < \lambda < 0.04$[45].

Finally pressure losses over individual components, like the heater and the radiator, can be calculated by:

$$\Delta p_{comp} = \zeta \frac{1}{2} \rho \cdot v^2 \tag{2.12}$$

Where the resistance number (ζ) depends on the specific component.

Rewriting equation (2.1):

$$\frac{P \cdot \eta}{Q} = \frac{\tau_{motor} \cdot \omega_{motor} \cdot \eta}{Q} = \Delta p_{pump} \tag{2.13}$$

So in the simplified case the following is valid for a closed system with a centrifugal pump:

$$\begin{aligned} \Delta p_{pump} &= \Delta p_{comp} + \Delta p_{loss,turb} + \Delta p_{loss,lam} \quad \Updownarrow \\ \frac{\tau_{motor} \cdot \omega_{motor} \cdot \eta}{Q} &= \Delta p_{comp} + \Delta p_{loss,turb} + \Delta p_{loss,lam} \end{aligned} \tag{2.14}$$

This equation is only valid if the liquid is homogenous, i.e. it is not valid if cavitation occurs in the pump. Cavitation occurs when vapour bubbles are formed in a region of a liquid where the pressure of the liquid drops below its vapor pressure point.

For systems where friction loss predominates, reducing pump speed moves the intersection point on the system curve along a line of constant efficiency (see Fig. 2.3)[46]. However for small

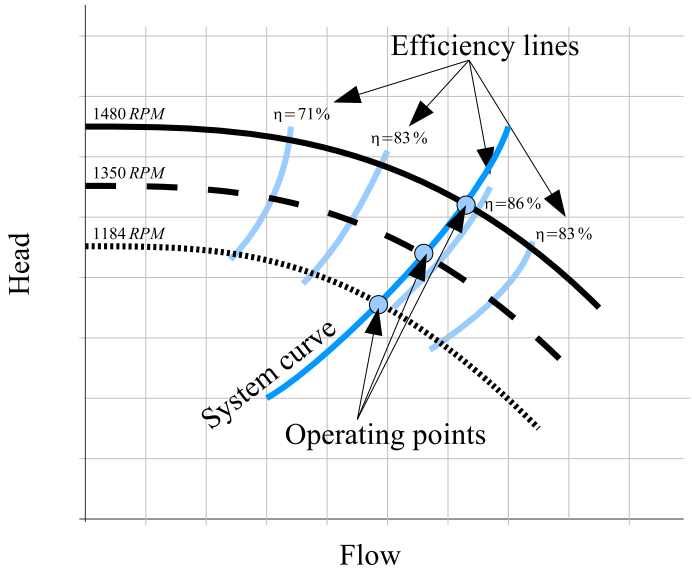

Figure 2.3: Example of the effect of pump speed change in a system with only friction loss[46]

pumps, the losses internally in the pump can not be neglected and efficiency becomes a more complex issue that is beyond the scope of this thesis.

The impeller efficiency is dependent on flow, and decreases with flow. In [47] a peak efficiency of 60 % is reported for an optimized impeller at the nominal flow dropping to 10 % at approximately 10 % of nominal flow.

The interdependency of flow and head means that by adjusting the speed it is possible to track the system curve shown in Fig. 2.3. This means that a variable speed drive is needed to control the pump efficiently at reduced output.

2.2 Summary

A pump system, considered in this thesis, is a wet-runner centrifugal pump connected with boiler, and some load in the shape of pipes and radiators. Some relations between different parameters relevant for such a system was introduced.

Part II - Motor Design

Chapter 3

HSRM model

A variable speed pump drive would typically be controlled by a microcontroller, since energy efficient pump control would require knowledge of the behaviour of the impeller and the pump housing, as described in the previous chapter. The focus of this thesis is however not on the dynamic behaviour of the pump and impeller, but on the hybrid switched reluctance motor drive. The purpose for the model presented here is thus primarily to enable simulations of the dynamic behaviour of a hybrid switched reluctance motor (HSRM), both for the motor but also for the fan load [1]. This dynamic simulation can then be used to evaluate the control methods, including the position sensorless control method. This chapter starts by describing the HSRM and finishes by describing the dynamic model of the HSRM.

3.1 The hybrid switched reluctance motor

The hybrid switched reluctance motor (HSRM) differs from the normal switched reluctance motor, mainly because the permanent magnets introduce a magnetic bias field in the motor. The HSRM model presented here describes how the permanent magnets increase the torque density of the motor due to the bias field from the permanent magnets.

[1] The pump is assumed to be a quadratic load as the fan.

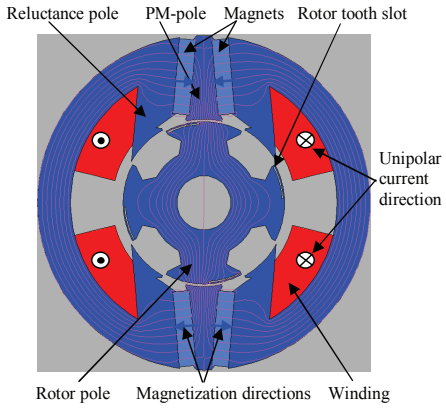

(a) The hybrid switched reluctance motor proposed in [36]. Notice that the stator is made of four segments.

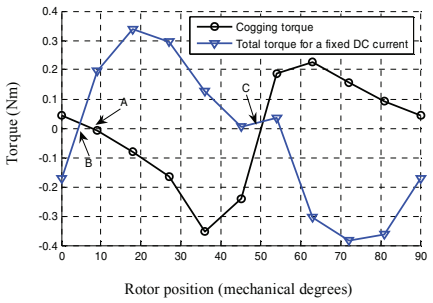

(b) The torque envelope from [36] which shows the torque with full phase current(total torque) and no phase current (cogging torque).

Figure 3.1: Drawing and torque profile from HSRM proposed in [36]

A HSRM was previously designed at Aalborg University and presented in [36], as it is shown in Fig. 3.1. The motor presented in [36] is similar with the HSRM designed and analysed in this thesis as it is shown in Fig. 3.2. More details of the HSRM shown in Fig. 3.2 will presented later in the following sections and also in the next chapter. The reference frame for the coordinate system used for rotor angles are the shown in Fig. 3.2.

The HSRM has six poles on the stator side, two permanent magnet poles (PM-poles) and four reluctance poles. The rotor has four poles with a saturable saliency. This ensures that the rotor is parked by the permanent magnets at a known rotor angle when there is no phase current. The parking position may easily be identified from the motors torque profile, by identifying the angles with near zero cogging torque at near flat slopes of cogging torque. When the two series connected coils are energized, a flux is generated that opposes the flux from the permanent magnets and attracts the rotor poles to the reluctance poles. When defluxing the coil, the process repeats as the permanent magnet poles attract the rotor. In the region where there is negative combined torque the current should be kept zero, and the positive cogging torque serves as the motoring torque that pulls the rotor to its original position.

One sequence of operation, also known as a stroke, contains three main steps:

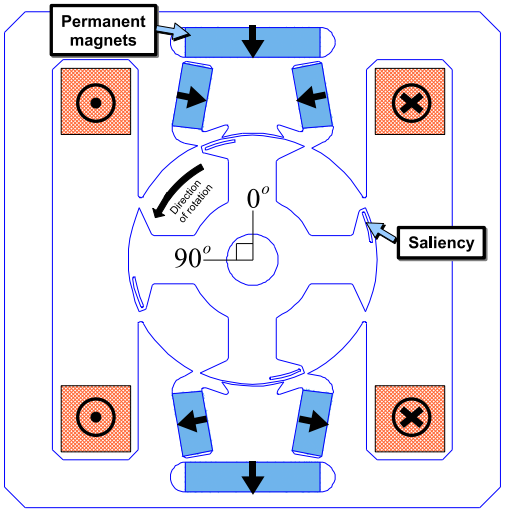

Figure 3.2: HSRM used as basis for the dynamic model, here with rotor shown at an angle of 0 degrees. Circles enclosing either dots or crosses indicate the direction the coil current. The two coils are connected in series. Due to the saliency in the rotor the normal parking position of the rotor is normally at 1-5 degrees. Manufacturing sets a lower limit on how thin the cut outs in the laminations can be. This limitation means that the saliency is not thin enough to generate a flat top torque when the coil is energized. Thick black arrows indicate magnetization direction of the permanent magnets.

1. The machine is initially parked at a rotor angle slightly offset from the 0 degrees shown in Fig. 3.2, ideally at the zero cogging torque position. The offset is due to designed asymmetry in the rotor poles and the bias permanent magnet field.

2. The stator coils are energized and due to the reluctance between the four stator "reluctance" poles and the rotor in the position described above, the rotor rotates to minimize the reluctance. When the reluctance is at a minimum, the rotor is said to be aligned with stator poles. That would mean a rotor angle close to 45 degrees, where the combined torque is close to zero.

3. When the rotor is aligned with stator reluctance pole, current is removed from the coils through a defluxing period. The permanent magnets will then pull the rotor to the first position, and the process is repeated. The process of flux-removal is also called defluxing.

3.2 Model of Hybrid Switched Reluctance Motor

An electrical motor is a device that converts electrical energy to mechanical energy as it is shown in Fig. 3.3, where W_{el} is electrical energy from the supply, W_{cap} represents energy in the DC-link capacitor, W_{cu} are energy lost due to coil winding resistance, , W_{Fe} represents iron losses, W_Ψ is stored in the magnetic flux, , W_{cog} is the energy associated with cogging torque, , W_{fric} is for the frictional energy losses, W_J is energy stored in the rotational mass, and W_m represents the energy supplied to the load.

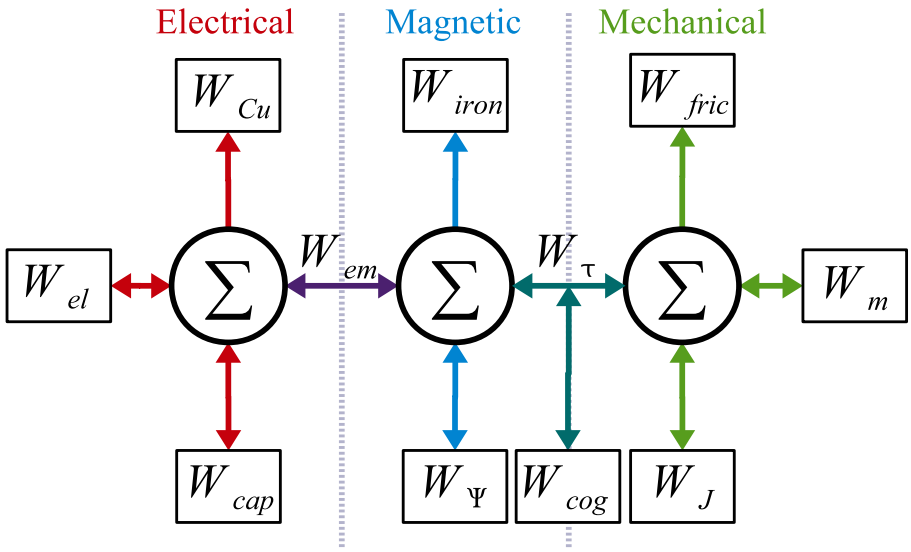

Figure 3.3: In an electrical motor energy is converted from electrical energy to mechanical energy or if the motor is used as a generator the mechanical energy is converted to electrical energy. Dissipative elements are on the top, whereas energy-storage elements are below. See text for an explanation of the symbols.

The dynamic model should be able to predict the transient behaviour of the non-linear HSRM. It is particularly interesting to calculate the current waveforms, rotor speed, and rotor angles, since these parameters can be directly measured in a real system. The DC-link and the inverter are ignored in the model presented here, so the model only describes the HSRM and a simplified model of the load.

This model is based on calculating the continuous states of the energy storage elements in the model: the magnetic flux, the cogging torque and the moment of inertia. Cogging torque and

torque generated by magnetic flux from a coil are not easy to separate in magnetically saturated systems[48, 49, 50], and therefore they are not separated in the model presented here. To simplify the calculations the cogging torque is not considered directly as an energy storage element in the electromagnetical system, but is moved to the mechanical subsystem. The torque production is then considered as a non-linear function of rotor angle and phase current. The magnetic flux from the coils and the permanent magnets are added together using the superposition principle, though it is not strictly correct due to saturation effects. The following sections briefly describe how key parameters are calculated: flux linkage, phase current, torque, speed and angle. Based on these calculations the selected state variables (flux linkage, phase current, moment of inertia and speed) are used to model the HSRM.

3.2.1 Fluxlinkage calculations

The general flux linkage equation is given in (3.1):

$$\begin{aligned} u &= R \cdot i + \frac{d\Psi}{dt} \Leftrightarrow \\ \Psi &= \int (u - R \cdot i)dt + \Psi_0 \end{aligned} \tag{3.1}$$

where u is the phase voltage applied to the phase, R is the phase resistance, i is the phase current, Ψ is the phase flux linkage, and Ψ_0 is the initial flux linkage in the phase. Ψ_0 is caused by the permanent magnets and is angle (θ) dependent. The field generated by the armature current is opposing the magnetic field from the permanent magnet. The armature flux and the permanent magnet flux are conducted by different stator poles and therefore it may assumed that the permanent magnet field is somewhat independent of the armature current. Substituting the initial flux linkage (Ψ_0) with the angle dependent flux linkage ($\Psi_{PM}(\theta)$), but ignoring the dependence on the phase current. Thus (3.1) can reformulated as (3.2).

$$\Psi = \int (u - R \cdot i)dt + \Psi_{PM}(\theta) \tag{3.2}$$

Due to saturation effects, the above superposition is not accurate for all current levels and rotor angles.

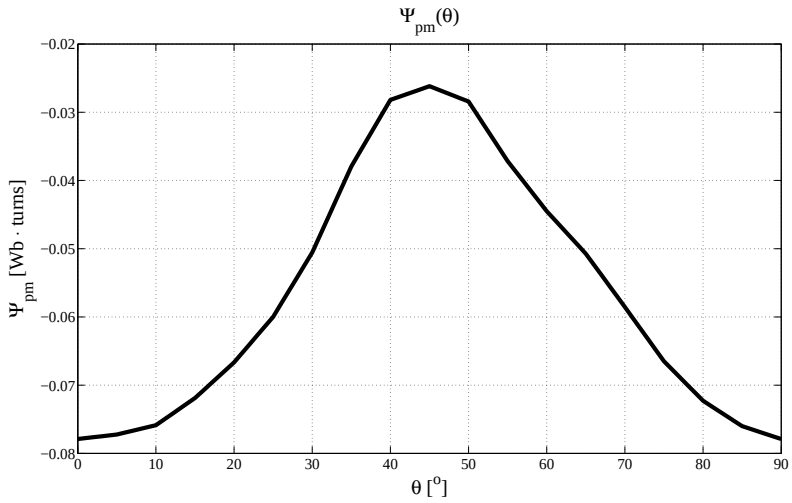

Figure 3.4: The permanent magnet flux look up table as a function of the rotor angle, for the first prototype motor presented in the next chapter.

3.2.2 Phase current calculation

For a HSRM, at a fixed rotor position, the amount of flux generated by a certain current is fixed. Therefore is the phase current uniquely identified by the flux linkage (Ψ) and the rotor angle (θ). The phase current is found using a lookup table with flux linkage and rotor angle as parameters. The lookup table is found using a finite element model of the HSRM. The use of the lookup table can be expressed as a function f_i as it is done in (3.3) where $f_i(\Psi,\theta)$ can be seen in Fig. 3.5.

$$i = f_i(\Psi,\theta) \tag{3.3}$$

3.2.3 Energy conversion and torque production in HSRM

The energy transferred to the magnetic system (W_e) can be described as[51]:

$$W_e = W_{supply} - W_{cu} = \int \left(u \cdot i - R \cdot i^2\right) dt = \int i d\Psi(\theta, i) \tag{3.4}$$

Where W_{supply} is the energy from the supply and W_{cu} is the copper loss.

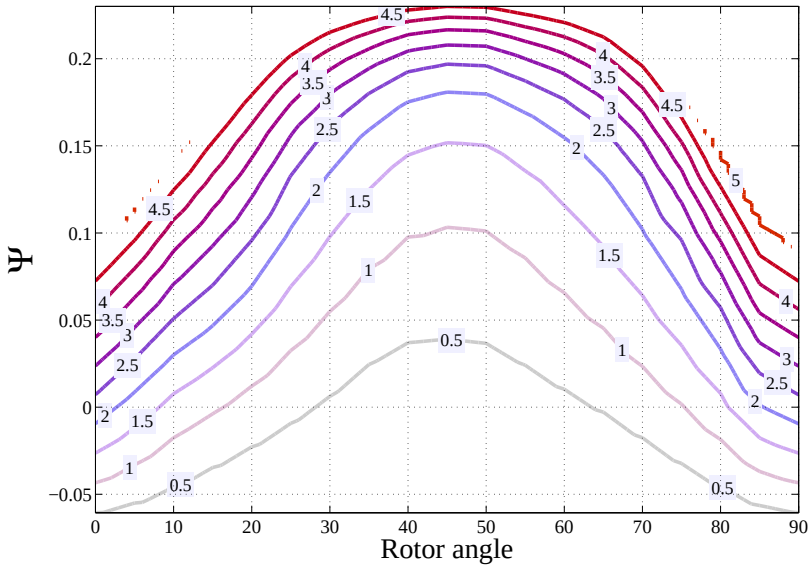

Figure 3.5: A plot of the look up table used for finding the current as a function of the coil flux linkage and angle. The current level is marked on the contours. The data are from the first prototype motor presented in the next chapter.

The field energy ($W_{field}(\Psi,\theta)$) is given by[51]:

$$\begin{aligned} W_{field}(\Psi,\theta) &= W_e(\theta,i) - W_{em}(\theta) - W_{cog}(\theta) - W_{iron}(\theta, d\theta/dt, i, di/dt) \\ &= \int i d\Psi(\theta,i) - W_{em}(\theta) - W_{cog}(\theta) - W_{iron}(\theta, d\theta/dt, i, di/dt) \end{aligned} \tag{3.5}$$

W_{em} is the energy delivered to the mechanical subsystem of the machine from the magnetic subsystem.

W_{cog} is the energy stored in the magnets. If the load of the magnet is changed, ie. by varying the air-gap, the stored energy of the magnet would change, which gives rise to cogging torque (permanent magnet reluctance torque). The stored energy in the magnet also depends on temperature, but in this dynamic model the temperature is fixed to the operating temperature. This limitation is not critical because of the large time-constant in the thermal system of the motor.[51]

W_{iron} represent the iron-losses (eddy current losses, hysteresis losses, and excess losses), which are dependent on phase current, change in phase current, the rotor angle, and the change

in rotor angle. These parameters are linked to the flux levels in the HSRM and the changes in the flux levels in the HSRM. The losses may the be approximated by e.g. the Steinmetz equation based on results from calculated flux densities in various sections of the HSRM based on finite element models. The iron loss model would have limited impact on the dynamic behaviour of the HSRM model, since other losses are dominant (copper losses and Coulumb losses in the bearings), so it is omitted from this HSRM model.

At this stage the iron losses are ignored:

$$W_{field}(\Psi,\theta) = \int_0^{\Psi} i(\theta,\chi)d\chi - W_{em}(\theta) - W_{cog}(\theta) \tag{3.6}$$

The co-energy is defined as [52][51][22]:

$$W_{co} = i\cdot\Psi(\theta,i) - W_{field} = \int_0^{i} \Psi(\theta,\chi))d\chi \tag{3.7}$$

where χ is a substitute integration variable.

The mechanical equation is given by:

$$\tau_{em} - \tau_{load} - \tau_{friction} = J\cdot\frac{d\omega_m}{dt} \tag{3.8}$$

The electromagnetic torque calculation for a hybrid switched reluctance motor is given based on Fig. 3.6.

The field energy for a specific current level (i_{max}), with a fixed rotor angle θ is given by[5]:

$$W_{field} = i_{max}\cdot\Psi(\theta,i_{max}) - W_{co} \tag{3.9}$$

where W_{co} is the co-energy.

The co-energy is calculated slightly different from a normal switched reluctance motor, since the integral has to consider the bias introduced by the permanent magnets. To give a valid integral the flux linkage curve in Fig. 3.6 from point A to point B and also the flux linkage curve from D

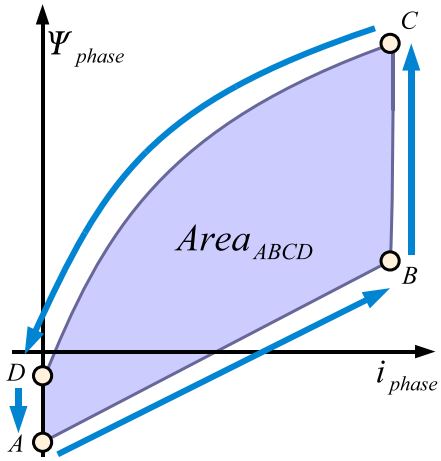

Figure 3.6: Energy conversion work cycle for a single phase HSRM in a single stroke is derived based on difference in co-energy in aligned and unaligned position.

to C has to be shifted into the firs quadrant. The bias is given as $\Psi_{bias} = \Psi(\theta_u, i = 0)$ and thus the co-energy can be calculated as the integral given in (3.10)

$$W_{co}(\theta) = \int_0^{i_{max}} (\Psi(\theta, \chi) + \Psi_{bias}(\theta)) d\chi \tag{3.10}$$

When current builds up the winding, the field energy ($W_{field,u}$) is found for a constant current i_{max} at the unaligned rotor angle (θ_u):

$$W_{field,u} = i_{max} \cdot \Psi(\theta_u, i_{max}) - \int_0^{i_{max}} (\Psi(\theta_u, \chi) + \Psi_{bias}(\theta)) d\chi \tag{3.11}$$

The current is kept constant as the rotor rotates to the aligned rotor positon (θ_a) and the energy injected into the magnetic field (W_{in}) is given by[5]:

$$W_e = i_{max} \cdot \Psi(\theta_a, i_{max}) - i_{max} \cdot \Psi(\theta_u, i_{max}) \tag{3.12}$$

Finally the field energy is put into the DC-link capacitor, when the winding is de-fluxed. The field energy thus stored in the DC-link is given by:

$$W_{field,a} = i_{max} \cdot \Psi(\theta_a, i_{max}) - \int_0^{i_{max}} (\Psi(\theta_a, \chi) + \Psi_{bias}(\theta)) d\chi \tag{3.13}$$

If the losses are ignored then the energy converted from the magnetic field energy to mechanical work must be given be the energy removed from the magnetic field. The energy that is removed

from the magnetic field is obtained by adding the energy injected in the field (equations (3.11) and (3.12), subtracting the energy put back into the DC-link(equation (3.13)):

$$W_{em} = W_{field,u} + W_{in} - W_{field,a} = W_{co}(\theta_a) - W_{co}(\theta_u) \tag{3.14}$$

In other words the area ($Area_{ABCD}$) gives the energy transferred to the mechanical subsystem during one stroke.

The instantaneous torque is then given by[5]:

$$\tau = \left.\frac{\partial W_{co}}{\partial \theta}\right|_{i=const} \tag{3.15}$$

The permanent magnets are placed in the fluxpath to make the unaligned flux linkage negative when there is no phase current. This increases the output torque production area, but the permanent magnets may also make the aligned flux linkage negative when there is no phase current. This can be seen in Fig. 3.6, as the point "‘c"’ lowers into the fourth quadrant if the aligned flux linkage is negative.

The energy calculation in (3.14) and the torque equation in (3.15), while they are important to illustrate the importance of magnetic bias, are however not practical for this dynamic simulation model. Instead the instantaneous torque is extracted from FEM as a look-up table based on phase current and angle. This means instantaneous torque is expressed as a function τ_m as it is done in (3.16)

$$\tau_m(\theta, i) = f_\tau(\theta, i) \tag{3.16}$$

3.2.4 Combined model for a HSRM

Combining (3.2), (3.3), and (3.16) with a general mechanical model the simulation equations can be stated as (3.17).

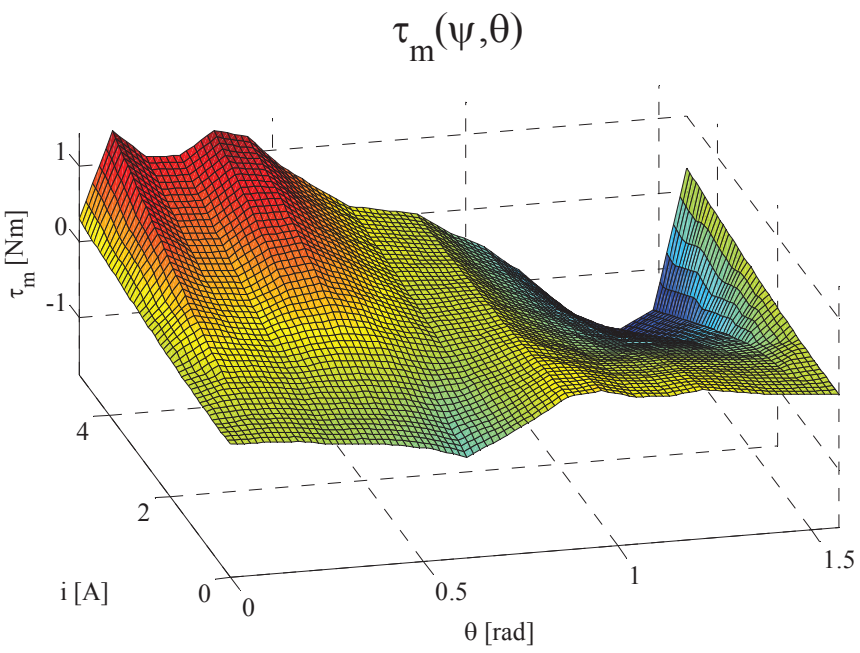

Figure 3.7: A plot of the look up table used for finding the torque as a function of the phase current and rotor angle. The data are from the first prototype motor presented in the next chapter.

$$\begin{bmatrix} \Psi \\ i \\ \omega \\ \theta \end{bmatrix} = \begin{bmatrix} \int (v - R \cdot i)\, dt + \Psi_{PM}(\theta) \\ f_i(\Psi, \theta) \\ \int \left(\frac{\tau_m(\theta, i) - B \cdot \omega - \tau_l}{J} \right) \\ \int (\omega)\, dt \end{bmatrix} \tag{3.17}$$

where Ψ is the phase flux linkage, v is applied phase voltage, R is the phase resistance, i is phase current, Ψ_{pm} is the angle (θ) dependent phase flux linkage from the permanent magnets, f_i is the a lookup function that links the coil flux and θ with i, $\tau_m(\theta, i)$ describes the generated motor torque, B is the Coulomb friction, ω is the mechanical speed, τ_l is the load torque, and J is the moment of inertia. Leakage inductance, power converter dynamics and static friction is not considered in (3.17), but is included in Simulink model presented in appendix C. For the simulations the pump loads are approximated with a simple approximation of a fan load as:$\tau_l = B_{fric} \cdot \omega^2$[53].

3.3 Converter for a single phase HSRM

The motor design and the control design may depend on the converter. For example sets converter the limits on how fast the current may be controlled. This section describes briefly the converter used to control the HSRM, since it did affect the design choices in the controller and the motor design.

Several converters for a single phase switched reluctance motor can be found in [54, 55, 56, 57, 58]. The standard asymmetrical halfbridge appears to be the single most used compromise for the single phase SRM. That the asymmetrical halfbridge is indeed used for commercial single phase SRM can be seen in Fairchilds integrated powermodule for vacuum-cleaners. It integrates high- and low-voltage ICs, IGBTs, fast recovery diodes, and a thermistor. The chip provides optocoupler-less, single-supply IGBT gate driving capability as well as under-voltage lock-out and short-circuit protection[59].

For this project another inverter is developed, where the main design criteria is performance and not cost. The schematic for the converter is shown in Fig. 3.8.

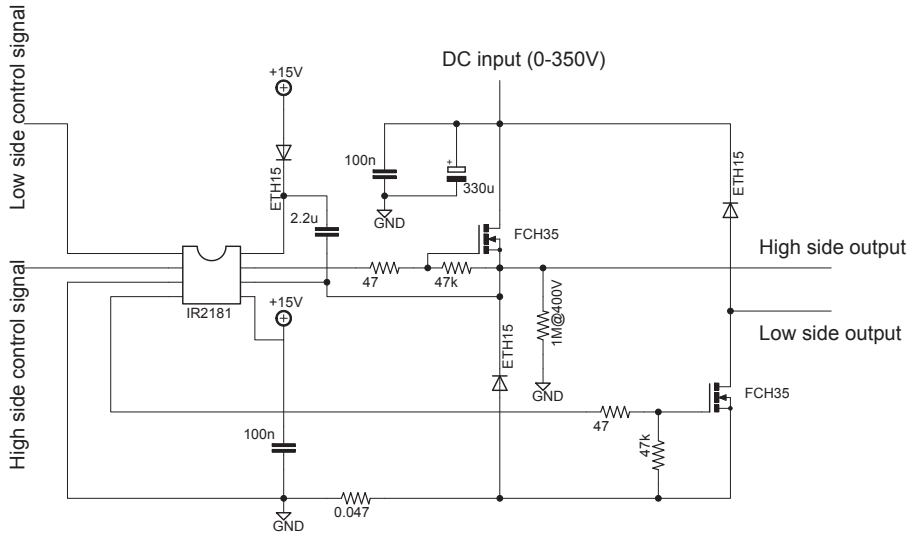

Figure 3.8: The key components for inverter used in this project. The over current protection, optical connection etc. are not shown on this schematic

The inverter uses two Fairchild MOSFET (FCH35N60) for 600V with an on-state resistance of

less than 100 mΩ. Their low on state gate charge and low equivalent drain-source capacitance allows for high frequency switching (in this project the typical switching frequency is 50 kHz). Both factors means that the losses in the converter are smaller than if IGBTs were applied as is the case for the integrated powermodule for SRM, in particular at a 50 kHz switching frequency. The reason for the relatively high switching frequency is explained in the motor control part. The switching frequency also requires sufficiently fast diodes to ensure low recovery losses. For this purpose 15ETH06 diodes are used, since they have a reverse recovery speed of approximately 15 ns. The inverter is connected with a TMS320F2812 DSP running at 150 MHz through an optical fibre link, which ensures electrical isolation between inverter and DSP. For a commercial low cost system isolation has to be removed and high performance components exchanged with low cost compromises. If the isolation between DSP and inverter is removed, the consumer has to be sufficiently isolated from all electrical components in the product. The inverter allows for a motor design with a low inductance, since the current may be shaped very quickly by the inverter.

A low cost version could be developed that would be in a similar price range as two commercially available pump motor drives if the required control algorithms are sufficiently simple.

3.4 Summary

This chapter presented the dynamical model of the single phase hybrid switched reluctance motor (HSRM) as it was used in this project. The model is verified in the chapters regarding control, since a HSRM can not run without control. Finally the asymmetrical half bridge inverter used in the project was presented, that enables use of a switching frequency of 50 kHz without excessive losses.

Chapter 4

HSRM Design

This chapter describes a few key points regarding the design of the first motor type regarding efficiency and starting torque. In total was two prototypes designed and manufactured for this project. The analysis of the hybrid switched reluctance motor will be laid on the first prototype. The first motor should ensure sufficient starting torque and this is achieved by asymmetrical shaping some of the stator poles. As it was described in the previous chapter, the permanent magnets are also important to achieve a good torque density for the motor. This is explored for different configurations of proposed magnetic flux concentration topologies. Flux concentration is used since ferrite magnets have good corrosion resistance, but also have low flux density when compared to high energy density permanent magnets such as sintered Neodymium-Iron-Boron (NdFeB) magnets.

The chapters starts by an overview of the specifications for this motor design, followed by an initial estimate of the size of the motor. The proposed motor and the design procedure is presented in general terms. The next sections in the chapter describes pole shaping, flux concentration design, and design validation using measurement results for this first prototype . A summary ends the chapter with some comments and conclusions for the first motor design.

4.1 Magnetic topology design flow

Motor design can be done in many different ways. The task is fundamentally to design a motor that fits the required specifications. If the motor design is a classical well understood motor type, like the induction motor, typically a simplified design procedures are available. One such simplified design procedure is to adjust a few key parameters of a known motor type and find an optimum for such a motor design. Such an approach used in e.g. [60],[61],[62], [63], [64], and [65]. Such an approach requires that the key parameters are well known and well documented or the design is relatively simple. Similarly if the magnetic topology is simple or well known, properties of the magnetic topology can be evaluated by describing the magnetic structure in the form of a network of lumped parameter magnetic components, also known as a magnetic reluctance network. When the magnetic structures do not have a predefined structure it becomes cumbersome to use magnetic reluctance networks for anything but preliminary analysis. Here the task is to make some structural changes to the magnetic topology and therefore the key parameters are not well known. This requires an approach that allows free definition of magnetic topologies to be used in this thesis.

The applied design methodology is directly using finite element simulation software in the iterative design process. The finite element software used in this project was David Meekers "'Finite Element Method Magnetics"' (FEMM)[66]. Unfortunately FEMM does not have facilities for solid geometry modelling. Solid modelling systems uses symbolic representations of "'abstract solids"' to model physical solids[67]. Specifically, FEMM simulation models are defined as a collections of curves, lines, nodes, and surfaces, which may not correspond to well-defined solid objects. Since well defined solids are not guaranteed, such a system may need human assistance to supply missing information and resolve inconsistencies[67], and therefore cannot support reliable and automatic generation of magnetic structures (magnetic topologies). Solid modelling tries to ensure that the integrity in the symbolic representation of an abstract solid is maintained even if a series of 2D-transformations are performed on the abstract solid. A solid modelling tool was written for this project as a series of Matlab commands, controlling a Delphi program for the actual solid modelling. FEMM supports scripting in the form of scripts based on Lua scripting

language. A Matlab script using the solid modelling commands was then used to generate a Lua script that could be executed in FEMM. The magnetic topology design flow is illustrated in Fig. 4.1.

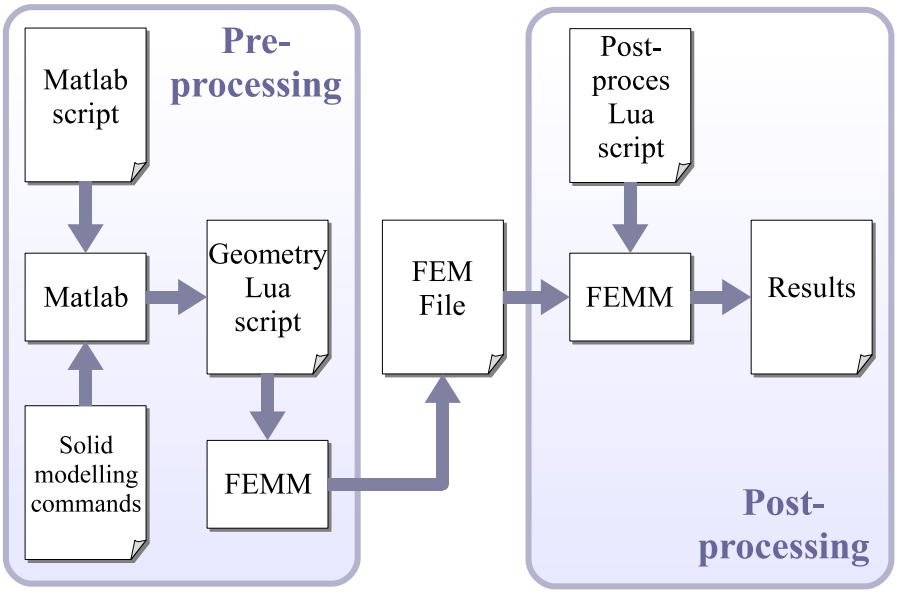

Figure 4.1: The design procedure is an iterative process where a geometry is evaluated and based on the results the geometry is modified. Using solid modelling, complex geometry can be defined in a Matlab script. The Matlab script uses a set of commands to generate a Lua-script which in turn generates a FEM file with the machine geometry. Based on the parameters of the post processing a series of finite element simulations are performed and the results are gathered in a single file. The single result file may be further processed to generate the lookup tables needed for a dynamic simulation.

To quickly evaluate the torque production from a design it is sufficient to evaluate the torque for different rotor angles with no current in the windings (cogging torque) and the torque for different rotor angles with maximum current in the windings (combined torque). Plotting these torque magnitudes on the same graph forms the limits of the torque envelope. The machine can only generate torque within this torque envelope, and all other current levels between zero current and maximum current will generate a torque within those limits. The cogging torque for a four pole rotor over one period of 90^o of mechanical rotation is zero as defined in (4.1)

$$\int_{0^o}^{90^o} (\tau_{cogging}(\theta))\, d\theta = 0 \tag{4.1}$$

The same applies for the combined torque and thus if the positive cogging torque or combined torque is increased, the consequence is an increased negative peak torque. The increased peak

torque also means that the change of torque production versus angle becomes steeper for the combined torque close to an angle of zero degrees. This has an impact for the control, and this will be discussed in chapter 6.

The permanent magnet coercivity (H_c) describes which load that the permanent magnets can sustain before they are permanently demagnetized. To avoid demagnetization, the state of the PMs needs to be evaluated. To do so two scripts are written, which respectively extracts the information from the FEM simulations, and checks for demagnetization in points in the PMs.

4.2 Specifications for first prototype

The goal is to design a prototype single phase hybrid switched reluctance motor with following specifications:

- The output power is $70\,\mathrm{W}$ at 3000 RPM to 4000 RPM, matching a small centrifugal pump. A main objective is to have a motor that under ideal conditions can compete regarding efficiency with three phase permanent magnet synchronous motors (PMSM) and three phase brushless DC-motors (BLDC) under equally ideal conditions. Since this is linked with the control design, the efficiency test are described in the next chapter regarding control.
- The motor should have starting torque of approximately the same as the average torque $\tau = 0.223\,\mathrm{N\,m}$.
- The motor should aim at getting a square shape, so simple bobbins may be used .
- Use flux concentration but avoid the segmented stator presented in [36].
- Unlike [5] and [68] only one type rotor lamination should be used to simplify construction.
- Square bobbins are to be used for this design, unlike [5, 68, 36]. This will also fit EU-WEEE recommendations of simplifying reuse[69], which may become mandatory for all drives.

4.3 Design of first prototype

These specification acts as guidelines for iterative motor design phase, and [36] is used as a starting point for this design. The first step is an initial guess of motor size, followed by iterative design of the magnetic topology evaluated in finite element simulations. See Appendix A for flux plots of the motor at parked and aligned position at both full current and no current.

4.3.1 Initial motor sizing

For an arbitrary motor with permanent magnets the ratio of the torque (τ) to the volume for the permanent magnets (V_{magnet}) multiplied with fourth root of the rotor diameter ($D_{rotor}^{1/4}$) has approximately a fixed ratio as it was found in [70], with the assumption that the magnets are of a similar type. The output power has to be approximately $70\,\mathrm{W}$ at 3000 RPM. This gives an output torque of approximately $0.22\,\mathrm{Nm}$. As an initial guess of the size it is convenient to use an existing motor design as initial guess. For this design a brushless DC-motor with ferrite magnets has an output torque of $0.16\,\mathrm{Nm}$ at 3000 RPM, with a rotor diameter (D_{rotor}) of $46\,\mathrm{mm}$ and a permanent magnet volume of $11.4\,\mu\mathrm{m}^3$ presented in [70]. The outer size limit is guessed to be 100 mm, and the rotor diameter is thus limited to less than half and here this guess is set at $50\,\mathrm{mm}$. If two magnets with a size of 30 mm x 10 mm x 30 mm are used their total volume is close to $20\,\mu\mathrm{m}^3$.

$$K_{motor} = \frac{\tau}{V_{magnet} \cdot D_{rotor}^{1/4}} = 30306 \tag{4.2}$$

For this motor with C5 magnets, a magnet volume of approximately $0.2\,\mu\mathrm{m}^3$, and a 5 cm diameter rotor the torque is approximately given in (4.3)

$$K_{motor} \cdot V_{magnet} \cdot D_{rotor}^{1/4} = \tau = 0.28\,\mathrm{Nm} \tag{4.3}$$

This means that the output power at $3000RPM$ for an initial design is approximately $\tau \cdot \omega = 88\,\mathrm{W}$.

The output torque may also be estimated based on (4.4)[61] for a totally enclosed DC-motor.

$$\frac{D_{rotor}^2 \cdot l_{stack}}{V_T} = \tau \tag{4.4}$$

where l_{stack} is stack length and V_T is a coefficient found based on output power and cooling. For this motor $V_T \approx 0.33\,\mathrm{mm}^3/\mathrm{Nm}$ based on the dimensions for the brushless DC-motor. The output torque is then given in (4.5)

$$\tau = \frac{0.05^2 \cdot 0.03}{0.33 \cdot 10^{-3}} = 0.2268 \tag{4.5}$$

This guess implies an output power of 71 W at 3000 RPM.

So the initial guess for the sizes for the motor is:

D_{rotor} =50 mm

l_{stack} =30 mm

D_{stator} =0.1 mm

where D_{stator} is the outside length of the stator.

4.3.2 Proposed hybrid switched reluctance motor

The machine has six poles on the stator side, two permanent magnet poles (PM-poles) and four reluctance poles. The rotor has four poles with a saturable saliency. This ensures that the rotor is parked by the permanent magnets at a known rotor angle when there is no phase current. Refer to Fig. 4.2 for details on parking. When the two series connected coils are energized, a flux is generated that opposes the flux from the permanent magnets and thus attracts the rotor poles to the reluctance poles. When the coil is defluxed and the phase current becomes zero, the process repeats as the permanent magnet poles attract the rotor. The motor has a square frame that allows square bobbins to be inserted before the rotor is inserted, simplifying assembly. To ensure that the machine only operates in the desired direction, the rotor has to be parked within certain angles.

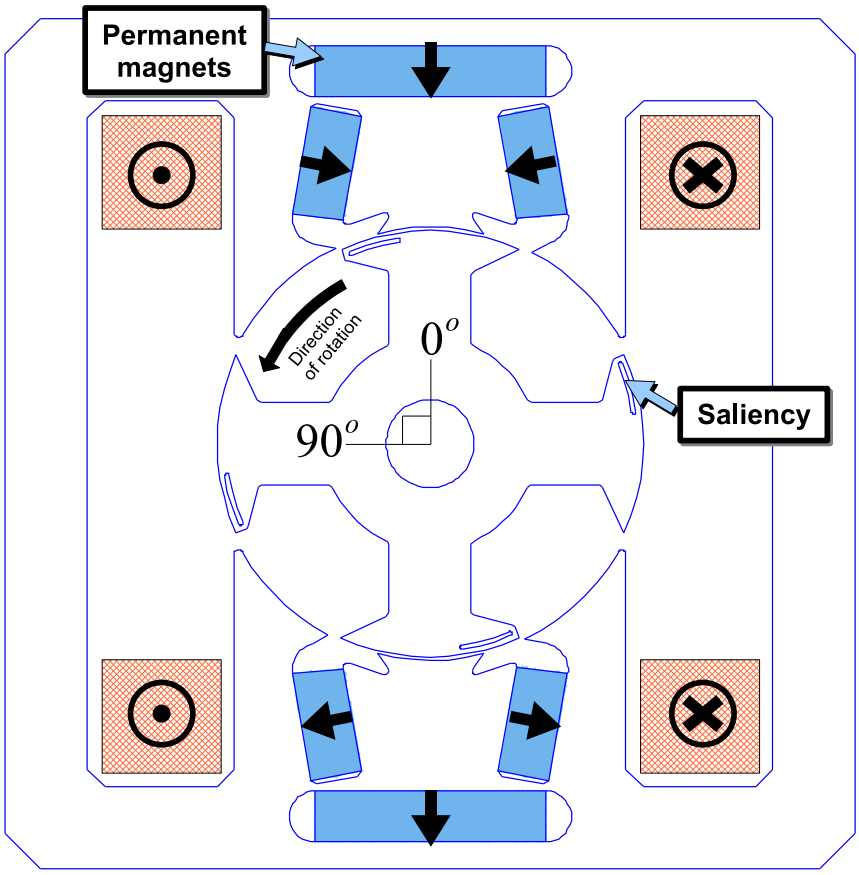

Figure 4.2: Proposed motor, here with rotor shown at an angle of 0 degrees. Circles enclosing either dots or crosses indicate the direction the coil current. Thick black arrows indicate magnetization direction of the permanent magnets.

Pole arcs

The single phase HSRM motor is actually a two phase motor with a pseudo phase with the magnetic flux supplied by the permanent magnets. The rotor and stator pole arcs can thus to some extend be found as for the switched reluctance motor. Four of the stator poles are not directly linked with the permanent magnets. These four stator poles and the rotor poles can initially be designed as for a normal SRM, with the arc angles as seen in Fig. 4.3. The sizing of the permanent magnet poles is described in [36].

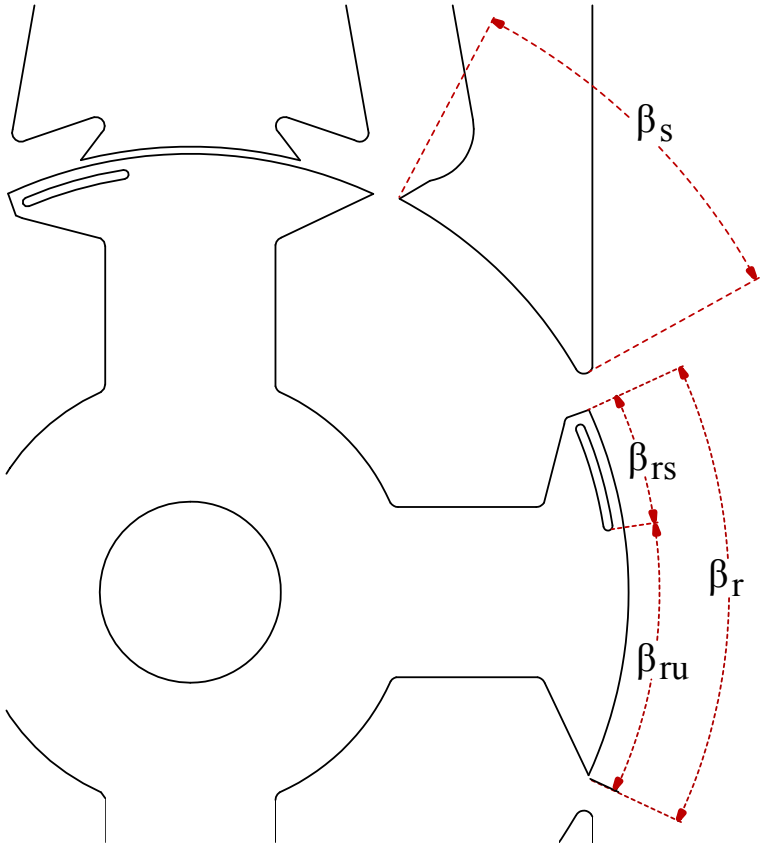

Figure 4.3: The reluctance stator pole arcs and the rotor pole arcs of the HSRM.

The minimum stator arc ($min(\beta_s)$) can be found based on the number of rotor poles ($P_r = 4$) and the number of stator poles ($P_s = 8$). It should be mentioned that two of the stator poles are "missing", since these permanent magnet stator poles would prohibit the simple coil insertion. The minimum stator arc is found in (4.6) as given in [63].

$$min(\beta_s) = \frac{2 \cdot 360}{P_r \cdot P_s} = 22.5^\circ \tag{4.6}$$

The maximum stator pole arc is given by the rotor pole arc (β_r):

$$max(\beta_s) = \frac{360}{P_r} - \beta_r \leq \frac{360}{P_s} = 45^\circ \tag{4.7}$$

Due to the saturated piece of iron over the slot, the rotor will align the unsaturated part of the rotor with the stator. The arc of the unsaturated part of the rotor (β_{ru}) should then be approximately equal to the stator pole arc (β_s). The arc length of the saturated part of the rotor (β_{rs}) is then given by [71]:

$$\beta_s \approx \beta_{ru} \leq \frac{360}{P_r} - \beta_{ru} - \beta_{rs} \tag{4.8}$$

An initial guess for the lenght of the stator arc could then be:

$$\beta_s = \frac{max(\beta_s) + min(\beta_s)}{2} \approx 34^\circ \tag{4.9}$$

Assuming $\beta_s \approx \beta_{ru}$ in (4.8) gives an upper boundary for β_{rs}:

$$max(\beta_{rs}) \leq \frac{360}{P_r} - 2 \cdot \beta_s = 22^\circ \tag{4.10}$$

Assuming $\beta_s \approx \beta_{ru}$ in (4.8) gives an lower boundary for β_{rs}:

$$min(\beta_{rs}) \geq \beta_s - \frac{360}{2 \cdot P_r} = 11^\circ \tag{4.11}$$

An initial guess for the length of the saturated pole arc could then be:

$$\beta_{rs} = \frac{max(\beta_{rs}) + min(\beta_{rs})}{2} \approx 16^\circ \tag{4.12}$$

For single phase reluctance machines, saturating parts of the rotor poles may have extended the range of angles where the motor can generate positive torque[71]. Like the design presented in [36] this motor cannot use a stepped airgap for the rotor design as presented in e.g. [30]. The rotor has to be cast with concrete and a stepped airgap is not a suitable structure for concrete casting. The first prototype uses holes to achieve saturation of parts of the rotor poles, since a stepped airgap rotor is not possible due to the increased hydraulic losses a stepped airgap rotor would cause. The iron above the slot as seen in Fig. 4.4, should be as small as possible, since a thin piece of iron more easily saturates. But manufacturing limits the minimum thickness to 0.6 mm and the slot width to 0.5 mm as seen in Fig. 4.4.

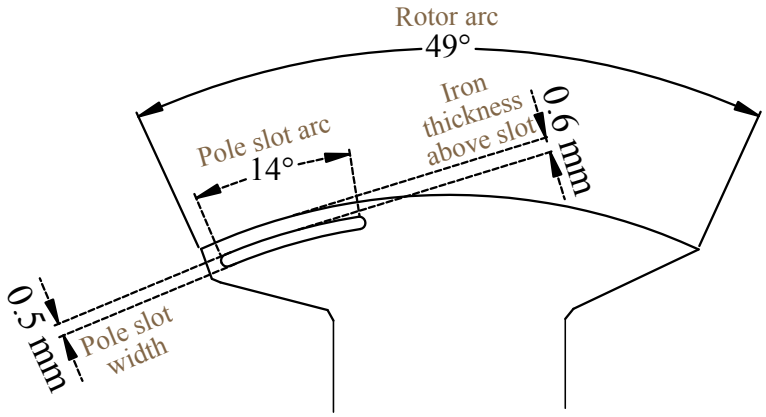

Figure 4.4: The pole slot width and the thickness of iron over the pole slot are key features that determine the degree of saturation on the rotor tip.

4.3.3 Improved starting using stator poleshaping

In a pump drive, the rotor may be parked in the same position for a long time. Particles may get stuck in the airgap between rotor and stator. If the particles are sufficiently stuck, starting torque may need to be higher than usual[72]. It is assumed that the full average torque ($0.223\,\mathrm{N\,m}$) is sufficient as starting torque, since a similar BLDC for a centrifugal pump at 50 W at 4000 RPM has no starting issues. This means that cogging torque must ensure that the rotor is parked in a position where the combined torque is high enough. Another related design requirement is that at no point shall both the combined torque and the cogging torque be zero at the same angle.

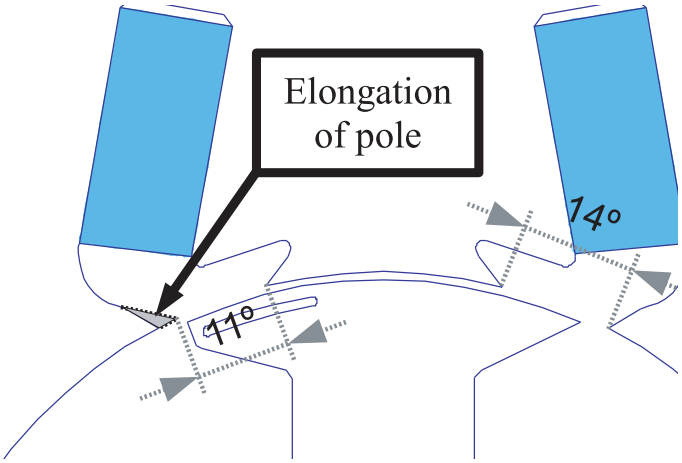

Figure 4.5: Two of the four reluctance poles are elongated, so the stator poles are no longer axially symmetric

The saliency in the rotor poles makes the rotor park at an angle of 1-5 degrees depending on the static friction.

To have enough starting torque is an important issue in the design of a single-phase machine [73], [74]. The normal way used to increase the starting torque is to optimize the rotor pole-arc [74]. By changing the rotor pole-arc, the starting torque will be changed, but at the same time, the average reluctance torque generated, and the cogging torque available in HSR, is also affected. Therefore to optimize the starting torque based on the rotor pole design will require extra considerations on other torque production issues, which will make the design process more complicated. An easy way to control independently the starting torque is to extend the stator reluctance pole-arc, as illustrated in Fig. 4.5 for one of the stator reluctance poles. Pole-arc

extension may only need to be done for two of the stator reluctance poles that are opposite to each other to balance the radial force. The shape of the stator permanent magnet poles and the rotor poles is not changed. Therefore, extension of the reluctance pole-arc has little effect on the cogging torque. For this HSR machine, the stator reluctance pole-arc is increased by 3 degrees (9% increase). This increase affects slightly the average output torque ($<$ 1% change in the average output torque), and has almost no influence on the cogging torque. But the starting torque at the unaligned position is increased from less than 0.1 Nm to 0.25 Nm for this machine, which is more than 150% increase, as demonstrated in Fig. 4.8.

When the stator coil is energized at a rotor angle of zero degrees (unaligned position), more magnetic flux will flow through the rotor as it can be seen in Fig. 4.6. However when the rotor is aligned with the main reluctance poles, the situation does not change significantly, as it can also be seen in Fig. 4.6. Since the main flux sources for the cogging torque are the permanent magnets and the flux from the permanent magnet mainly flows from the permanent magnet stator poles, the cogging torque is only slightly affected.

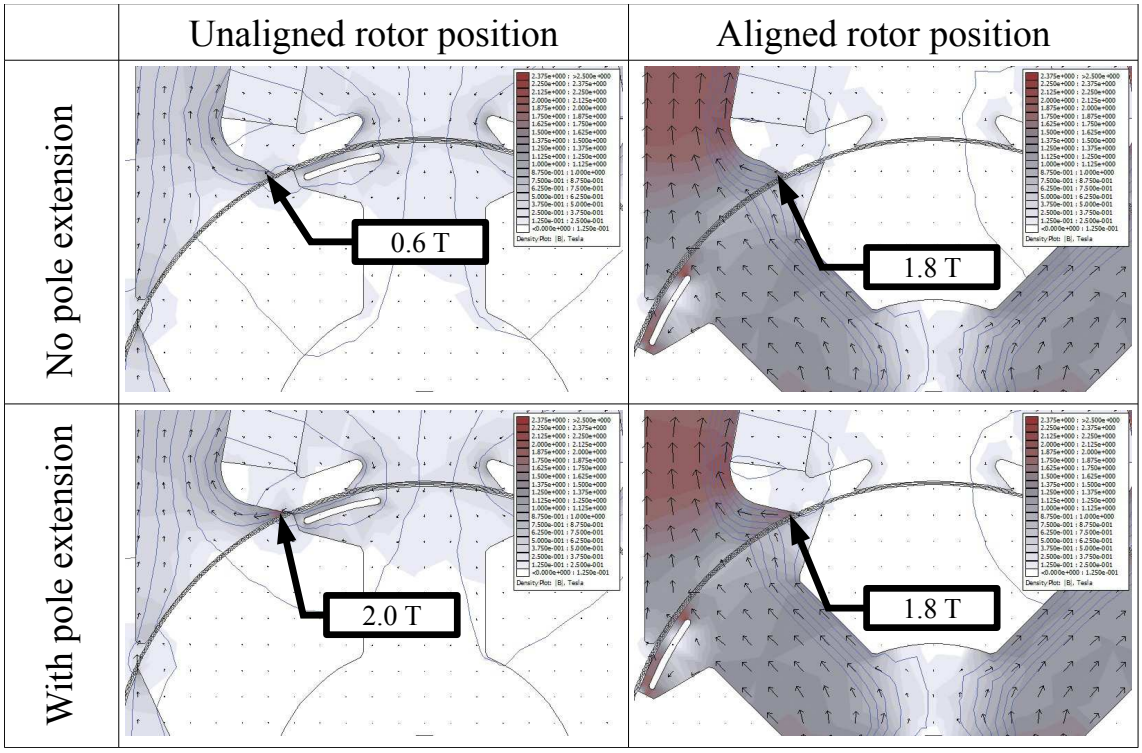

*Figure 4.6: The figure shows a finite element simulation of the motor, and the phase current is set at the maximum current (*4 A*).*

The pole extension increases the combined torque at 0 degrees from less than 0.1Nm to 0.25Nm. In total this improves the starting torque in the region from -0.5 to 3.5 degrees. The pole elongation has little impact on cogging torque and output power as may be observed from Fig. 4.7.

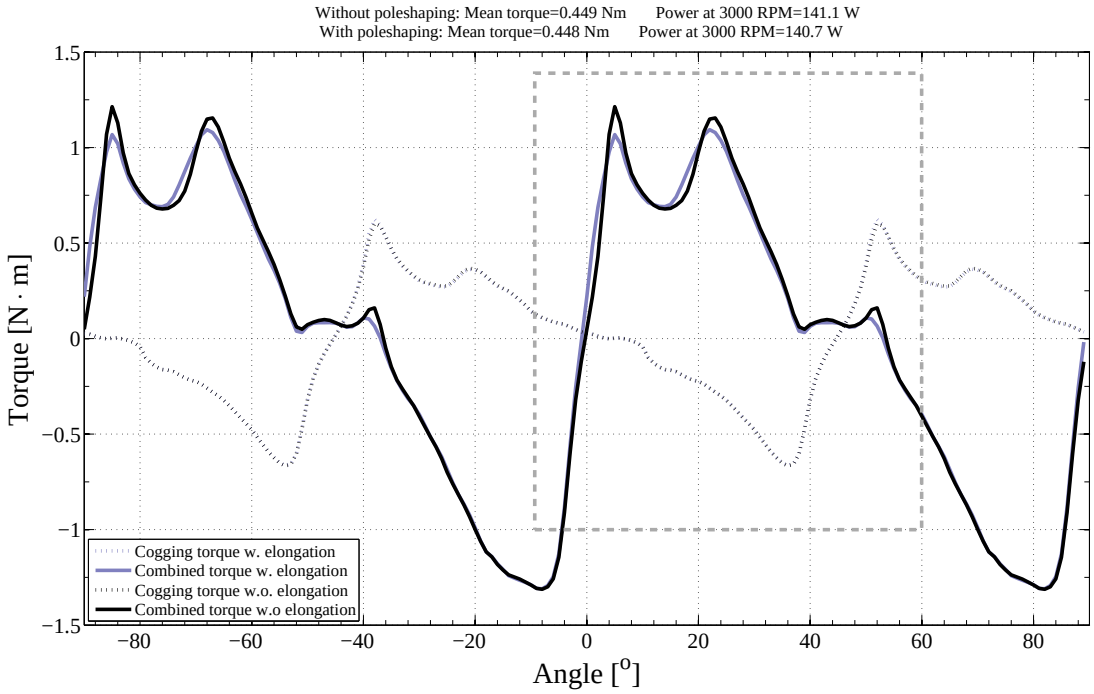

Figure 4.7: The torque production from the cogging (phase current=0A) and the combined torque (phase current=4A), with and without the pole elongation. The dashed area is shown in detail in Fig. 4.8

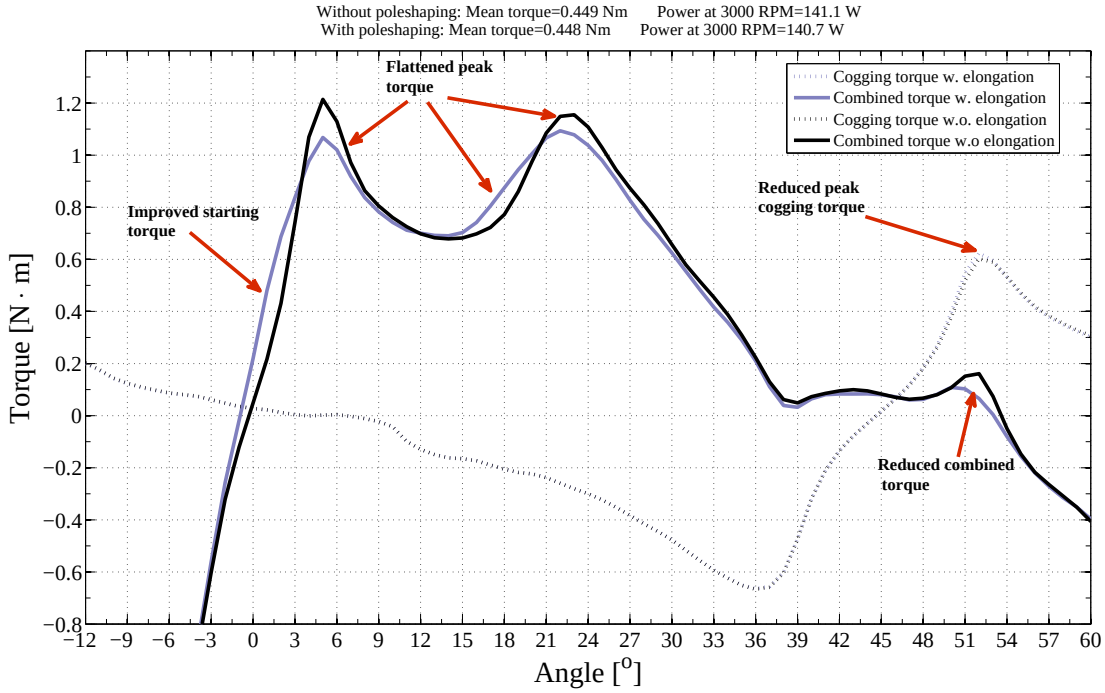

Figure 4.8: Zoom of Fig. 4.7 in the region near the parking region of 1 to 5 degrees. The starting torque is improved in the region from -0.5 to 3.5 degrees. The cogging torque with pole elongation is identical to the cogging torque without pole elongation, and the two curves thus overlap.

4.3.4 Output torque improvement using flux concentration with ferrite magnets

A way to evaluate and compare different designs is to compare output average torque for different configurations of permanent magnet flux concentration structures. In the previous chapter it was stated that the permanent magnet bias flux directly increases the torque production. The task in this section is to use flux concentration of the permanent magnet flux to improve the output torque.

Simulation has shown that the peak magnetic flux density in the airgap under the permanent magnet pole was approximately $0.5\,\mathrm{T}$ in the design presented in [36]. Increasing the flux density may also saturate parts of the motor and since the flux from the coil interacts with the flux from the permanent magnets, the saturation knee-point is also influenced by the flux concentration arrangement. This influence can be seen in the aligned and unaligned flux linkage graphs, also presented in this section.

The specifications required a square stator frame, and this puts a limit on the possible permanent magnet dimensions. A stator designed with four permanent magnets in a configuration similar to [36] is discussed later in this chapter.Another possibility is to use six permanent magnets, three per flux concentration.

Flux concentration with six magnets

Three different permanent magnet arrangements (A,B, and C), shown in Fig. 4.9, are presented here that concentrates the flux in the air gap under the permanent magnet pole (PM-pole).

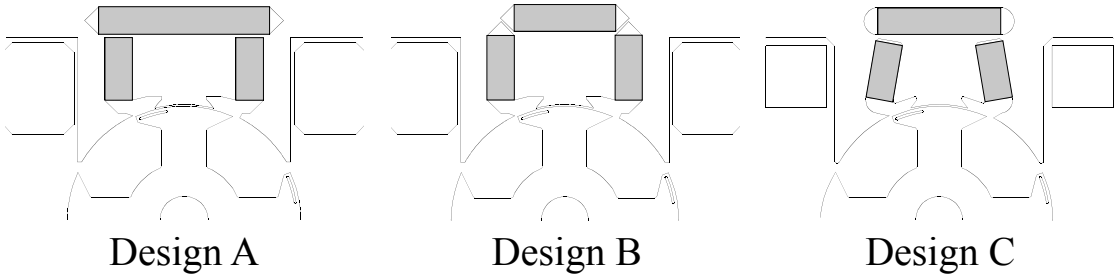

Figure 4.9: Three flux concentrating arrangements of permanent magnets evaluated. The magnetization direction is like in the previous designs. Pole elongation is also kept for all designs

The minimum and maximum flux linkages and torque profiles for design A, B, and C are shown in Fig. 4.10, Fig. 4.11, and Fig. 4.12 respectively. The average torque is calculated by averaging the maximum of either cogging torque or combined torque at any angle. Based on the average torque, the theoretical maximum output power is calculated by multiplying the average torque by the rated speed, which here is 3000 RPM. The current is assumed to be fixed at 4 A for the combined torque.

Design A, with FEA simulation results shown on Fig. 4.10, has lower output power than the two other designs. The lower output torque is partly because design A starts to saturate at low current levels. The finite element analysis showed that a higher phase current was needed to produce positive output torque, but the analysis also showed that the magnets would be damaged by the higher currents. This design (A) uses more PM material than design B and design C.

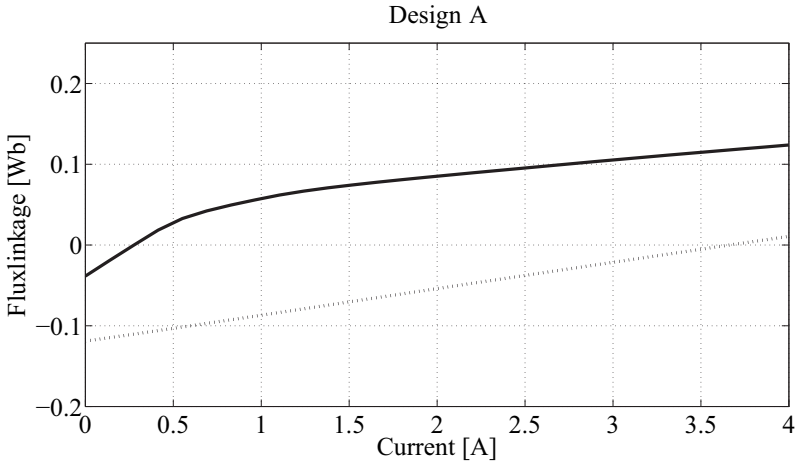

(a) flux linkage for unaligned and aligned rotor position. The full line indicates flux linkage when the rotor is aligned with coil reluctance poles, and the dotted line indicate flux linkage when the rotor is unaligned with the coil reluctance poles.

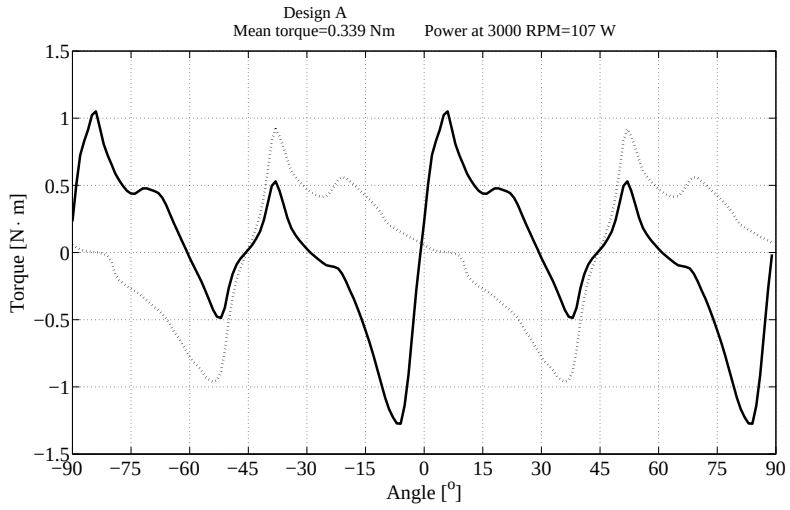

(b) The torque production from the cogging (phase current=0A, dotted line) and the combined torque (phase current=4A, full line), for design A

Figure 4.10: Flux linkage and torque profile for the design A from FEA

Design B is an improvement of design A, but design B is not able to produce positive torque for an entire stroke and still saturates at lower current levels than design C. Design B has a bigger offset between negative and positive flux linkage than design C, but also has a lower knee point. This explains why design B, despite the bigger offset, has no better torque production than design C, since saturation lowers the area covered in the energy production cycle. The mechanical structure of the flux concentration in design B is also problematic, since a thin piece of iron between the magnets has to withstand the normal force on the permanent magnet pole. However a thicker piece of iron between the permanent magnets would increase leakage of permanent magnet flux in the flux concentration.

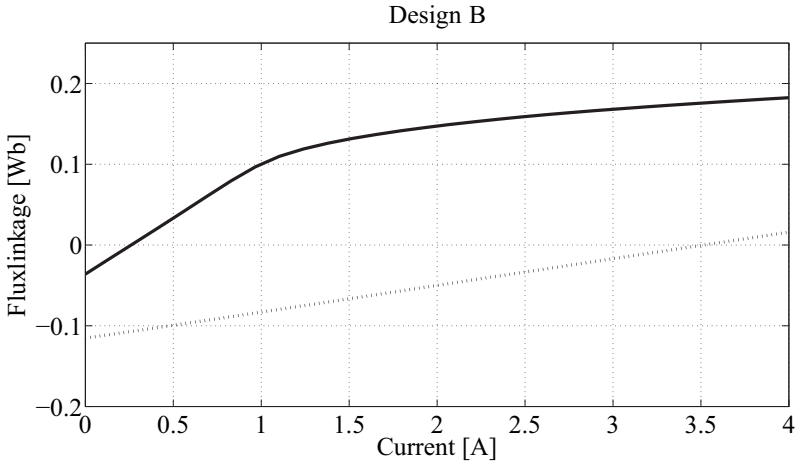

(a) flux linkage for unaligned and aligned rotor position. The full line indicates flux linkage when the rotor is aligned with coil reluctance poles, and the dotted line indicate flux linkage when the rotor is unaligned with the coil reluctance poles.

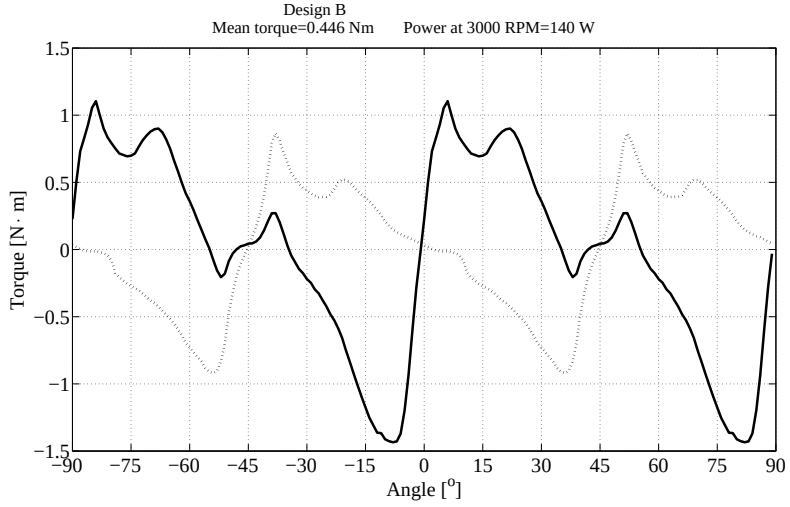

(b) The torque production from the cogging (phase current=0A, dotted line) and the combined torque (phase current=4A, full line), for design B

Figure 4.11: Flux linkage and torque profile for design B from FEA

An improvement to design B, would be to reduce the amount of negative torque, increase the saturation knee point, and improve the structural strength. To reduce the negative torque and increase the saturation knee point it is actually better to have lower flux density in the air gap. The lower flux density in the air gap means that key parts of the stator are not saturated as easily as before as it is seen in Fig. 4.12. The lower flux density also decrease the cogging torque and thus decreases the negative torque production. This also lowers the positive cogging torque, but the torque profile shows that design C can theoretically produce positive torque for an entire stroke. The structural strength is improved in this design since the thin pieces of iron supporting the PM-pole are shorter and thicker. Design C is implemented in the first prototype as it will described in the next section.

The peak flux density for design C in the airgap is approximately $0.8\,\mathrm{T}$ and influences the magnitude of the rotor position dependent flux linkage as discussed in the next section.

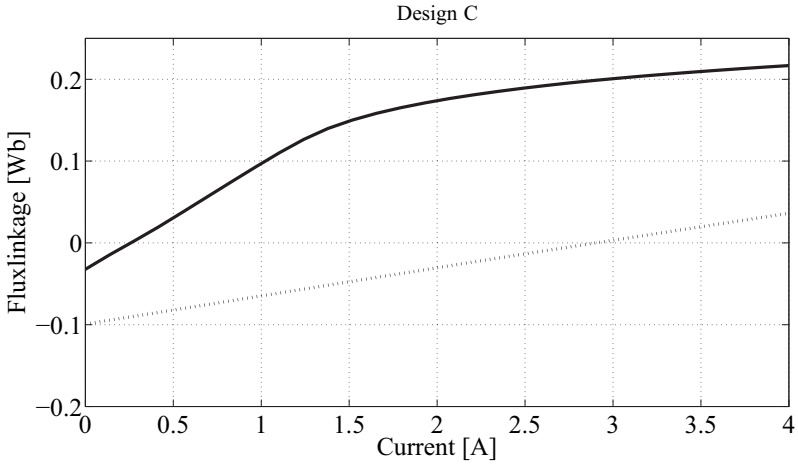

(a) flux linkage for unaligned and aligned rotor position. The full line indicates flux linkage when the rotor is aligned with coil reluctance poles, and the dotted line indicate flux linkage when the rotor is unaligned with the coil reluctance poles.

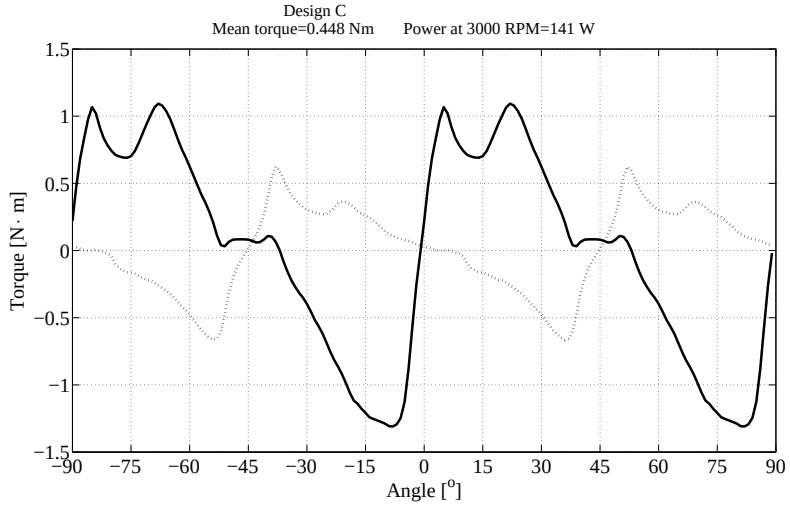

(b) The torque production from the cogging (phase current=0A, dotted line) and the combined torque (phase current=4A, full line), for design C

Figure 4.12: Flux linkage and torque profile for design C from FEA

Flux concentration with four magnets

The permanent magnet flux is beneficially used in the HSRM to improve the machine performance. Therefore it is important to improve the magnetic field generated by the magnets. In [36], v-shape flux concentration structure was used. In order to reduce the leakage flux at the top ends of the magnets, it was needed to remove the iron core back above the magnets as the design presented in [36]. However, this will result in a weak mechanical stator structure, compared to a solid stator construction.

Torque density for a HSRM may be increased if the flux linkage is increased when the rotor poles are unaligned with the four reluctance poles, without increasing the flux linkage at the aligned position. To visualize the effectiveness of the π-shape flux concentration in design C, a v-shape flux concentration design, similar to [36], was carried out as seen in Fig. 4.13. .

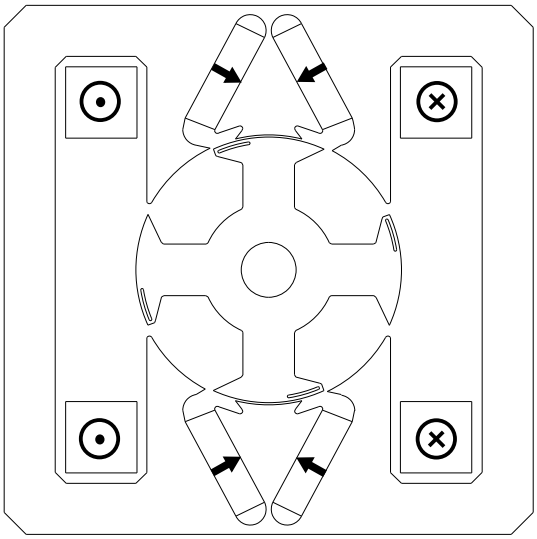

Figure 4.13: A v-shaped flux concentration arrangement for a HSRM

The PM flux linkage vs. rotor position profiles obtained from FEM for the v-shape flux concentration design, and for this π-shape design, are shown in Fig. 4.14.

It may be observed from Fig. 4.14 that at around 45°, the PM flux linkage values generated by the v-shape flux concentration structure and by the ?-shape flux concentration structure, are very close to each other. At this position, the rotor poles are under the stator reluctance poles. The large air gap under the stator permanent magnet pole dominates the reluctance and these

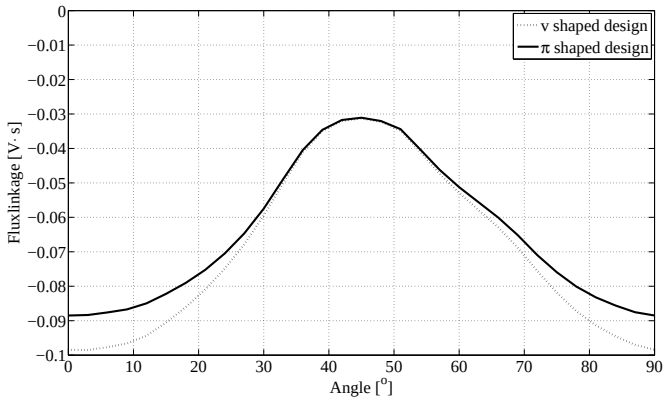

Figure 4.14: Comparison of the PM flux linkage vs. rotor position profiles for the v-shape flux concentration design vs. the π-shape flux concentration design

two different flux concentration structures generate almost the same amount of flux linking the winding. But at the position where two of the rotor poles are aligned with the stator permanent magnet poles (at 0°), the π-shape flux concentration design produces much higher flux linking the winding than that generated by the v-shape flux concentration design. The peak-to-peak value of the PM flux linkage generated by the ?-shape flux concentration design is 16.5 % higher than that generated by the v-shape design. The π-shape flux concentration design is more effective in generation of useful flux components, for improving the cogging torque and the motor efficiency.

4.4 Implementation of first prototype

Design C with pole elongation is implemented as it can be seen on Fig. 4.18. The prototype motor can be seen assembled on Fig. 4.19.

4.4.1 Coil implementation

The coils uses square bobbins wound with wires in parallel using a mechanical coil winder. The more strands, the lower resistance but also higher copper consumption. For practical reasons three strands of 0.355 mm copper wire was used.

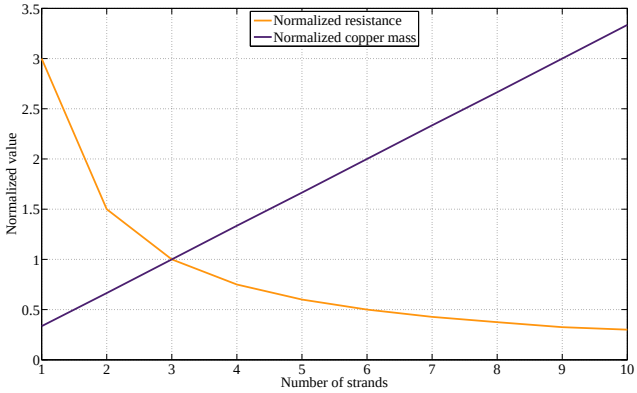

Figure 4.15: The coils were wound using three wires in parallel giving a resistance of 4 Ω. *This plot shows the normalized resistance and weight of the coils for different number of parallel strands.*

If the other losses are not considered then an upper boundary for the maximum efficiency the motor can theoretically achieve is set by the copper losses and the relationship between number of parallel strands can be seen in Fig. 4.16. The current is assumed to be pure square waves and The maximum efficiency thus will be lower than 85 % for the HSRM at 141W output power with only copper losses considered.

The coils are finally coated with a polyester-lacquer and baked in an oven to harden the coils. The baking should reduce the vibrations from the coils and thus may reduce noise from coils.

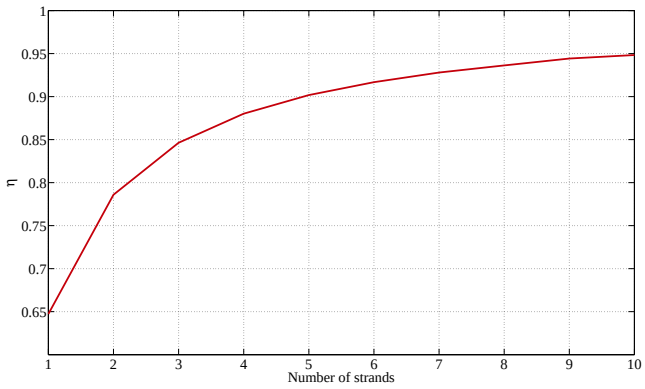

Figure 4.16: This plot shows maximum efficiency, ignoring other all sources of loss except copper losses, for different number of parallel strands.

4.4.2 Estimation of losses

To estimate the losses for the HSRM, four working points are chosen at 3000 *RPM* with a quadratic torque load with an output power of $P_{out} = (17.5, 35, 70, 141)$ W.

The bearing losses are assumed to consist two components a static torque of approx. 5 mNm and a Coulomb friction loss of approx. $9.6 \cdot 10^{-6}$ Nm·s/rad. It is assumed that for a certain unspecified combination of turn and turn off angles, the torque output is linear with current. The peak flux density in the stator core back is assumed to be linear with current[1]. The iron losses are estimated using a simplified estimation of the losses. The motor is dominated by a large stator back, where most of the iron volume is present. So the iron losses are estimated assuming that the peak flux density of the iron back is valid for the entire iron volume. Several empiric formulas exist for predicting iron losses. The one used here was presented in [75]. The loss formula is:

$$P_{Fe} = a \cdot f \cdot \hat{B}^x + b \cdot f^2 \cdot \hat{B}^2 + e \cdot f^{1.5} \cdot \hat{B}^{1.5} \tag{4.13}$$

where a, b, e, x are specific material coefficients, f is the frequency of the magnetic field, and $\hat{B}$ is the peak flux density. The constants used are also from [75] for 0.35 mm steel, with a specific loss at 50 Hz and 1.5 T of 2.7 W/kg, where $a = 0.0183$,$b = 0.000077$, $e = 0.0$, $x = 1.92$. The peak flux

[1]This is not correct for low currents since the negative flux linkage, caused by the permanent magnets, is somewhat independent of the phase current.

density in the stator back is found to be approximately $\hat{B} = 0.6$ T. The iron losses are calculated for the first five harmonic components of the flux plus the fundamental flux component.

The efficiency of the motor is affected by the nature of losses, since the current and iron losses are (almost) quadratic with current. At a high load torque, the motor peak efficiency lies at a lower speed. When the load torque is low, the motor peak efficiency lies at speeds beyond 3000 RPM. This can clearly be seen in the efficiency plots seen in Fig. 4.17.

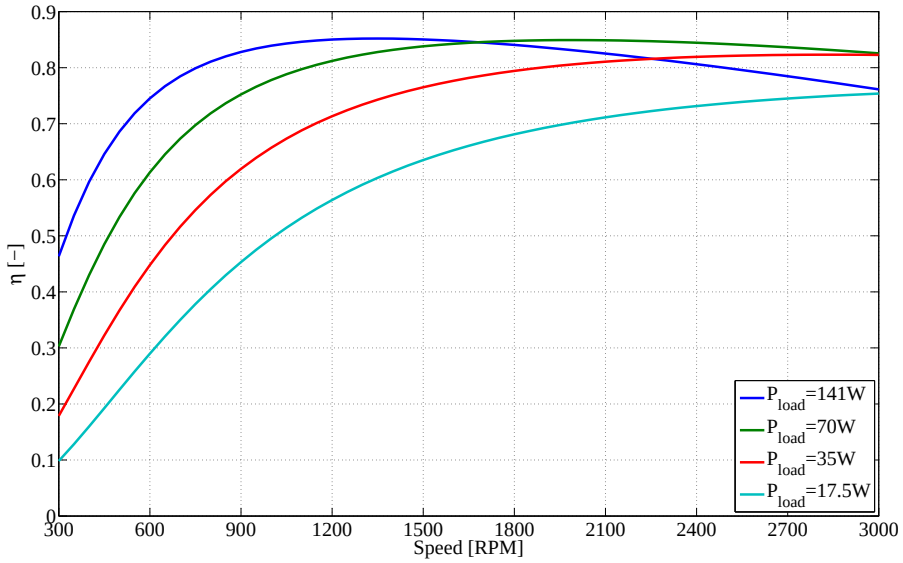

Figure 4.17: The efficiency as a function of load and speed

4.4.3 Motor assembly

To further reduce frictional losses, the rotor is filled with concrete before it is mounted on the motor shaft. The permanent magnets are glued and inserted into the stator, as shown in Fig. 4.18, before final assembly in the test frame. The final assembly is then done in a few steps: First the stator is mounted in the test frame, secondly the coils are inserted in the stator and finally the rotor is inserted in to the test frame. The assembled motor can be seen in Fig. 4.19.

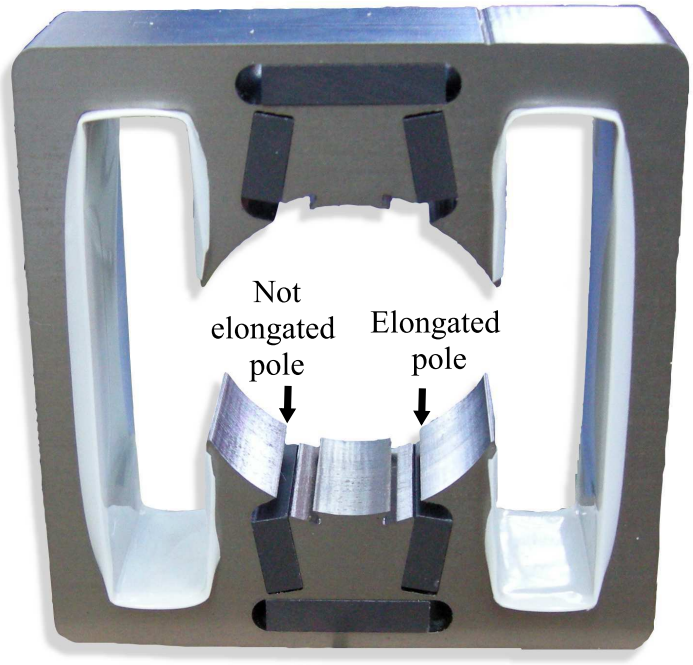

Figure 4.18: The stator is here shown with magnets glued to the stator before the coils and the rotor is inserted. The difference between the two stator poles controlled by the coils are visible in particular in the lower part of the stator.

The test frame allows for easy assembly and disassembly, but does not have the structural strength of a standard motor housing. The motor in its test frame would therefore be more noisy than a motor mounted in a standard motor housing. A standard motor housing is used for the second prototype.

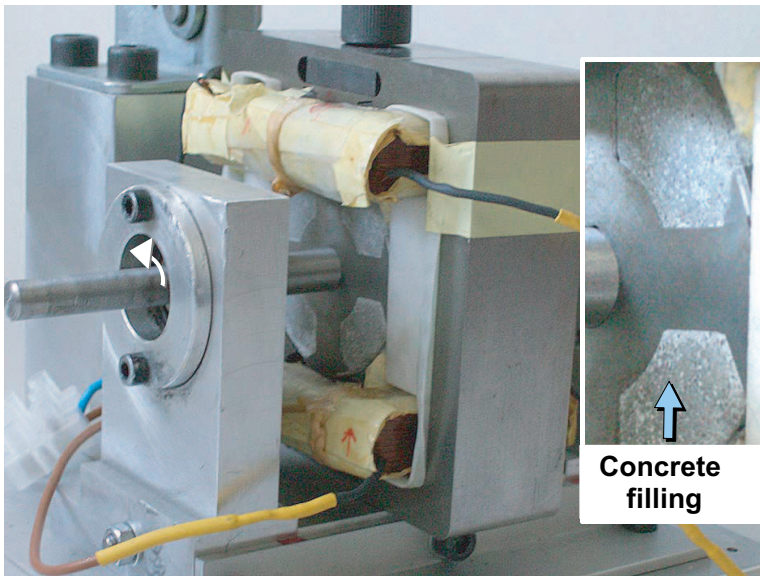

Figure 4.19: The prototype motor in its test frame. The rotor is here parked at an angle of approximately 4 degrees.

4.5 Measurement Results on The Prototype Motor

Two static measurements are done for the first prototype and presented in this section: flux linkage measurement and static torque measurement. The measurement of the dynamic performance of the first prototype is presented in the next part describing how the motor is controlled. The measurement set-ups used for measuring static torque and flux linkage are described in appendix D.

The flux linkage measurement result for the prototype is shown on Fig. 4.20. The FEA model is a 2D model that does not include the end-effects. An approximately constant leakage inductance is used to model this difference in the motor model. The bias caused by the permanent magnets are added to the curves in Fig. 4.20, but they are obtained from the FEA model. This means the flux linkage measurement can not be used to estimate the average torque for a stroke, but this has to come from the static torque measurement.

The leakage inductance (L_{leak}) is estimated to be between 20 mH to 33 mH.

A key parameter to consider for this motor is output torque. The output torque is evaluated with a lower phase current than in the FEA-simulations to leave headroom for variations in the permanent magnets and still avoid demagnetization. The measured cogging torque, that is with no phase current,and the measured torque where the current is kept constant at $3.5\,\mathrm{A}$ can be seen in Fig. 4.21.

The torque measurement on Fig. 4.21 shows good agreement with the predicted torque, though it seems to be slightly lower than predicted. The torque production is affected by the flux from the permanent magnets, end effects, and the six magnets may have different levels of magnetization, potentially causing differences between FEA and measurement.

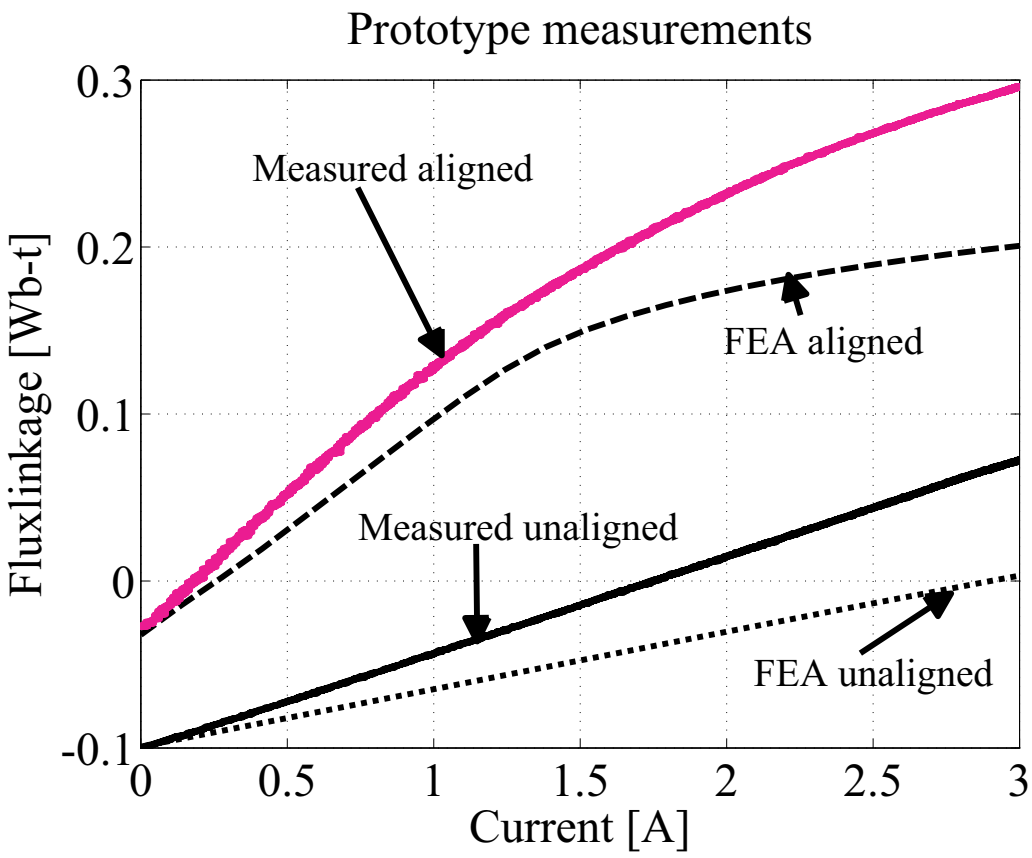

Figure 4.20: Measured flux linkage up to 3A for the prototype motor. The current was limited by AC-source.

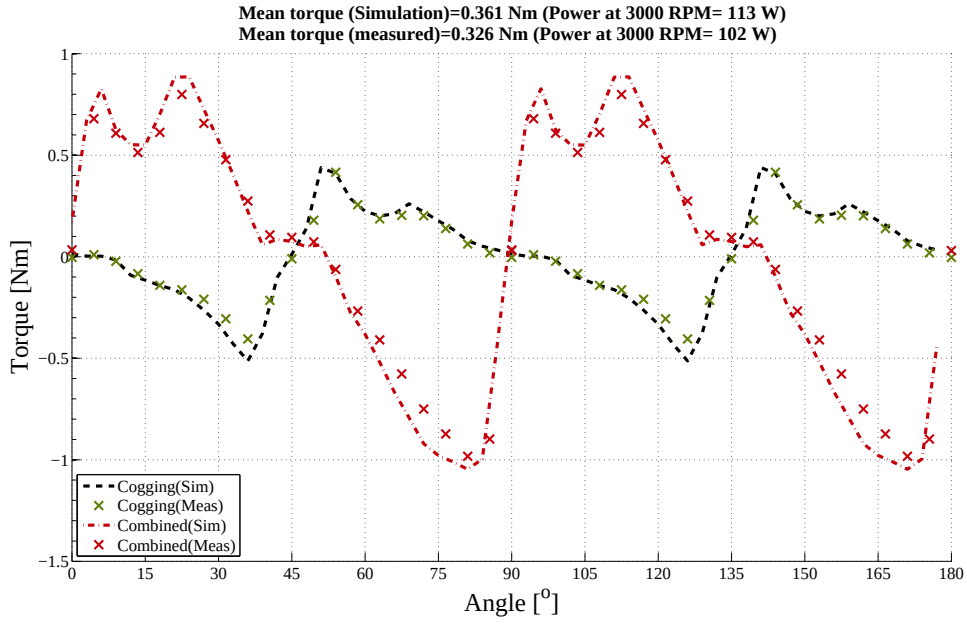

Figure 4.21: The figure shows the measured static torque and the FEA predicted static torque.

4.6 Discussion

The motor design presented in this chapter is easy to assemble and disassemble. The prototype was assembled from the pre-made components: the two coils, stator, magnets, glue, shaft with concrete and iron rotor and bearings. The rotor was not balanced. The coils were wound using a coil winding machine. For the prototype motor, the cogging torque and the total combined torque for various DC currents were measured. By detecting the rotor parking position and from the cogging torque measured, the static frictional torque may be estimated, which was found to be less than 0.05 Nm. Knowing the parking position and the measured combined torque, the starting torque may be estimated, which is larger than 0.2 Nm for a starting current of 3.5 A. This starting torque will not only be able to overcome the frictional torque in various conditions, but also will accelerate the motor to a desired minimum speed (e.g. 300 RPM) in a short time, where a simple, back-EMF based sensorless controller may successfully take over the control. For the prototype machine, with the high starting torque provided, it is able to accelerate to 350 RPM within only one stroke.

A comparison of the HSRM with the 3 phase benchmark motor at 100 W presented in [40], can be seen in table 4.1. The single phase HSRM uses less active materials than the benchmark motor, including permanent magnet material despite the fact that the HSRM uses ferrite magnets and the benchmark motor uses NdFeB magnets.

The design could still be optimized in several ways:

1. More copper, would reduce the resistive losses, but adding copper would also increase the cost of the motor. So an optimisation could be done in this regard. Here the number of turns are chosen, so the coils can be square and the rotor can still be inserted afterwards.

2. If motor volume is increased, the losses also drops. Once again the cost would increase.

3. The cogging torque is rather low compared to the combined torque. If the combined torque is at full magnitude the combined torque would be significantly higher than the cogging torque giving a larger torque ripple.

Table 4.1: Machine Comparison

Parameter	First prototype HSRM	MLBLDCM/4[40]
Output power (Theoretical)	100 W	100 W
Outer stator length	96.4 mm	113 mm
Airgap	0.4 mm	0.65 mm
Rotor radius	24.2 mm	30.85 mm
Shaft diameter	10 mm	18 mm
Stack length	30 mm	30 mm
Silicon iron weight	1.153 kg	1.760 kg
Permanent magnet weight	95 g	112 g
Permanent magnet Type	Ferrite C5	Bonded NdFeB
Copper weight	185 g	319 g

4. The torque profile for the combined torque has some predominant peaks not found in the design presented in [36]. The saturated piece of iron near the rotor slots does not achieve hard saturation and can not emulate the behaviour of the stepped air gap presented in [71].

The dynamic behaviour of the first prototype is treated in the part regarding motor control.

4.7 Conclusion for first prototype

A single phase hybrid switched reluctance motor was designed with a novel stator pole shaping method and a new arrangement of permanent magnets for flux concentration was presented. It was shown how stator pole shaping can improve starting torque for a single phase hybrid switched reluctance motor. It was demonstrated that the configuration of permanent magnets in different flux concentration arrangements influences the shape and magnitude of the torque. This first prototype is used for most of the experiments presented in the next part, with the exception of the tests in a pump system.

A list of parameters for the first prototype is shown in appendix A.

Chapter 5

Pump motor implementation

This chapter describes a few key points regarding a hybrid switched reluctance motor (HSRM) for a small pump motor drive. The second prototype should fit inside a standard pump housing. The main purpose is to test the sensorless control in a small pump system. The main purpose is to investigate the the sensorless control of a HSRM in a pump motor drive and to propose an alternative to the stainless steel can used to protect the windings in normal wet-runner pump drives.

The chapters starts by an overview of the specifications for this motor design, followed by an initial estimate of the size of the motor. The proposed motor parts are presented and a proposed low cost replacement of the winding protection is presented. A summary ends the chapter with some comments and conclusions.

5.1 Specifications for pump motor prototype

The first prototype showed that an extension of the positive torque region was possible and copper consumption could be low with simple coils.

The goal is to design a prototype single phase hybrid switched reluctance motor with following specifications:

- The peak output power is 30 W at 3000 RPM.
- The motor should have starting torque of approximately the same as the average torque $\tau = 0.1\,\mathrm{N\,m}$.
- The motor should fit a standard pump housing for an induction motor pump. The diameter is 80 mm and the stacklength is 25 mm.
- The permanent magnets have a fixed size of $6 \times 13 \times \times 32$ mm .
- Unlike [5, 68] only one type rotor lamination should be used to simplify construction.

5.2 Design of pump motor prototype

The angles of the rotor poles and stator poles are kept the same as for the first prototype, so the description of these are given in the previous chapter. See Appendix B for flux plots of the motor at parked and aligned position at both full current and no current.

5.2.1 Initial sizing

The motor is supposed to fit a standard pump housing for an induction motor pump. The diameter is 80 mm and the stacklength is 25 mm.

The output power has to be approximately 30 W at 3000 RPM. This gives an output torque of approximately $0.1\,\mathrm{N\,m}$. For this design a brushless DC-motor with ferrite magnets has an output torque of $0.16\,\mathrm{N\,m}$ at 3000 RPM, with a rotor diameter (D_{rotor}) of 46 mm and a permanent magnet volume of $11.4\,\mu\mathrm{m}^3$. For this motor with C8 magnets, a magnet volume of approximately $0.2\,\mu\mathrm{m}^3$, and a 5 cm diameter rotor the torque is approximately given in (5.1). The difference between the strength of C5 and C8 magnets is ignored here in the initial sizing.

$$K_{motor} \cdot V_{magnet} \cdot D_{rotor}^{1/4} = \tau = 0.135\,\mathrm{N\,m} \tag{5.1}$$

Where K_{motor} was found in 4.3.1.

This means that the output power at 3000*RPM* for this motor is approximately $\tau \cdot \omega = 42.5\,\mathrm{W}$.

5.2.2 Proposed motor for second prototype

The proposed second prototype HSRM is shown in Fig. 5.1. The motor differs structurally slightly from the first prototype in the sense that it uses fewer magnets, has a simpler rotor structure and the motor fits into a standard pump motor housing.

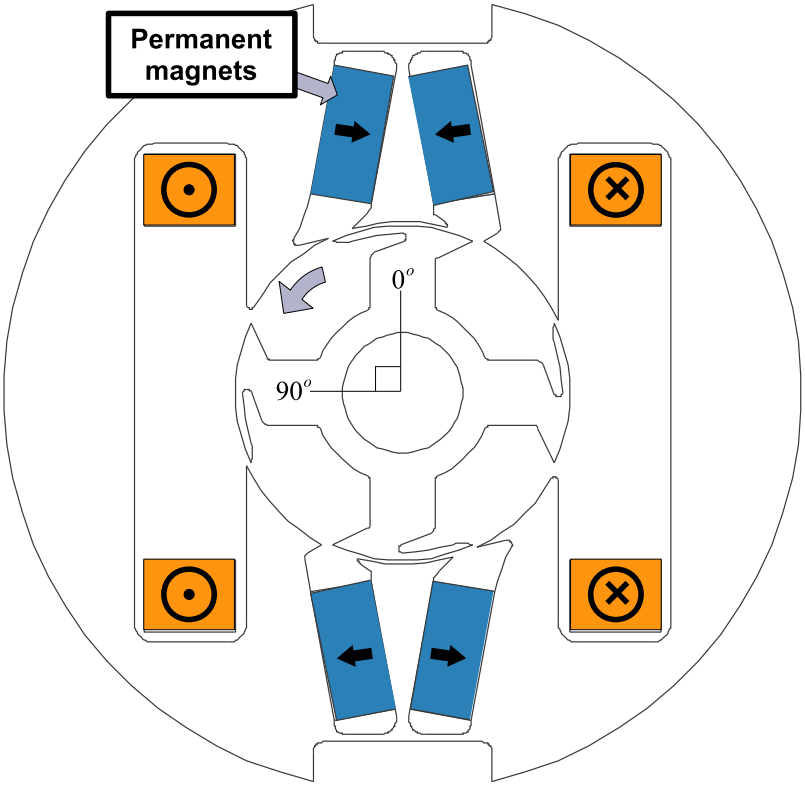

Figure 5.1: The second prototype with a simplified design compared with the first prototype.

5.2.3 Flux concentration with fewer ferrite magnets

The first prototype used 6 magnets to achieve a flux density of up to $0.8\,\mathrm{T}$ in the airgap from the permanent magnets alone. The magnets for the second prototype is of a standard size and are not specifically made for this motor, unlike the first prototype. The second prototype uses 4 magnets with fixed dimensions: $13 \times 6 \times 32\,\mathrm{mm}$. This time the magnet grade was changed from

C5 to C8 mainly due to availability. The peak flux density is reduced to $0.63\,\mathrm{T}$, as can also be observed in the cogging torque as it can be seen in Fig. 5.2.

5.2.4 Simplified rotor design

The previous rotor used a design that was not suitable for punched laminations. A simplified design was designed with a reluctance path approximately as the first prototype. The minimum thickness of sections of laminations cannot be smaller than $0.8\,\mathrm{mm}$ due to manufacturing limits. Like the previous design, this sets some limits on the shape of the torque envelope. A smooth airgap is still needed, and thus a stepped airgap can not be used to achieve a flat top torque. [22]

The torque envelope can be seen in Fig. 5.2. The overlap between the cogging torque and combined torque is improved compared to the first prototype. The torque generated by the permanent magnets is reduced, but the permanent magnet volume is also less than half of the first prototype.

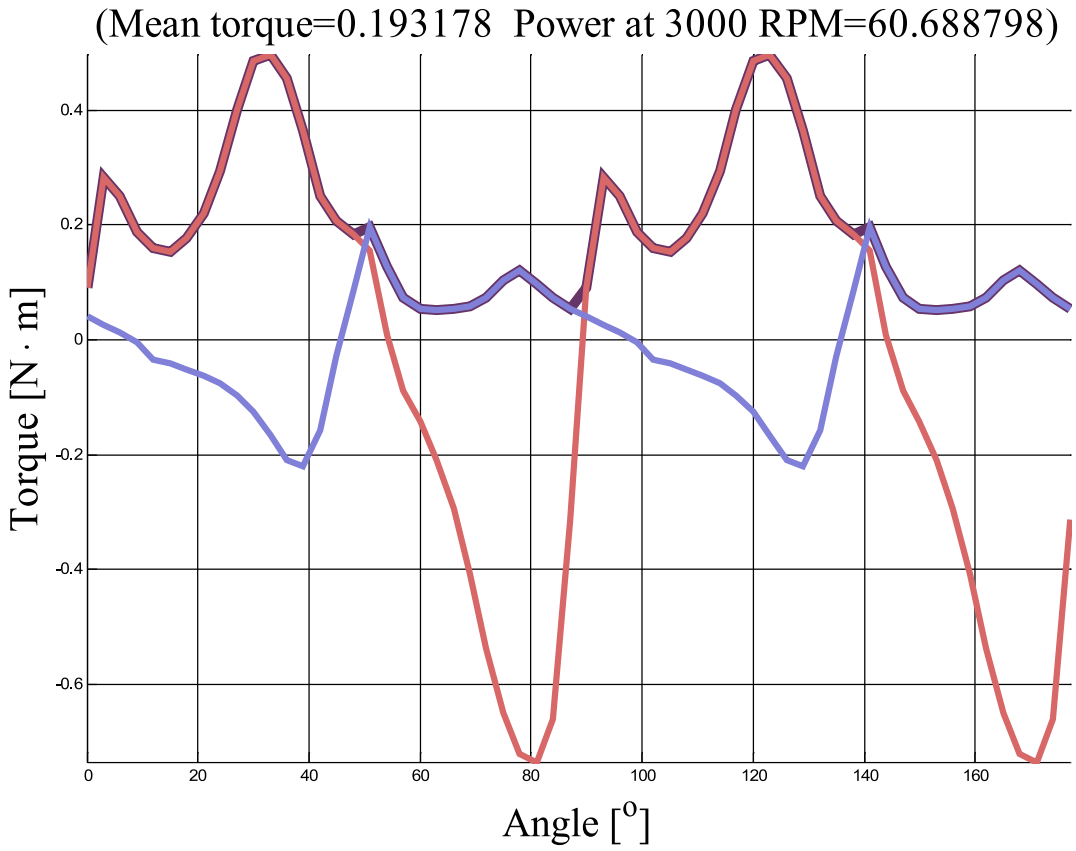

Figure 5.2: The torque envelope for the second prototype. The output torque is less than half of the first prototype, but so is the rotor volume.

5.2.5 Rubber protection of motor windings against water

The wet runner typically uses a stainless steel can inserted in the airgap to protect the phase windings. In this prototype, the windings are to be protected in another way to try to reduce the cost. If the stainless steel can is removed, the stator and the windings are exposed to the hot water. In the following discussion, unless stated otherwise, water is considered to be just pure liquid water with no impurities except limited amounts of dissolved oxygen (O_2).

Water is a polar molecule, which makes it a good solvent. Heat will speed up some chemical processes, including some which involves water. Hot water may degrade conventional winding insulation like polyester through hydrolysis[76] and shorten the service life of the coil[77]. Since hot water also has a higher conductivity than cold water[78], it is clearly important to protect

the phase windings. Partial discharges are a symptom of insulation breakdown, and to retard corrosion of the phase winding, a coating may be applied on top of the polyester coated windings. Since the windings in this motor are concentrated windings, which has a simple coils shape, rubber coating may be applied as an outer armour. The proposed rubber armour is shown in Fig. 5.3.

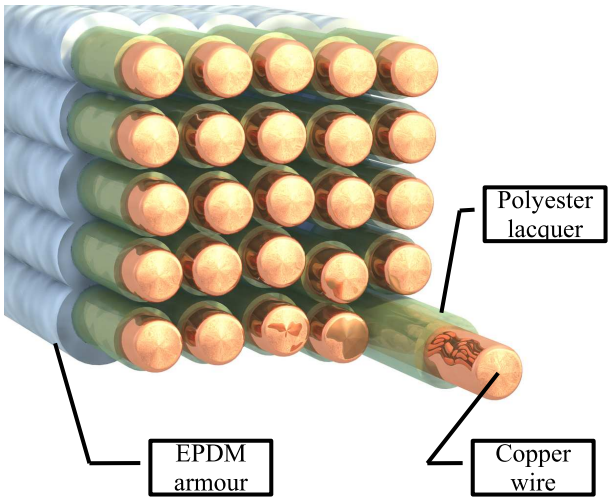

Figure 5.3: A coil can be coated with a layer of EPDM on the surface of the coil

At least two materials are interesting to consider for the rubber armour: silicone rubber and Ethylene Propylene Diene Monomer (EPDM). They can be mixed and it is thus possible to mix the properties of the two materials. Silicone rubber has a higher resistivity than EPDM, but EPDM has a higher tensile strength[79]. Both materials are suitable candidates for this project, but EPDM is available in an uncured form that allows for simple coating of the windings.

The following description is by no means exhaustive, since completely describing the EPDM polymer is outside the scope of this thesis.

EPDM is an artificial rubber introduced in 1950's[80] and thus has had a significant service life. It has good resistance against how water, ozone (which is chemically more reactive than O_2).

EPDM is one of the most commonly used industrial rubbers due to its resistance to ageing due to heat, light, oxygen, and ozone[81]. Furthermore it has the potential to be used in blast/shock absorbing applications[81]. Most ageing studies focus on EPDM weathering in open air, considering elongation at break as the primary modus of failure, as seen in [82, 83, 84].

It is however noted that ageing is retarded if too much water is sprayed on the EPDM during tests[85]. This may be why [86] reports that EPDM endured long term exposure to 150^{o}C steam. The long term endurance in hot water conditions can also be observed by the fact that EPDM is already now used in pumps as seals and structural support for bearings[87]. The main weakness of EPDM is the poor resistance against solvents like toluene and aromatic hydrocarbons, but these compounds should normally not appear in domestic heating systems.

The EPDM chosen for this thesis is called a liquid EPDM, since it can be applied on surface in a liquid form. Before the EPDM is applied, a catalyst is added to the liquid EPDM, that over time will evaporate and leave a rubber coating on the painted coil surface. The coils are dipped in the mixed EPDM and left to dry for three weeks. The dried EPDM coat seems to be evenly distributed with an approximate thickness of $0.5\,\mathrm{mm}$. This means the dielectric strength is approximately $10\,\mathrm{kV}$, sufficient for the test here.

The stator coils are coated in the second prototype and the coated coils can be seen on Fig. 5.4.

Figure 5.4: The two rubber coated coils.

The EPDM coating have not been tested to see if the manufacturers specifications are valid. The EPDM rubber coated coils are however used in the second prototype, to evaluate the behaviour of the position sensorless control method presented in the next part.

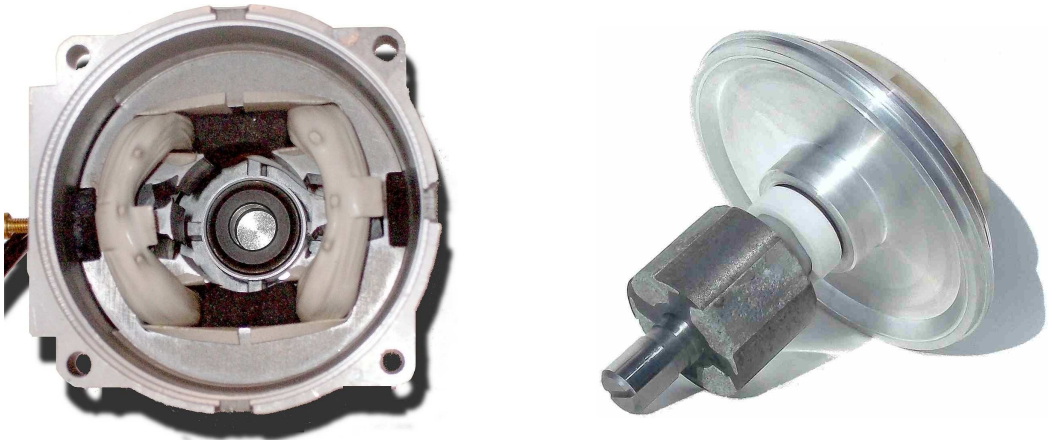

Figure 5.5: The stator and the rotor before assembly.

5.3 Implementation of second prototype

Implementation of the second prototype is primarily done to see if the HSRM can run position sensorless in a pump system. There was a small slip between the pump motor housing and the stator (approximately $0.05\,\mathrm{mm}$), and this means that the stator can move relative to the motor housing when subjected to the normal force from the rotor. The final rotor assembly with impeller and end piece fits into motor housing and pump housing.

5.4 Discussion

The main research question for this thesis is to evaluate the suitability of a hybrid switched reluctance motor as a variable speed pump motor. An initial test of the HSRM pump motor is presented in the chapter regarding position sensorless control.

The static parameters (static torque and flux linkage are not measured for this motor), since the prototype is manufactured and assembled as a pump motor and thus does not fit the test set-up described in appendix D.

5.5 Summary

This chapter presented some features of a hybrid switched reluctance motor, that was designed to fit in an existing pump motor housing, replacing a stainless steel can in the airgap with rubber protection of the windings. The test results from the position sensorless measurements in a small scale pump system, will be presented in the next part after introducing the control methods, including a position sensorless control method.

Part III - Motor Control

Chapter 6

Control methods for HSRM

This chapter describes how the single phase hybrid switched reluctance motor is controlled. First general cascaded control is discussed, followed by a description by the current control as the inner loop of a cascaded control loop. This is followed by a description of the outer loop of the cascaded control loop, a time variant non linear speed controller, with a short description of some effects of the time variance.

6.1 Design philosophy for control

Not many companies have realized commercial switched reluctance motor drives[23], but some have succeeded such as LG[88], Dyson[89] and Shop-Vac[90]. One of the main reasons may be the complexity of the controller that needs to be tailored to each design, each application, and possibly each unit[23]. The acceptance of PMBLDC motors in a variety of applications depends on the simple and low cost controller[91]. This also applies to the hybrid switched reluctance motor(HSRM) and this chapter tries to show that the control of a HSRM is rather simple.

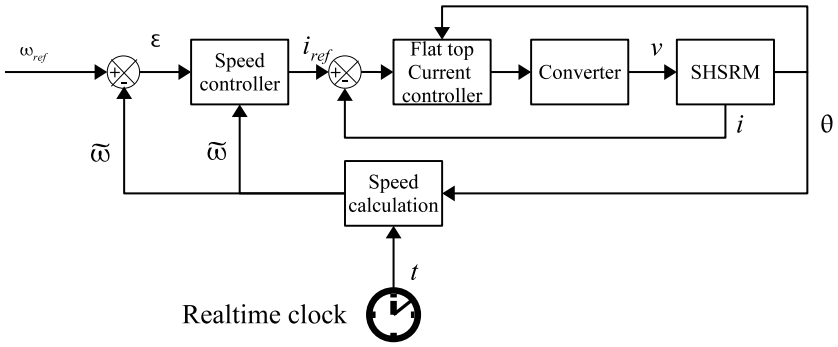

Figure 6.1: Cascaded control structure for HSRM.

6.2 Cascaded control

In a variable speed drive the target is to control the rotational speed of the drive, so it tracks a speed reference. To control speed, torque has to be controlled through controlling the phase current. The typical way to implement speed control is to control phase current and thus torque in an inner current control loop at an update frequency orders of magnitude faster than the outer speed control loop. The speed control generates a current reference to the inner current control loop and the inner current control loop is supposed to reach this current level before next update of the speed controller as it is seen in Fig. 6.1. The target of the current control is to achieve a well defined relationship between reference current and motor torque. That way the control is similar to the simple control as seen in DC- and BLDC-motors[23, 45].

6.2.1 HSRM torque control

The single phase hybrid switched reluctance motor (HSRM) is basically controlled like a normal switched reluctance motor using the single phase inverter. The inverter progresses through a number of discrete states as shown in Fig. 6.2.

I The current flows through the active transistors, energizing (fluxing) the phase

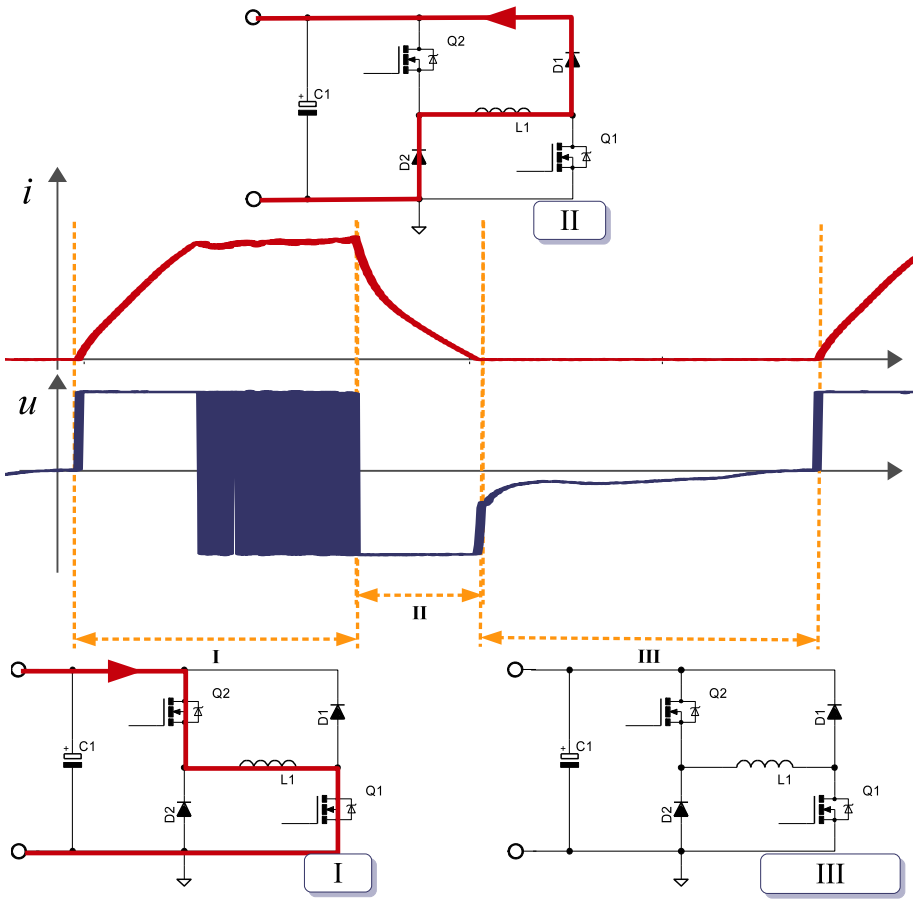

Figure 6.2: The single phase inverter for the HSRM has a fixed number of states possible. During approximately half the time, the converter is inactive.

II The current cannot flow through the inactive transistors but flows through the diodes. This defluxes the phase.

III No current is in the phase and the converter is inactive.

Torque in a switched reluctance motor is produced by pulses of phase current synchronized with the rotor position[23]. A pulse of the phase current is sometimes also called a stroke. Torque is controlled by controlling the current shape and timing of these phase current pulses. At low speed the torque can be controlled by chopping[23], at higher speeds torque is controlled by changing the timing for when to turn on and turn off phase current[23]. Ideally the torque would be controlled with a simple linear relationship between torque and current. This may not always be the case for the switched reluctance motor, where the torque may also be influenced by rotor

speed, and a non-linear relationship exist between torque and current.

The HSRM is parked at a specific rotor angle, and the coils are energized to start the rotation in one direction. The phase coil is energized by letting the transistors conduct the current. The current is maintained at a desired current level until the current is turned off (defluxing) at a specific angle and the moment of inertia and the cogging torque ensures the continued rotation in the desired positive direction. The defluxing is achieved by turning the transistors off and letting the diodes conduct until the phase current is zero. These requirements lead to the torque control state machine shown in Fig. 6.3.

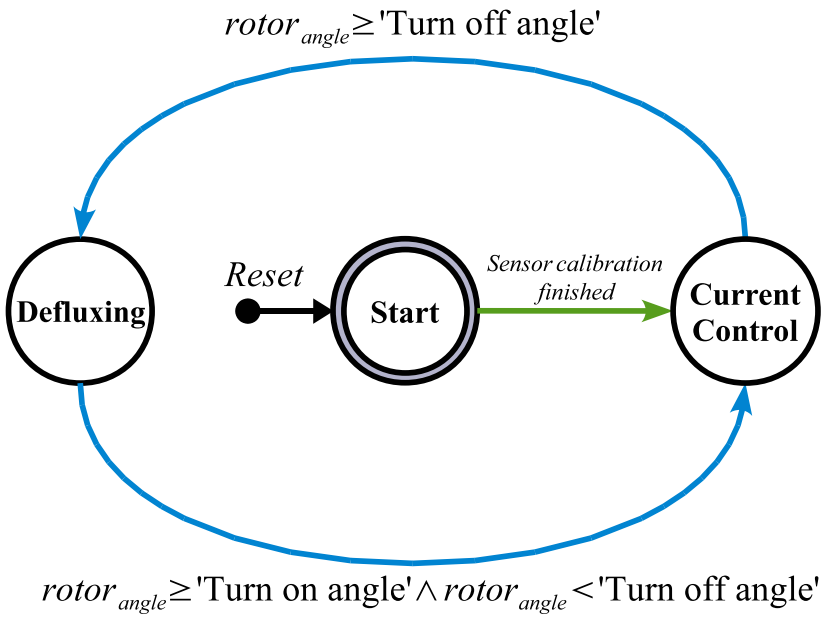

Figure 6.3: The torque control state machine is shown above. Circles indicate the state of the state machine, dark arrows indicate state transition with conditions, and light blue arrows indicate that the state is kept until the state transition condition is fulfilled.The torque control is active only for approximately half the time, four times per rotation. The turn on angle is approximately 0^o *, and the turn off angle is approximately* 42^o

The inverter has at least two states: defluxing and energizing. To simplify the description, the notation in [51] is used, which describe the voltage ($\tilde{u}$) as a number between -1 and $+1$, for fully defluxing and fully energizing respectively. If PWM is used with the single phase inverter, then the PWM duty cycle ($D_{duty} \in [0, 1]$) approximates an average voltage magnitude. This means an

average model for the applied voltage may be given as:

$$2 \cdot \left(D_{duty} - \frac{1}{2} \right) \cdot U_{DC-link} = \tilde{u} \cdot U_{DC-link} \tag{6.1}$$

The two HSRM in this project has similar torque envelopes that was presented previously. To achieve better efficiency it is important to achieve maximum torque per ampere phase current spent. One of the desired design specifications was to achieve an acceptable starting torque. In a previous chapter 4.5 it was also presented that an elongation of the positive torque region, would mean that the peak negative torque would also increase. This increase also means that the change of torque magnitude is rather high at the point where current has to be turned on. It is therefore desirable to change the current magnitude, rather fast at the turn on point. The turn off point is not so sensitive. The phase inductance sets a limit on how fast the current can be changed, and thus sets a limit o. To control the magnitude with a high precision regarding angles, a suitable current control update frequency is needed. If the the update frequency f_s for the torque controller is $50\,\mathrm{kHz}$, and the rotational speed (ω) is $314\,\mathrm{rad\,s^{-1}}$ then the resolution in degrees can be calculated as (6.2).

$$\frac{d\theta}{dt} = \omega \Leftrightarrow \frac{\Delta\theta}{\Delta t} \approx \omega \Leftrightarrow \Delta\theta \cdot f_s \approx \omega \Leftrightarrow \Delta\theta \approx \frac{\omega}{f_s} = \frac{314}{50000} \cdot \frac{180}{\pi} \approx 0.36^o \tag{6.2}$$

To limit the number of parts in the final system, it may be desirable to have a digital controller with a fixed update frequency for both angle and current control. The equation (6.2) showed that a switching frequency of $50\,\mathrm{kHz}$ is enough to achieve angle control with an accuracy of better than 0.5 degrees at 3000 RPM. A hysteresis controller could be used, but it may give excessive current ripple unless the control updates are sufficiently fast. A slow hysteresis controller is not acceptable in a permanent magnet motor, since current spikes limits how close to the demagnetization point the current reference can be. The slow hysteresis controller may also generate undesirable vibrations on the stator, possibly in the audible range. A hysteresis controller operating at a high average switching frequency would lead to increased losses in the inverter, and would be difficult to implement in a low cost digital controller. To avoid these problems, a modified proportional controller is used to control the system. The proportional controller has

a hysteresis band like a hysteresis controller, but within the hysteresis band the controller acts as a proportional controller. The gain is designed such that the output at the boundary between hysteresis mode and proportional control is the same. The hysteresis band is thus the only parameter that needs to be determined. The current change is, as said before, limited by the phase inductance. And the worst case is the minimum inductance at maximum voltage. The boundary can be determined by (6.3).

$$u = L \cdot \frac{di}{dt} \approx L \cdot \frac{\Delta i}{\Delta t} \Leftrightarrow \frac{u}{f_s \cdot L} \approx \Delta i \tag{6.3}$$

where u is the voltage applied to the inductance, i is the instantaneous phase current, f_s is the control update frequency, Δt is the time between two control updates, L is the minimum phase inductance, and Δi is the current difference between two current control updates.

Ideally, the update frequency of $50\,\mathrm{kHz}$, would mean a current ripple of $72\,\mathrm{mA}$. However the delay of the current measurement second order filter and the slight delay between current measurement acquisition and PWM output this in this implementation increased to approximately four times this number, i.e. $\Delta i = 144\,\mathrm{mA}$.

The proportional gain should at the boundary between operation as a hysteresis controller and as a proportional controller give the same result. So if the difference between current reference (i_{ref}) and measured phase current (i) is $\Delta i/2$ the output is given as (6.4):

$$k_p \cdot (i_{ref} - i) = k_p \cdot (\Delta i) = 1 \Leftrightarrow k_p = \frac{1}{\Delta i} \tag{6.4}$$

If Δi is chosen too small, the controller will frequently act mostly as a hysteresis controller. On the other hand, if Δi is chosen too large, the steady state error will be too large.

$$\tilde{u} = \begin{cases} +1 & i \leq (i_{ref} - \Delta i) \\ -1 & i \geq (i_{ref} + \Delta i) \\ k_p \cdot (i_{ref} - i) & otherwise \end{cases} \tag{6.5}$$

The measured and simulated phase current are compared on Fig. 6.4 and Fig. 6.5 for two different turn off angles. The simulations shows acceptable agreement with the measured results,

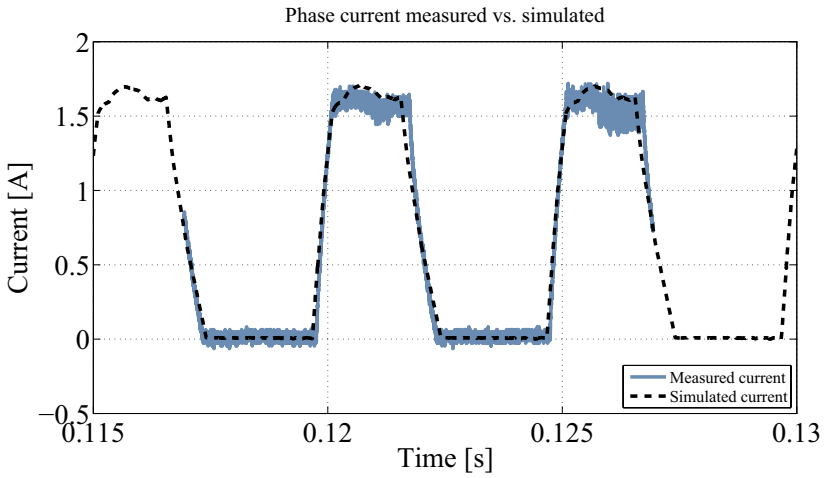

Figure 6.4: Measured phase current compared with simulated current from a dynamical non-linear model of the drive. The simulated control only uses a current control with the same turn on and turn off angles.

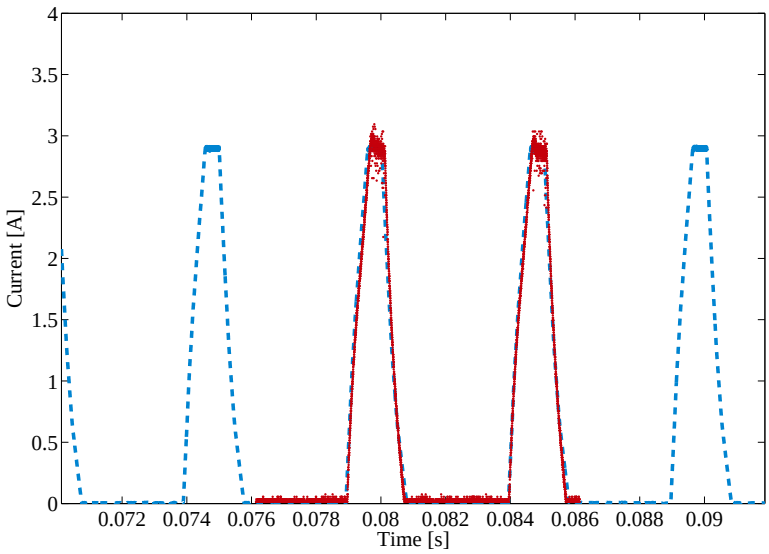

Figure 6.5: Measured phase current compared with simulated current from a dynamical non-linear model of the drive. The simulated control only uses a current control with the same turn on and turn off angles. The turn off angle is now $14\ ^{o}$ *rather than the usual* $43\ ^{o}$.

but notice that the inverter is simulated with an average voltage, rather than a simulation of the inverter PWM. The average model of the inverter speeds up simulation, but also does not model the current ripple caused by PWM switching.

A design criteria for the motor was to be able to use current control and not angle control also at 4000 RPM. At 4000 RPM the current rises relatively slowly as compared to low speed, but a flat

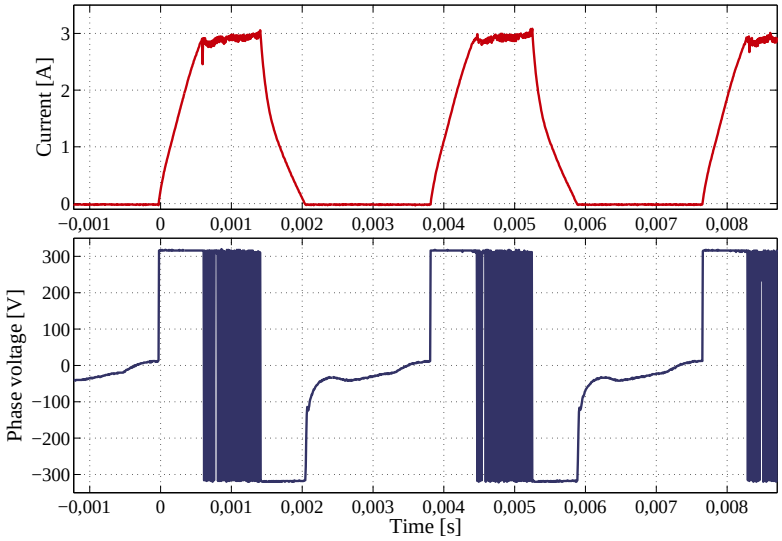

Figure 6.6: The motor phase voltages and currents at 4000 *RPM.*

top current is maintained as shown in Fig. 6.6.

The current control method is sufficient to control the current with a relatively small overshoot. This is the current control method also used for the position sensorless control presented in the next chapter. The speed controller, presented in the following, uses the current controller presented in this section as the inner torque control loop

6.3 Speed control for single phase HSRM

The outer loop of the cascaded loop is the speed controller as it is shwon in Fig. 6.7. The speed controller would normally be updated at a fixed update frequency. The basic reason for the proposed controller here, is that the information about the true average speed is available four times per revolution and the average torque can be properly controlled four times per revolution. In other words the speed controller updates should be synchronized with the rotor speed rather than have a fixed update frequency.

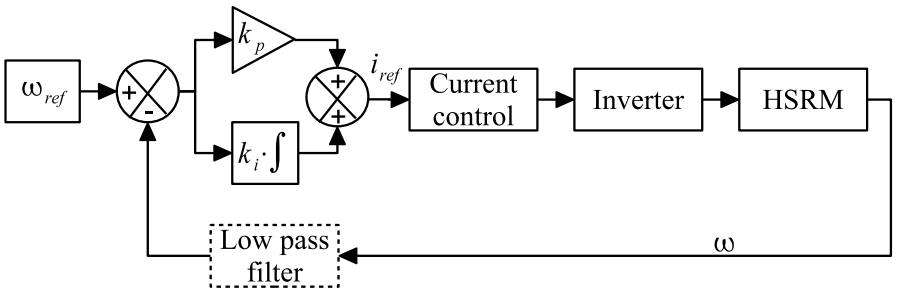

Figure 6.7: The speed controller is implemented as two parallel controllers that sums up to give a current reference for the current controller.

The idea of this section is to show that a time variant modification of the discrete integration in a proportional-integral controller, that approximates the continuous integration, performs as good as or better than a time invariant proportional-integral controller. The real advantage is however in simpler implementation of the time-variant controller than the time-invariant controller. An added benefit is also that some of the calculations used for the time variant controller may be reused in the position sensorless control method presented in the next chapter. First an introduction is given to the design of a time invariant speed controller for a hybrid switched reluctance motor followed a design of a time variant speed controller and this is concluded by a comparison.

6.3.1 Time invariant controller

If the system that is controlled mostly is a first order system, then it is sufficiently controlled by a proportional and integral controller[92]. The model of the controlled system was described in

chapter 3 and only the equation regarding the speed is considered in this section. The differential equation describing the speed from chapter 3 is repeated in (6.6).

$$\frac{d\omega}{dt} = \frac{\tau_m(\theta, i) - B \cdot \omega - \tau_l}{J} \tag{6.6}$$

where ω is the rotational speed, $\tau_m(\theta, i)$ is the torque produced by the motor that is dependent on the rotor angle (θ) and instantaneous phase current (i), B is the rolling friction, J is the combined moment of inertia of the load and rotor, and τ_l is the torque load. If the load is considered a disturbance and initially ignored, then the speed may be described by the simple equation (6.7).

$$\frac{d\omega}{dt} = \frac{\tau_m(\theta, i) - B \cdot \omega}{J} \tag{6.7}$$

The average torque for a single phase HSRM has a non-linear dependency on both speed and current. The average torque for the first prototype using a dynamic simulation, where the current reference is kept fixed at a desired value and the speed of the rotor is forced to a given speed is shown in 6.1. To simplify the discussion, the relationship between torque and current is treated

Table 6.1: Average torque vs. speed and current

$\tau_{avg}(i,n)$/Nm	n=1000 RPM	n=2000 RPM	n=3000 RPM	n=4000 RPM
$i = 1$ A	0.065	0.062	0.058	0.053
$i = 2$ A	0.168	0.156	0.143	0.129
$i = 3$ A	0.278	0.254	0.230	0.203
$i = 4$ A	0.333	0.301	0.269	0.234

as linear and speed independent. This is done by choosing a fixed speed of 3000 RPM and using linear regression to find an approximation in (6.8)

$$\tau(i) \approx 0.072 \cdot i - 0.005 \tag{6.8}$$

To avoid the offset in (6.8), the gain is scaled back in (6.9)

$$\tau(i) \approx 0.071 \cdot i \tag{6.9}$$

Active torque control is also not possible for the entire stroke, as described in the section above. The update frequency of the discrete digital implementation has to be similar to the frequency of

the strokes. Since the number of strokes varies with the speed, the update frequency of the speed controller has to be either at the highest frequency of the strokes at high speed, at the lowest frequency of the strokes at low speed or somewhere in between. Since the torque produced has a periodic ripple, with a period of four times the rotational frequency, this speed ripple may affect the input to the speed controller if it is not low pass filtered. If the speed controller updates are not synchronized with the strokes, the speed controller outputs may change during a stroke. The changes in the speed controller output during a stroke, may give rise to undesired low frequency oscillations in the measured rotor speed. So the controller design is a compromise between four parameters: Update frequency, low pass filter parameters, proportional gain and integral gain.

For the time invariant controller described here the control updates are chosen to occur at a frequency of 200 Hz to give a good response at 3000 RPM. It also means that there will three updates of the speed loop during one stroke at a speed of 1000 RPM. To avoid the speed controller to respond to the torque ripple at e.g. 1000 RPM, the speed measurement is lowpass filtered before it is used in the feedback. The lowpass filter is chosen to have a cut off frequency of 400 , since this is the lowest useful speed.

The time invariant controller is simulated and the response is satisfactory as seen on Fig. 6.8, for a variable speed drive pump. Notice the time it takes for the controller at high speed to remove the steady state error. The moment of inertia of the rotor and the fan is set to 500 mg·m^2.

If the moment of inertia is reduced to 50 mg·m^2 and the controller gains are maintained the rotor speed may oscillate as seen in Fig. 6.9. The speed is oscillating because the low pass filter does not completely filter out the speed ripples before they are used by the speed controller.

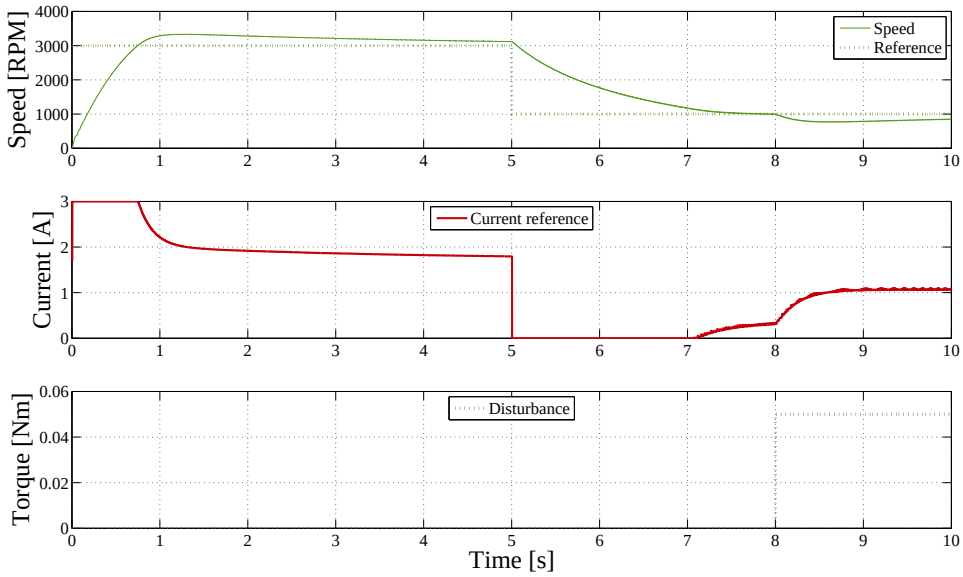

Figure 6.8: Simulated time invariant controller with low pass filter on the speed measurement. The controller toggles between a speed references of 3000 *RPM and* 1000 *RPM, and a load disturbance is introduced at* $t = 8$ *s.*

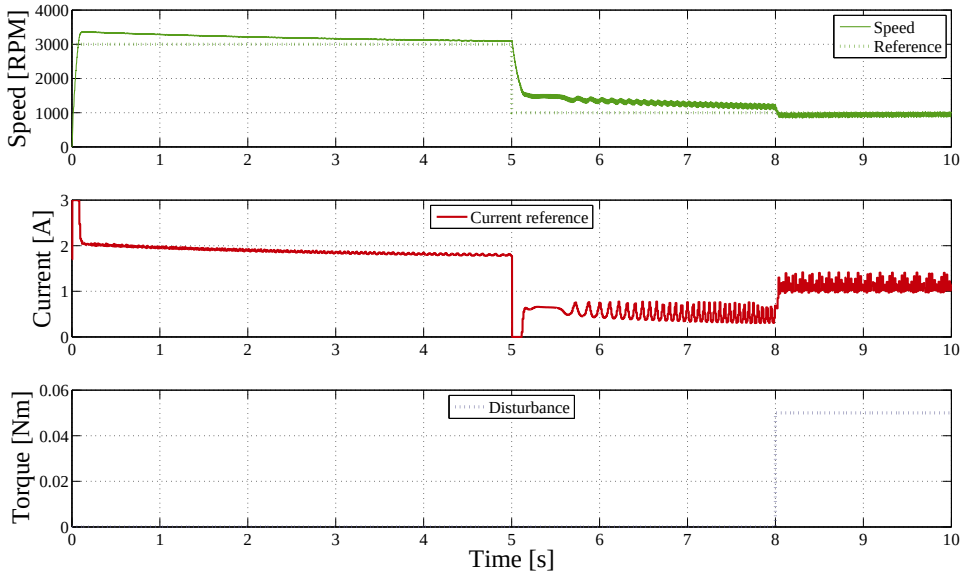

Figure 6.9: Simulated time invariant controller with low pass filter on the speed measurement. The moment of inertia is reduced to 50 $mg{\cdot}m^2$.

6.3.2 Accurate average speed calculation for a high torque ripple motor

If a motor has non uniform torque during a rotation, the speed variation will be related to the torque variations. This section describes a simple way to calculate the average rotation speed,

with no low pass filter.

For the discussion here, the load is assumed zero and the only losses are caused by the rolling friction by the bearings.

As presented in chapter 3, the rotational speed ω is governed by (6.10).

$$\frac{d\omega}{dt} = \frac{\tau_m(\theta, i) - B \cdot \omega - \tau_l}{J} \tag{6.10}$$

where $\tau_m(\theta, i)$ is the angle (θ) and phase current (i) dependent torque, B is the viscous friction coefficient, τ_l is the load torque, and J is the combined moment of inertia of both the rotor and the load.

If a linear relationship between current and torque as given in (6.9) is assumed then (6.10) can be Laplace transformed. Setting the torque load to zero and Laplace transforming (6.10), simplifies the speed calculation to (6.11)

$$s\omega = \frac{\tau_m(\theta, i) - B \cdot \omega}{J} \Longleftrightarrow \omega = \frac{\tau_m(\theta, i)}{B + s \cdot J} \tag{6.11}$$

The torque production is angle and phase current dependent and the torque production is not very smooth. It is however periodic, because the torque envelope repeats itself four times per revolution or once per stroke. A stroke is one cycle of the current control state machine, as it was described in the previous section, and as it is shown on Fig. 6.10.

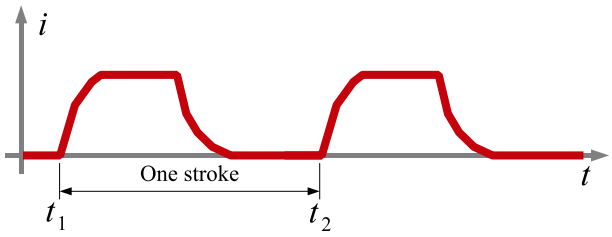

Figure 6.10: One stroke or current control cycle starts with energizing the phase winding at time t_1. The stroke ends at time t_2, just before energizing the winding the next time.

Seen from the speed controllers point of view the dynamics caused by the time variant speed updates can be seen as a variable delay, since the speed control updates are synchronized with the rotor. Where the delay ($t_d \approx \frac{\pi}{2 \cdot \omega}$) is inversely dependent on the speed. Adding this delay to

equation (6.11) would give equation (6.12)

$$\omega = \mathbf{e}^{(-\frac{\pi}{2\cdot\omega}s)}\frac{\tau_m(\omega,i)}{B+s\cdot J} \tag{6.12}$$

Synchronized updates allow the decoupling of the electrical from the mechanical subsystem when designing the speed controller. Speed measurements may also use these synchronized updates to simplify speed calculation.

Using the notation in [93], a sequence of average speed measurements $\tilde{\omega}[k]$ with a continuously increasing index k can be calculated accurately four times per revolution. Assume that the speed controller updates are sequentially numbered (k), and thus the present update is done at the time $t[k]=t_2$, and the previous update was done at the time $t[k-1]=t_1$. It is important to notice that the time between $t[k-1]$ and $t[k]$ varies as a function of the speed. The measured average speed can be calculated as:

$$\tilde{\omega}[k] = \underbrace{\frac{1}{t[k]-t[k-1]}}_{\text{Averaging term}} \cdot \underbrace{\int_{t[k-1]}^{t[k]} (\omega(t))\,dt}_{\text{Distance}} \tag{6.13}$$

where $\omega(t)$ is the continuous rotor speed at time t, and distance is the distance the rotor has travelled in the time interval ($t[k]$ to $t[k-1]$). If the control is kept synchronized with the rotor, the speed can be calculated by substituting the integral in (6.13) with a fixed value of $\pi/2$ radians:

$$\tilde{\omega}[k] = \underbrace{\frac{1}{t[k]-t[k-1]}}_{\text{Averaging term}} \cdot \frac{\pi}{2} \tag{6.14}$$

Using (6.14) the average speed for the period $t[k-1]$ to $t[k]$, can be calculated accurately four times per revolution. It alse means that the time between two strokes can be calculated as seen in (6.15).

$$\Delta t = t[k]-t[k-1] = \frac{\pi}{2\cdot\tilde{\omega}} \tag{6.15}$$

Unfortunately it also means that for the decoupling and speed measurement methods to be useful, the speed control loop needs to be updated synchronized with rotor, that is with a variable time between control updates. The main problem considered in the next two sections is how to

emulate the continuous integration in with a time variant discrete approximation in two simple ways.

6.3.3 Time variant integration

A simple controller can be made with a proportional controller, but it will have a steady state error [94]. Adding an integral term would remove the steady state error, but normal approximations of the continuous time integrator assume a fixed update frequency. The system dynamics changes when the integrator becomes time variant as the following will describe.

Using the discrete time frame as presented for the speed calculation in equation (6.13), the error ($\varepsilon[k]$), at the time instance (k), between the speed reference (ω_{ref}) and the measured speed is given by:

$$\varepsilon[k] = \omega_{ref}[k] - \tilde{\omega}[k] \tag{6.16}$$

Classical calculus tell that the continuous integration of a given function ($y = \int(f(x))dx$) can be approximated by piecewise summations of numerical integration methods[95]. One such numerical integration method is the trapezoidal approximation[95]. The time between updates are then not infinitely accurate, but has a finite resolution depending on the implementation. The speed controller may in a real implementation be implemented with a time domain resolution limited by the current controller update frequency. This means that the distance between updates can be calculated as given in (6.17).

$$\Delta t = \frac{\pi \cdot f_s}{2 \cdot \tilde{\omega}} \frac{1}{f_s} = \frac{counter_t}{f_s} \tag{6.17}$$

where $counter_t$ is a counter increased by 1 every update of the current controller and reset once per stroke, e.g. every time at the turn on point.

A trapezoidal iterative numerical integration may then be calculated as (6.18):

$$\begin{aligned} int[k] &= int[k-1] + \frac{\Delta t}{2}(\varepsilon[k-1] + \varepsilon[k]) \\ &\approx int[k-1] + \frac{counter_t}{2 \cdot f_s}(\varepsilon[k-1] + \varepsilon[k]) \end{aligned} \tag{6.18}$$

If the continuous integrator is given a fixed gain (k_i), then approximation (6.18) can be modified into (6.19).

$$int[k] = int[k-1] + k_i \cdot \frac{counter_t}{2 \cdot f_s}(\varepsilon[k-1] + \varepsilon[k]) \tag{6.19}$$

where $int[k]$ is the integrator at time instance k. The proportional controller is calculated as (6.20):

$$prop[k] = k_p \cdot \varepsilon[k] = k_p \cdot (\omega_{ref}[k] - \tilde{\omega}[k]) = k_p \cdot \left(\omega_{ref}[k] - \frac{1}{t[k]-t[k-1]}\frac{\pi}{2}\right) \tag{6.20}$$

where $prop[k]$ is the output of the proportional controller and k_p is the gain of the proportional controller. The combined controller response is then given by equation (6.21)

$$i_{ref}[k] = \begin{cases} k_p \cdot \varepsilon[k] + int[k] & \text{if } (k_p \cdot \varepsilon[k] + int[k]) \geq 0 \\ 0 & \text{if } (k_p \cdot \varepsilon[k] + int[k]) < 0 \end{cases} \tag{6.21}$$

The description here does not include the saturation and anti-windup handling, but the controller output has saturation boundaries as does the integrator.

The time variant controller is simulated and the response is satisfactory as seen on Fig. 6.11, for a variable speed drive pump. The controller removes the steady state error faster than the time invariant controller.

If the moment of inertia is reduced to 50 mg·m^2 and the controller gains are maintained, the rotor does not show the oscillations previouly shown in Fig. 6.9, but shows the stable behaviour seen in Fig. 6.12.

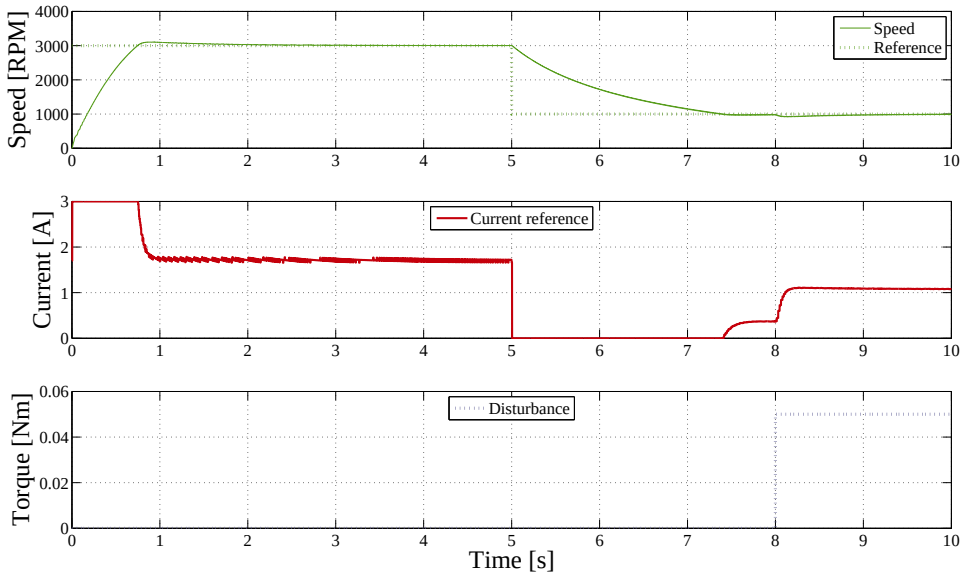

Figure 6.11: Simulated time variant controller. The controller toggles between a speed references of 3000 *RPM and* 1000 *RPM, and a load disturbance is introduced at* $t = 8$ *s.*

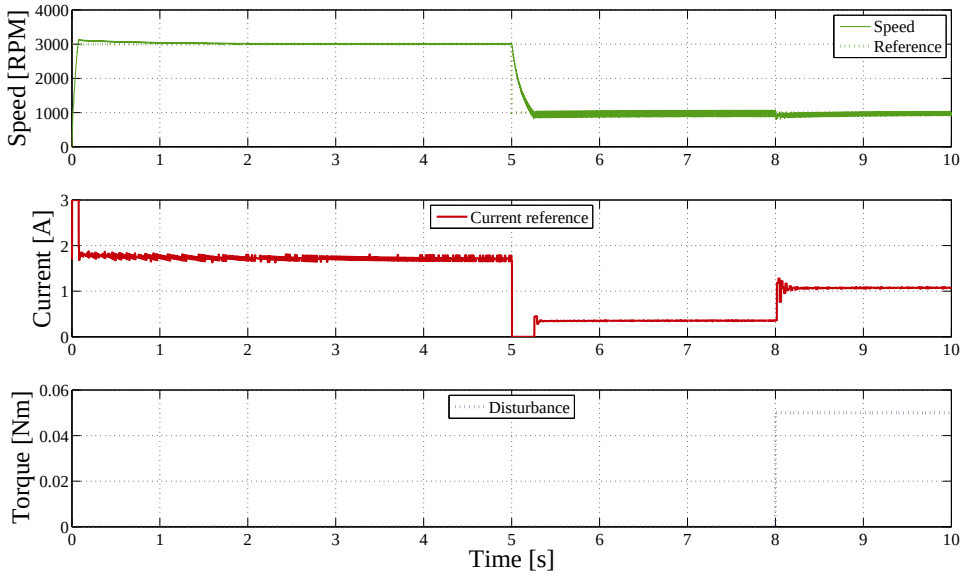

Figure 6.12: Simulated time variant controller. The moment of inertia is reduced to 50 $mg{\cdot}m^2$.

6.3.4 Simplified time variant integration

To simplify the time variant integrator, the continuous integrator is examined again in (6.22).

$$k_i \cdot \int_0^{t_2} \varepsilon dt = k_i \cdot \int_0^{t_2} \omega_{ref} - \omega dt \tag{6.22}$$

where t_2 is the end of a period as seen in Fig. 6.10, k_i is the integral gain, ω_{ref} is the speed reference, and ω is the instantaneous rotor speed. The integration in (6.22) can be done in parts as seen in (6.23):

$$k_i \cdot \int_0^{t_2} \varepsilon dt = k_i \cdot \int_0^{t_1} \varepsilon dt + k_i \cdot \left(\int_{t_1}^{t_2} \omega_{ref} dt - \int_{t_1}^{t_2} \omega dt \right) \tag{6.23}$$

Using the fact that $\int_{t_1}^{t_2} \omega dt = \frac{\pi}{2}$ then (6.23) simplifies to:

$$k_i \cdot \int_0^{t_2} \omega_{ref} - \omega dt = k_i \cdot \int_0^{t_1} \omega_{ref} - \omega dt + k_i \cdot \left(\int_{t_1}^{t_2} \omega_{ref} dt - \frac{\pi}{2} \right) \tag{6.24}$$

If the update for ω_{ref} is considered as changing in steps only updated at the start of the time interval $t \in [t_1; t_2]$, then (6.25) gives a simplified expression for integration of the speed reference.

$$\int_{t_1}^{t_2} \omega_{ref} dt = (t_2 - t_1) \cdot \omega_{ref}(t_2) \tag{6.25}$$

where $\omega_{ref}(t_2)$ is the speed reference present at t_2, despite the integrator is calculated for the entire interval $t \in [t_1; t_2]$. Using the notation in (6.18), the discrete integrator $int[k]$ can be calculated:

$$\begin{aligned} int[k] &= int[k-1] + k_i \cdot \left((t[k] - t[k-1]) \cdot \omega_{ref}[k] - \frac{\pi}{2} \right) \\ &= int[k-1] + k_i \cdot \varepsilon'[k] \end{aligned} \tag{6.26}$$

where ε' is the result of the integration $\int_{t_1}^{t_2} \varepsilon dt = (t[k] - t[k-1]) \cdot \omega_{ref}[k] - \frac{\pi}{2}$.

The proportional term can not be transformed with the same approach as used for the integral term. The proportional term in this formulation becomes time variant unlike the previous term which had a time variant integrator.

$$\begin{aligned} prop'[k] &= k_p \cdot \left(\omega_{ref}[k] - \omega[k] \right) \\ &= k_p \cdot \left(\omega_{ref}[k] - \frac{1}{t[k] - t[k-1]} \cdot \frac{\pi}{2} \right) \\ &= k_p \cdot \frac{1}{t[k] - t[k-1]} \cdot \left((t[k] - t[k-1]) \cdot \omega_{ref}[k] - \frac{\pi}{2} \right) \\ &= \frac{kp}{t[k] - t[k-1]} \cdot \varepsilon'[k] \end{aligned} \tag{6.27}$$

where $\varepsilon'[k]$ is the same error term calculated for the integrator, and $prop'[k]$ is the output of this proportional controller.

To avoid the variable gain in (6.27), it is observed that the output of the proportional controller can be calculated independently from the output of the integral controller. This independence can be used to calculate the proportional controller as described in (6.20) rather than (6.27). The combined controller response is then given by (6.28)

$$i_{ref}[k] = \begin{cases} prop[k] + int[k] & \text{if } (prop[k] + int[k]) \geq 0 \\ 0 & \text{if } (prop[k] + int[k]) < 0 \end{cases} \tag{6.28}$$

Notice that the calculation in equation (6.24) is not an approximation, but is an exact calculation of the result of the integration. In a practical implementations several factors will force a deviation from the exact integration, but most important limitations are: the resolutions of t_1 and t_2, and the accuracy of $\int_{t_1}^{t_2} \omega dt = \frac{\pi}{2}$. In the controller implementation presented here the limitation is the update frequency of the current controller of $50\,\text{kHz}$.

The magnitude of the error caused by the resolution of t_1 and t_2 is given by the ratio between the time for a stroke and the measured time limited by the resolution the time measurement[51]. The time is here limited by the current control update frequency of f_s. Since both t_1 and t_2, may be affected by the resolution the error in the speed measurement (ω_{error}) is given by (6.29):

$$\omega_{error}(\omega, f_s) = 2 \cdot \omega \cdot \frac{\frac{\omega \cdot p_r}{2\pi}}{f_s} \tag{6.29}$$

where f_s is the update frequency of the timers, p_r is the number of rotor poles, and ω is the rotor speed. So at 4000 RPM is the speed error 5.33 RPM and at 400 RPM is the speed error 0.0533 RPM, when $f_s = 50$ kHz and $p_r = 4$.

The simplified time variant controller is simulated and the response is also satisfactory as seen on Fig. 6.13, for a variable speed drive pump. The simplified time variant controller also removes the steady state error faster than the time invariant controller.

For this controller the moment of inertia is also reduced to 50 mg·m^2 and the controller gains are maintained. The response can be seen in Fig. 6.14

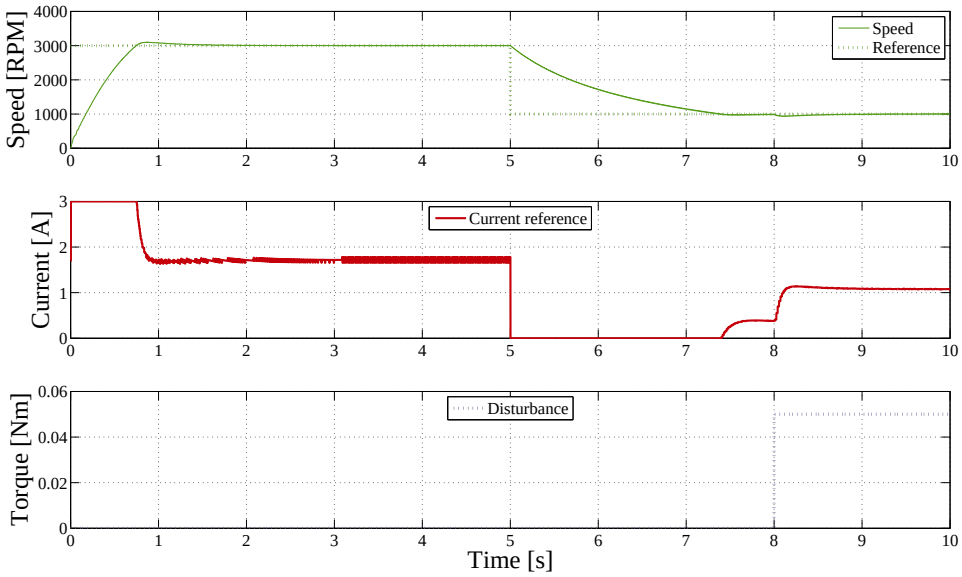

Figure 6.13: Simulated simplified time variant controller. The controller toggles between a speed references of 3000 *RPM and* 1000 *RPM, and a load disturbance is introduced at* $t = 8$ *s.*

The controller does not handle the load step as was seen for the normal time variant controller in Fig. 6.12.

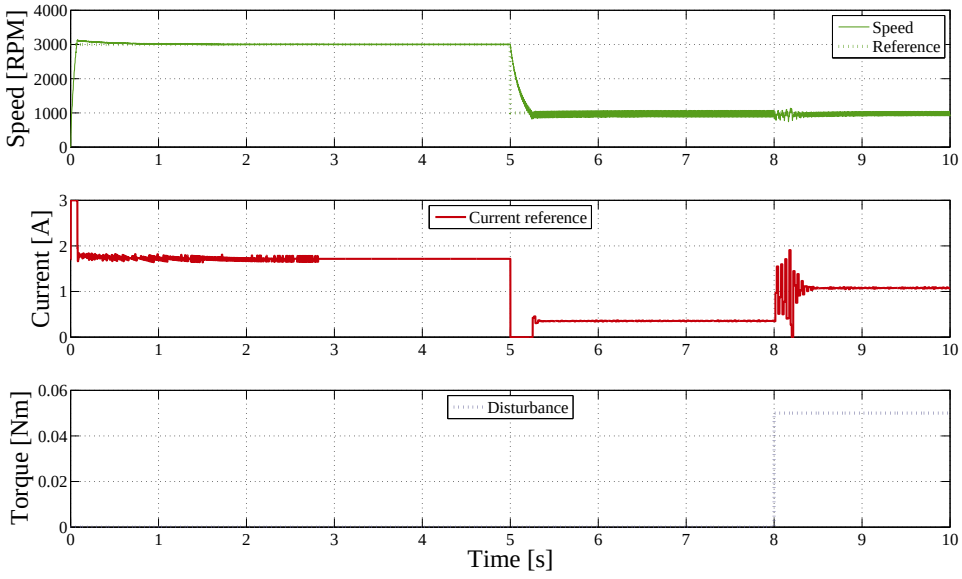

Figure 6.14: Simulated simplified time variant controller. The moment of inertia is reduced to 50 $mg{\cdot}m^2$.

6.3.5 Speed control measurement results

The three different speed controllers all have equally good performance on the physical motor in simulations, so the most promising candiate is chosen for implementation in the DSP. The time variant speed controller is set to toggle between two speeds as shown in Fig. 6.15.

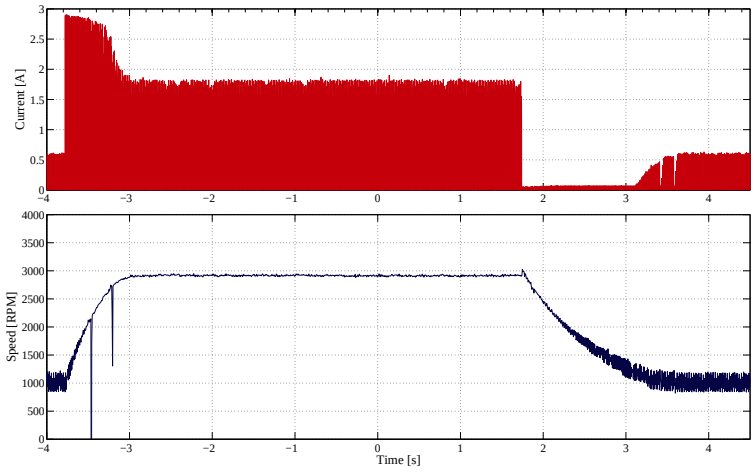

Figure 6.15: Measured speed and current of the time variant controller.

The HSRM used a fan as load, so a load disturbance was not readily possible. Instead a load disturbance was emulated by a reference disturbance as shown in Fig 6.16.

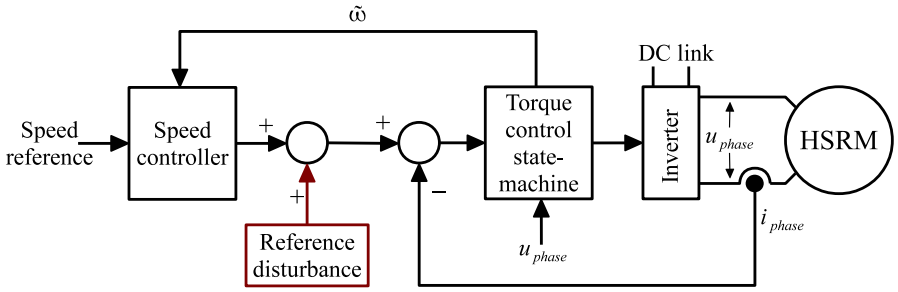

Figure 6.16: Current Reference disturbance added in the control loop.

The response, when reference disturbance was negative, is shown in Fig. 6.17. The controller recovers from the disturbance, despite the speed ripple. Since the speed ripple is periodic with a

period of four times the rotor speed and the speed controller is synchronized to the rotor speed, the measured speed does not contain the speed ripple.

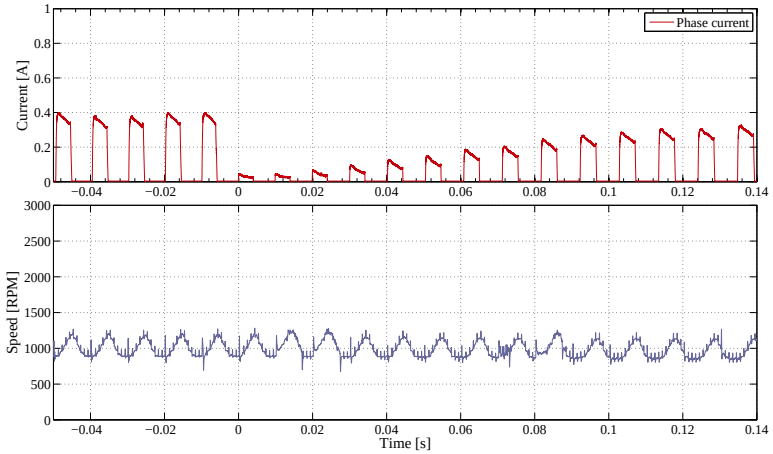

Figure 6.17: Measured speed and current with a negative reference disturbance for the time variant controller.

The response, when reference disturbance was positive, is shown in Fig. 6.18. As for the negative disturbance, the positive disturbance also is not affected by the speed ripple.

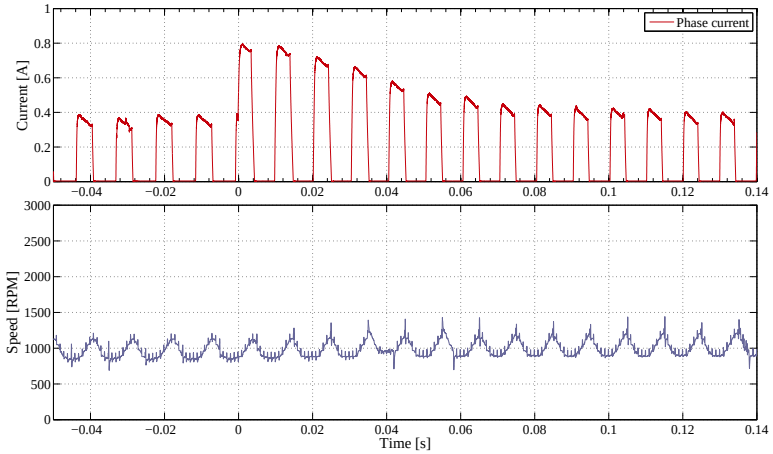

Figure 6.18: Measured speed and current with a positive reference disturbance for the time variant controller.

6.4 Discussion on control methods

The motor design philosophy used in this thesis is that the price of copper and iron will likely increase, unlike the price of power semiconductors. The price of semiconductors is either likely to decrease or the performance of power semiconductors is likely to increase without a similar increase in cost. So for the thesis a switching frequency of 50 kHz is used, but a switching frequency of 25 kHz is probably similarly useful in a practical drive.

The current controller is not optimized regarding energy consumption, since a flat top current will not achieve maximum torque per ampere control. To achieve maximum torque per ampere it is necessary to maximize the average torque per stroke for a fixed amount of input energy. Current shaping needs to be employed since the torque profile is not flat. The current could be varied to achieve maximum output power versus input power. Care have to be taken to avoid too large a torque and thus speed ripple at low speed, causing loss of stability. This may be a particularly severe problem when the machine is running position sensorless. Current shaping is possible for the first prototype and the second prototype, because their inductance is so low that the current shape can be controlled for a wide speed range.

The time-variant speed controller is not the only way to achieve speed control. Since this is a low performance drive, speed control using a classical speed controller with a fixed update frequency would also perform sufficiently. To minimize the problems for the classical speed controller it may be necessary to add a low pass filter to the speed measurement to get good steady state performance. The time-variant controller is simple to implement and since it is synchronized with the rotor, it fits the sensorless control method presented in the next chapter better than the time invariant PI-controller.

6.5 Conclusion

A cascaded controller was presented that enables variable speed control of the single phase hybrid switched reluctance motor. The inner loop consists of a hybrid hysteresis and proportional

controller. The hybrid controller ensures flat top current with a small current ripple at a fixed update frequency. The speed controller proposed here is a new time variant speed controller, that simplifies the implementation of the speed controller. Both control methods are easy to implement in a practical variable speed drive and assumes limited knowledge of the individual motor. This chapter showed that the control of the HSRM is very simple and compared to the complexity of the calculations needed for vector control for a permanent magnet synchronous motor (see appendix G for details). The designed control methods are implemented and tested on the first prototype. Combined control methods presented in this chapter forms the basis for the position sensorless control method presented in the next chapter.

Chapter 7

Sensorless control

Like the brushless DC-motor (BLDC) and the permanent magnet synchronous motor (PMSM), the HSRM needs information about rotor position to be properly controlled. Placing a position sensor in the motor for pump systems for central heating may complicate manufacturing, since the air gap in the pump motor is normally flooded with hot water. Removing the position sensor may also help lowering the cost of low power drives [96]. For BLDC, PMSM, induction motors, and the normal SRM position sensorless methods are relatively well established and have been used for some time. Some of the methods for the SRM and BLDC may be adopted for the HSRM, but care have to be taken since some of these methods assume that the motor has more than a single phase. For the single phase switched reluctance motor several methods have been used, and some of these methods are presented below. For the single phase hybrid switched reluctance motor there seems to be no known methods yet.

A position sensorless method for the single phase HSRM is presented in this chapter, which is simple to implement. The method does not depend on other parameters than moment of inertia, and knowledge of starting torque. The chapter starts by describing different position sensorless methods applied to permanent magnet motors and SRM. Then the proposed position sensorless method is presented followed by measurement results. The chapter is concluded with an evaluation of the position sensorless method.

7.1 Sensorless control methods

The position sensorless methods presented in this section are divided into a few categories based on the overviews presented in [63] and [51]. There is some overlap between the categories for the methods presented here and common to all methods is that they use the relationship between rotor position and flux linkage. All the methods try extract a signal, based on flux linkage, that reveals the rotor position.

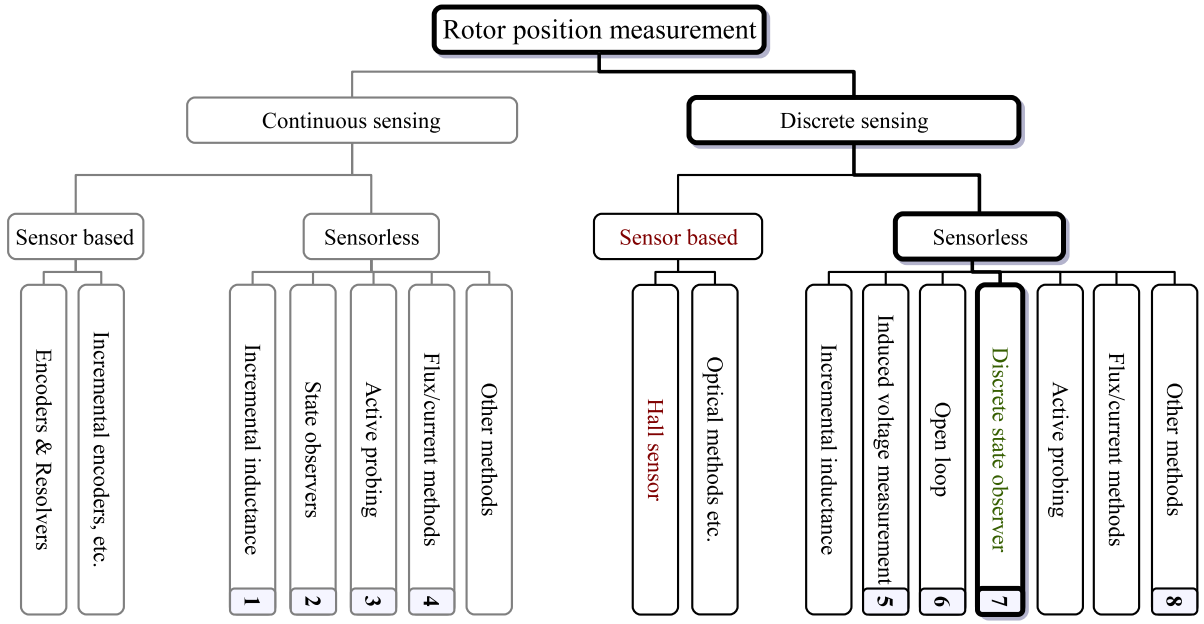

Figure 7.1: Overview over some of the sensorless methods for switched reluctance motors based on the overviews presented in [63, 97, 51]. The method applied in this thesis is highlighted with a thicker line. In [5] a hall sensor was used.

1. Incremental inductance

   These methods rely on the direct connection between inductance and rotor position in machines with a saliency on the rotor[51]. The methods using this principle may need to have good models of self-EMF and ohmic losses, if the inductance is to be reliably determined[51]. No extra signal is normally injected to detect the rotor position.

2. State observer

   By feeding a state space model of a motor with the currents and voltages, the state space

model may estimate the rotor position[51, 63]. A practical example of an back-EMF based observer for position sensorless control of the permanent magnet synchronous motor can be found in[98]. A new trend seem to be to use neural networks as state observers. A well known problem for neural networks is overfitting[99], where a network is trained to high performance on specific machine, but does not perform well on another machine due to parameter variations. Such problem seems to have occurred for a neural network applied to sensorless control of a single switch, two phase switched reluctance motor in [100]. Here the control failed control of the real machine after having been fitted very closely to the simulation model. The solution was here to use training and fitting on the real machine. The method delivers impressing results, but the overfitting of the neural network may be a problem in mass production setting. A method to handle varying parameters is to use online parameter estimation as in [101], but such a method can not be applied to neural networks without adding online training as well. One of the few sensorless control methods applied to single phase BLDC motors is presented in [102]. The author also uses a flux linkage estimation to continuously estimate the rotor position, but acknowledges that this method is sensitive to the accuracy of the flux linkage estimation.

3. Active probing

   Injecting a small current into either the controlled phase or an unenergized phase, will give different responses due to the varying incremental inductances[51, 63]. The small current injected will affect the torque production, but this method does enable a high resolution of the rotor position. Such active signal injection is used in [103] to detect the initial rotor position for sensorless direct torque control of a permanent magnet synchronous motor. See [104, 105, 106, 103] for details on direct torque control. In [107] it is suggested that the permanent magnet motors are designed with a saliency so signal injection can be used.

4. Flux/current methods

   The flux linkage is like to incremental inductance rotor position dependent in switched reluctance motors. Similar to the methods applied for permanent magnet synchronous motors[104], flux linkage can be calculated by integrating the voltage applied to the phase after the voltage drops on phase resistance and transistors is subtracted. Since the current

is known, look-up tables may then be used to determine the rotor position. The look-up tables may be formed based on measurement or from finite element simulations. Any integration is sensitive to drift[108] and also needs to compensate for the increase in phase resistance due to increased winding temperature.

5. Induced voltage measurement

   Cross coupling between phases can be used in polyphase SRM, for position detection. But if the cross coupling is small the voltage induced in a non-energized phase may be rather small. Permanent magnet machines has a back-EMF, generated by the varying flux linkage between the motor windings and the permanent magnets on either rotor or stator side. In a three phase BLDC, one of the phases is not conducting any current and the back-EMF may directly be observed. Such control of the BLDC is further described under "Discrete state observer". For a three phase PMSM, the back-EMF can also be used for position sensing, but the back-EMF can not directly be sensed as for the BLDC. The measured phase currents are compared with calculated phase current based on model that tracks the expected state of the PMSM. But back-EMF based methods are limited to rotor speeds where the back-EMF can be reliably detected[109].

6. Open loop

   If the dynamic control requirements are low it is possible to run most motors in open loop. Stepper motors are often in open loop mode with no position sensor. But also for induced voltage measurement methods, the start up may be performed in open loop. This is only possible if the load is low in the beginning as is the case if the machine load is a fan or a centrifugal pump.

7. Discrete state observer

   The back-EMF method is used extensively in brushless DC-motors as in [110, 111, 112, 113]. Typically only two phase are active at any given time in a three phase brushless DC-motor. A state machine tracks state of the inverter, and since the BLDC is synchronous, it also has a discrete tracking of rotor position. If the voltage over the non-conducting phase is monitored synchronized with the switching in the two active phases, the position is known at discrete points by watching for zero-crossing of the back-EMF. Based on the

speed, a delay , and the current switching state, the next switching state can be calculated. The main problem for the BLDC, in sensorless control is during start up, when back-EMF has a relatively low magnitude[110, 111, 112, 113]. Both [110] and [111] present different strategies to get full torque during start up. An open loop start up method is used in [114, 112, 113] . For a detailed overview of an practical implementation of position sensorless control of a BLDC in an 8-bit microcontroller, [114] seems like a good resource.

One of the few sensorless methods proposed for sensorless control of a single phase motor that seems practically feasible for mass production is for a single phase BLDC in [115]. Here the single phase winding is used both to drive the motor and as sensing coil. The BEMF is monitored when there is no current in the coil. Since the back should cross zero at this time, the position estimate can be updated once per period. The method is not sensitive to variations in flux or phase resistance. Like all back-EMF based methods, care has to be taken at low speed. At low speed the current can only be in the phase for a short time to allow for a clear detection of the back-EMF. This means at low speed the motor can not give full torque. Since this BLDC is for a small fan, this does not seem a serious issue.

8. Other methods

This category includes methods based on eddy currents[51], the current gradient method proposed in [116], and sensing coils. The most interesting method is the current gradient method. The detection method uses the change of the derivative of the phase current to detect the position where a rotor pole and stator pole start to overlap, giving one position update per energy conversion[116].

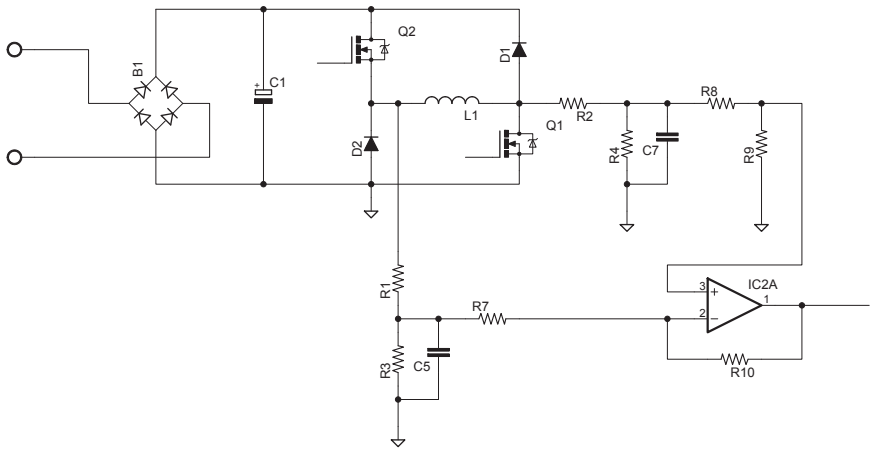

Figure 7.2: The sensor circuit is a simple difference coupling of an operational amplifier. Another option would be to directly couple the resistive dividers to the DSP or to use a single supply operational amplifier. The differential amplifier using dual and single supply are however more robust towards variations in the DC-link voltage.

7.2 Proposed sensorless method

Since there are permanent magnets present in the stator and the flux linking the permanent magnets with coils is changing with the rotor position, a back electromotive force (back-EMF) is induced in the motor phase. When no current is in the coil, the BEMF, can directly be observed. It can be observed that the changes in flux linkage as a function of the angle is zero at angles close to 0 and $\pi/4$ radians. The induced back-EMF will thus at these places become 0. So, when there is no current in the phase, the rotor position may directly be sensed. The BEMF is sensed by measuring the differential voltage across the phase impedance as it is seen on Fig. 7.2.

The BEMF-measurement is thus independent from a varying DC-link voltage, which will occur when using a rectified AC-source. It is important note that the diodes in the inverter, does not immediately stop conducting when the machine is defluxing, but may be rather slow in shutting down. To avoid measuring this diode voltage drop, a little extra time is needed after current is sensed to be zero, before motor BEMF can reliably be sensed.

The BEMF can be measured even at relatively low speed, as it is shown in Fig. 7.3. The BEMF is measured with machine being spun manually at approximately 640 RPM.

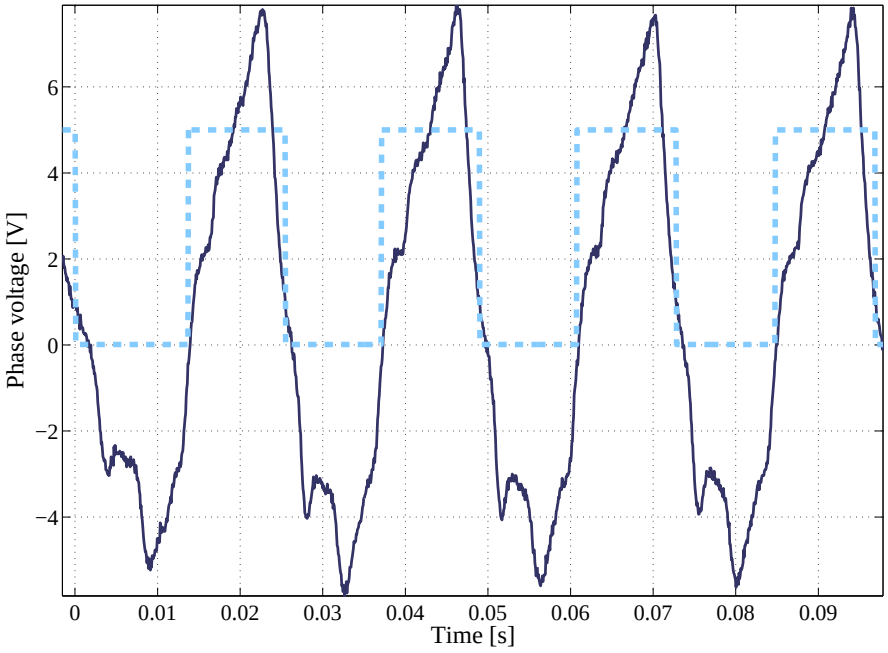

Figure 7.3: The BEMF is here related to the angle measured with an 8000 point encoder. The encoder signal goes high at -3 degrees mechanical and goes low at 42 degrees mechanical, for a span of 45 degrees. These point illustrates ideal turn on and turn off at low speed (less than 4000 RPM).

The purpose of this sensorless control is get sufficient information about the rotor position so the single phase HSRM can be properly controlled. The sensorless control method do not need to supply a continuous estimation of the rotor angle, because the machine is operated in strokes. Since the machine is controlled in strokes, the most critical pieces of information are: When phase current should be turned on and off. The method proposed here will supply both the current turn on time, the current turn off time, and also detect if the rotor has stalled.

When the machine is operated it can be considered progressing through some discrete states as it can be seen in Fig. 7.4 and decribed below:

State A - Current control: The current controller tries to achieve a flat current with a level determined by the speed controller. The two transistors are operating in PWM.

State B - Defluxing: The machine is defluxing the stored magnetic energy through the diodes to the DC-link capacitor.

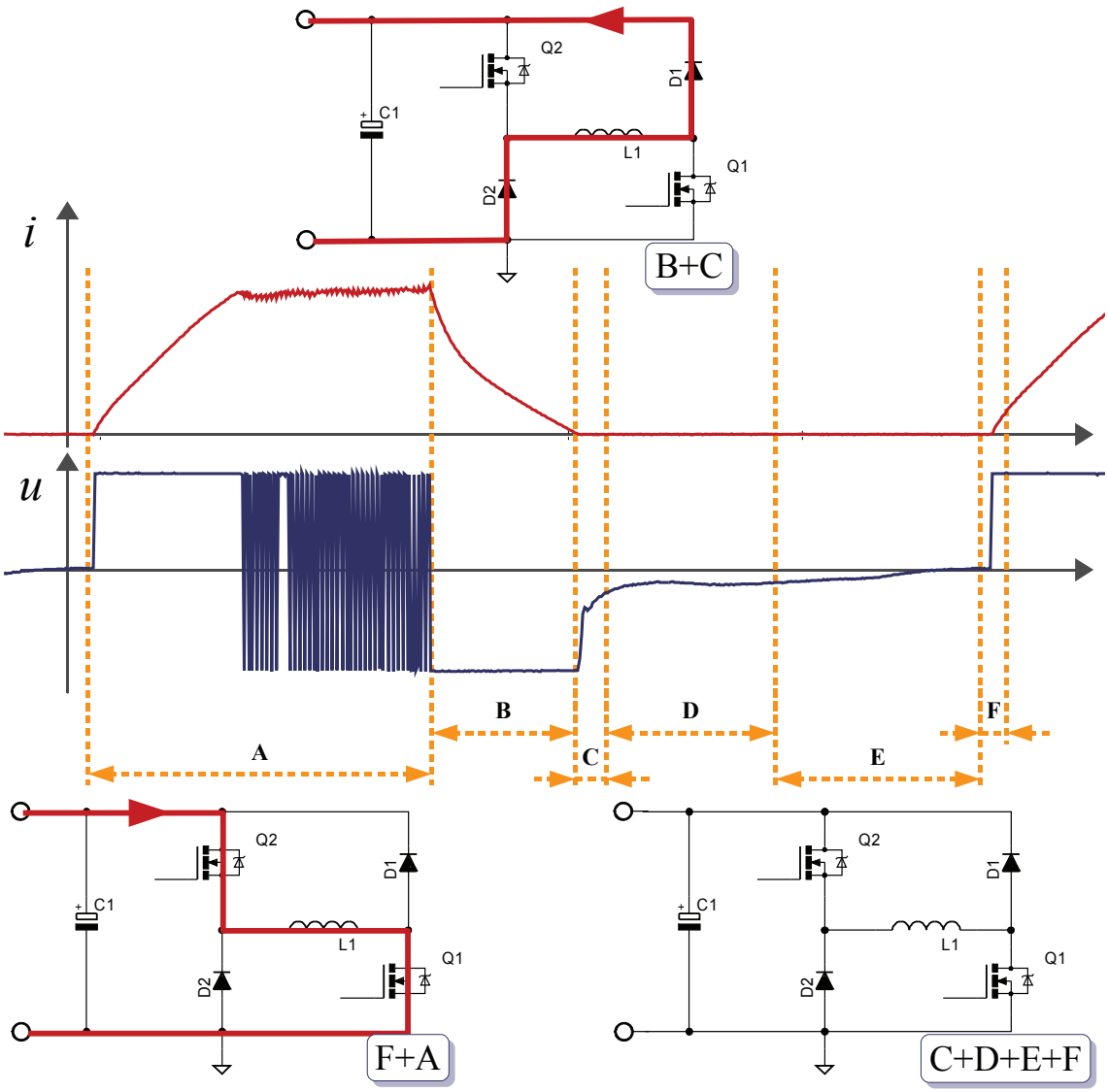

Figure 7.4: The inverter and thus the motor goes through a series of states. First the inverter is energizing (or fluxing) the phase winding, followed by a defluxing state, and before the next stroke the inverter is in a non-conducting state. The sensorless control states are marked with a letter described in the text.

State C - Ensure stand off: When the current reaches zero, the diodes will stop conducting and the back-EMF can be directly sensed. The main limitation is set by the limits to operational amplifiers common mode rejection for high frequency common mode signals, here in the order of $10 - 100$ kHz for the used LM741 operational amplifier. A delay is also induced by inverter parasitics, since the diodes does not immediately block, but shuts down after $10 - 30\,\mu$s. The signal is further delayed by the optical isolation and extra filters before the signal reaches the DSP. The DSP can also not reliable detect when the current is truly

zero, because of noise in the measurement. The more noisy the current measurement is, the sooner this would occur. The longer the stand off period is chosen to be, the more stable the controller will be. The extra stability comes from the fact that turn on should never occur too close to turn off. The downside of a long stand off period, is that it directly limits the maximum speed achievable in position sensorless operation. The maximum stand off time should be less than one quarter of a full stroke. Since three states occur after the stand off period they also have to be considered, so the stand off is determined as given in equation (7.1)

$$\begin{aligned} counter_{standoff} &< \frac{1}{4} \cdot \frac{f_s}{\left(\frac{\omega_{max}}{2\pi}\right)} - 3 \qquad \Updownarrow \\ counter_{standoff} &< \frac{\pi}{2} \cdot \frac{f_s}{\omega_{max}} - 3 \end{aligned} \tag{7.1}$$

where ω_{max} is the maximum speed in radians per second.

State D - Negative EMF: If the measure back-EMF is negative, the motor is in the expected state. This is used to detect if the rotor has stalled.

State E - Check zero crossing: When the back-EMF crosses zero, then the time since last zero crossing is found. If it is assumed that the back-EMF has a zero crossing at zero degrees, linearly increasing to positive peak value ($\hat{U}_{back-emf}$) at an angle of 40 $^\circ$ mechanical, The turn on angle error (θ_{error}) may be approximated based the magnitude of the noise floor for the back-EMF measurement ($\hat{U}_{noise}$) as seen in (7.2).

$$\theta_{error} \leq \frac{\omega_{nominal}}{\omega} \cdot \frac{40^\circ}{\hat{U}_{back-EMF}} \cdot \hat{U}_{noisefloor} \tag{7.2}$$

where $\omega_{nominal}$ is the nominal speed, at which the peak back EMF is $\hat{U}_{back-emf}$. The equation basically states that the back-EMF has to be so large, that the back-EMf can be seperated from the measurement noise. For the first prototype, at the lowest speed(400 RPM), the position error calculated to be less than 3 $^\circ$. If the turn on angle happens 3 $^\circ$ too soon then the average torque drops to 78% of the nominal torque for the stroke. If the turn on angle is 3 $^\circ$ too late, the average torque drops to 81% of the nominal torque for the stroke.

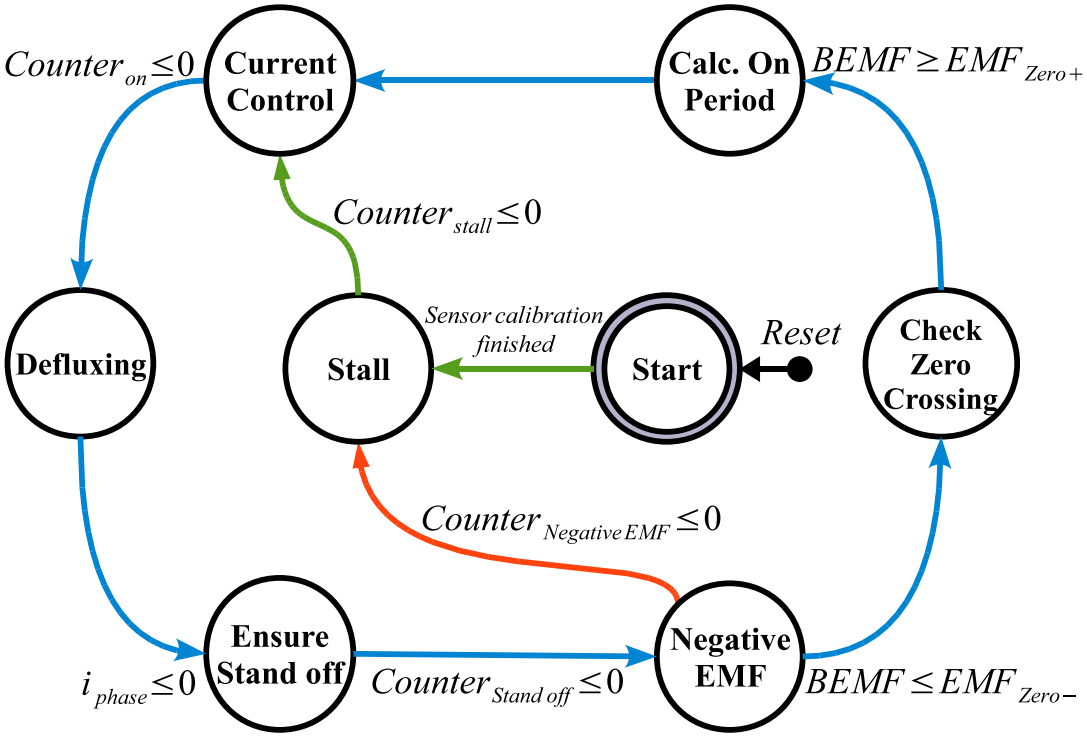

Figure 7.5: The torque control state machine has to handle current control and BEMF sensing. The BEMf cannot be sensed when there is current in the phase, and thus current control and BEMF sensing cannot performed at the same time. After a stall procedure has been performed, the torque control state machine is set to handle current control with a fixed value for the counter. The counter is decreased every time the current control is updated. The counter is updated continuously based on the time between zero crossings.

The net torque is still positive and the position sensorless control can still recover from this.

State F - Calc. on period: Now the time to have current in the winding can be found. The next state is now : state A - Current control. To minimize the the lag between the speed is measured and it is used to control the motor, the calculation of the duration of the current control is done in parallel with the current control.

Since the machine progresses through a sequence of discrete states, it is obvious to the track the rotor behaviour with a state machine. For a description of statemachines, see [117]. Based on Fig. 7.4 a sensorless statemachine can be designed as it is shown in Fig. 7.5. The statemachine shown in Fig. 7.5 can then be implemented as it is described in appendix F.

7.2.1 Sensor calibration

Start up consists of calibrating sensors to compensate for drift and to determine what is the level of noise and what value has a zero BEMF. Measurement of noise level is needed since it is important to distinguish positive and negative BEMF from measurement noise. The calibration enables lower sensorless speeds, but also means that the lowest possible speed depends on the current noise level.

7.2.2 Turn on point

Turn on should happen slightly before back-EMF crosses zero. The motor is designed with a relatively low inductance, so turn on angle is not advanced for speeds up to at least 4000 RPM.

7.2.3 Turn off point estimation

Note that it is only needed to have current in the phase approx. 50% of the time of the full stroke. Since the position may be sensed, speed can be inferred based on the time between zero crossings of the BEMF. The estimated speed is thus given by $\tilde{\omega} = \frac{\pi/2}{\Delta t}$ at every turn on instance. The duration of a stroke, the turn off time is calculated by the following:

$$counter_{on} = 0.4 \cdot counter_{Zero\ crossing}; \tag{7.3}$$

7.2.4 Stall

The first stroke has a predetermined turn off point estimation, that is the same to say that $counter_{on}$ is set at a fixed value. For a fan load the starting torque is approximately zero, and the speed change is primarily limited by the moment of inertia. So the time it takes to accelerate the machine to a given minimum can be approximated by (7.4).

$$\frac{d\omega}{dt} \approx \frac{\tau - 0}{J} \Leftrightarrow \frac{\Delta\omega}{\Delta t} \approx \frac{\tau}{J} \Leftrightarrow \frac{\Delta\omega \cdot J}{\tau} \approx \Delta t \tag{7.4}$$

where $\Delta\omega$ is the change of speed from

Based on (7.4) the value of $counter_{on}$ can be found as given in (7.5).

$$counter_{on} = \frac{\Delta t}{2} \cdot f_s \approx \frac{\Delta\omega \cdot J \cdot f_s}{2 \cdot \tau} \approx \frac{\omega_{min} \cdot J \cdot f_s}{2 \cdot \tau} \tag{7.5}$$

where ω_{min} is the minimum speed for which the back-EMF can be reliably detected (see (7.2)) and τ is the average torque at full current at zero speed (see (6.9) at page 100). The steady state torque calculated from the finite element analysis or the measurements will suffice.

If the cogging torque is lower than load torque during the first stroke, the speed will decrease and the machine can not be run sensorless. Since this motor is to be used for pump drives this is not normally an issue, except in conditions where particles are stuck between the rotor and stator. The error handling will detect the stall and try to perform a restart. This process may release the stuck particles, otherwise the process is repeated.

The sensorless method assumes that the HSRM after the first stroke has reached a speed, where the back-EMf can reliably be detected. To ensure this the time between retries has to be set sufficiently high to ensure that the rotor is at stand still before the first stroke.

7.2.5 Error Handling

Fault detection is required for a motor drive operating outside a controlled experimental set up. Some general fault detection and identification algorithms for motors presented in [118][119] are for induction motors and BLDC respectively. The methods presented in [119] assume sinusoidal currents for detection and thus not useful here. Some of these problems are overcome in [118], but it does however require on-line adjustment of some key parameters to avoid detecting non-existing errors. In [72] focuses on six errors occurring a centrifugal pump:

1. Inter-turn short circuit in the stator.

2. Clogging inside the pump.
3. Increased friction due to either rub impact or bearing faults.
4. Increased leakage flow in the impeller of the pump.
5. Performance degradation due to cavitation.
6. 6. Dry running.

A complete fault detection algorithm is outside the scope of this thesis, and only clogging inside the pump is handled here.

The detection is rather straight forward: Since the BEMF generated generates both a positive and a negative voltage, they are used to detect if the motor is truly running. If there is no negative BEMF within a the maximum time for two strokes at the lowest speed, the machine has stalled. The detection of the magnitude of the BEMF is only possible if the differential voltage is measured. An analog zero-crossing detection using a comparator would not give information regarding the magnitude and sign of the BEMF.

7.2.6 Simulation Results

The steady state performance of the position sensorless controller is very much similar to the operation of the controller using a position sensor as it can be seen in Fig. 7.6. The time variant speed controller from last chapter is used as speed controller for both the simulations presented here and it is also used for the experimental results presented later.

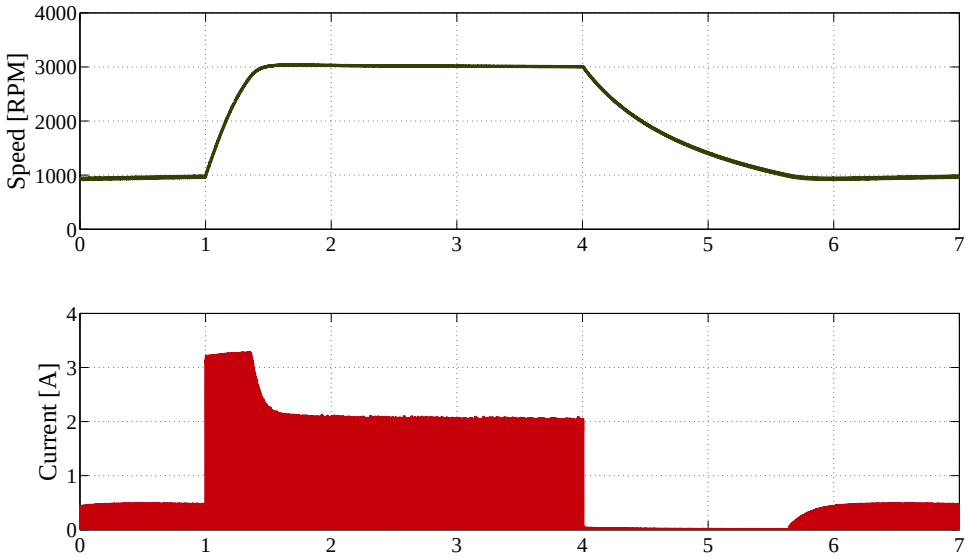

Figure 7.6: Position sensorless controller toggling between two speed references.

The start up is not entirely like it would be in the actual implementation, since embedded M-scripts in the simulations are not initialized in the same way as the actual implementation. This is not a serious complication, because the position sensorless controller constantly resynchronizes with the rotor. The simulated position sensorless start is shown in Fig. 7.7. Prior to the initialization of the speed controller the current reference is at 1.5 A as it can be seen Fig. 7.7 at (1). The initial active part of the stroke is calculated as in (7.5). When the active part of the stroke ends at (2), the state machine progresses through the states that ensures that the state machine is synchronized with the rotor. The active part of the second stroke is estimated based on the difference in time between the initialization of the state machine and the back-EMF zero crossing. Because of the way the state machine and the speed controller are implemented in the simulation, the estimated speed for the first stroke is to high and the estimate for the second stroke becomes to short. The state machine avoids an improper resynchronization at the wrong zero crossing, because it does not look for back-EMF zero crossing, before it has found the negative back-EMF at (4). The state machine is finally resynchronized with rotor at (5).

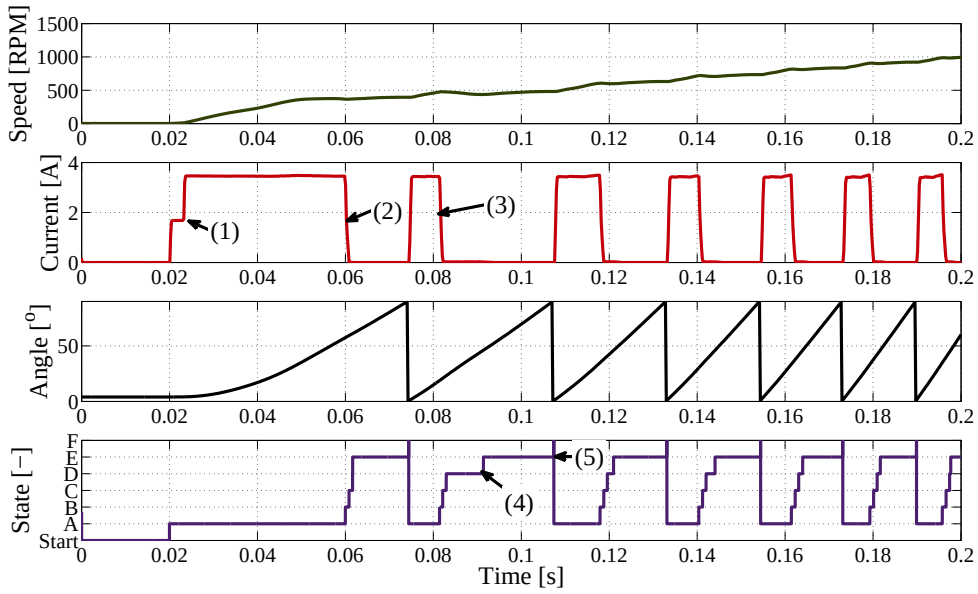

Figure 7.7: Position sensorless controller start up with the internal states of the position sensorless state machine.

7.3 Experimental results of position sensorless control

The proposed position sensorless control method is supposed to be dependent only on few motor parameters: average torque for the first stroke, moment of inertia for the motor and the load, maximum phase current. The motor torque load has to be low at low speeds, but can increase at higher speeds. To test this the position sensorless method is first used together with the first prototype, secondly it is briefly tested with the HSRM pump motor.

7.3.1 Experimental results of position sensorless control of the first HSRM prototype

The results from implementation of the proposed sensorless method is shown in this section. The experimental control system is implemented using a TI TMS320F2812 micro controller for all drive control. The current is sampled through a second order low pass filter, removing the demand for switching synchronized sampling. The inverter uses two Fairchild FCH47N60_F133 MOSFET and two International Rectifier 15ETH06FP diodes for the test. The back-EMF is measured optically isolated from the micro controller using a HCPL-7800. This type isolation requires that the analog signal has to be scaled to $\pm$200 mV prior to optical transmission and after the optical transmission it is amplified before used with the micro controller.

Sensorless start up performance

A critical part of a position sensorless control is how the start up is handled. The position sensorless controller presented here is using a feature of HSRM in the start up: the magnitude of the back-EMF can be sensed after the initial stroke, since the HSRM can deliver enough torque during the first stroke for the rotor reach a sufficient speed.

The start up shows how the position sensorless control recovers from the error introduced by the first stroke in the speed calculation. The implied assumption that the speed does not change

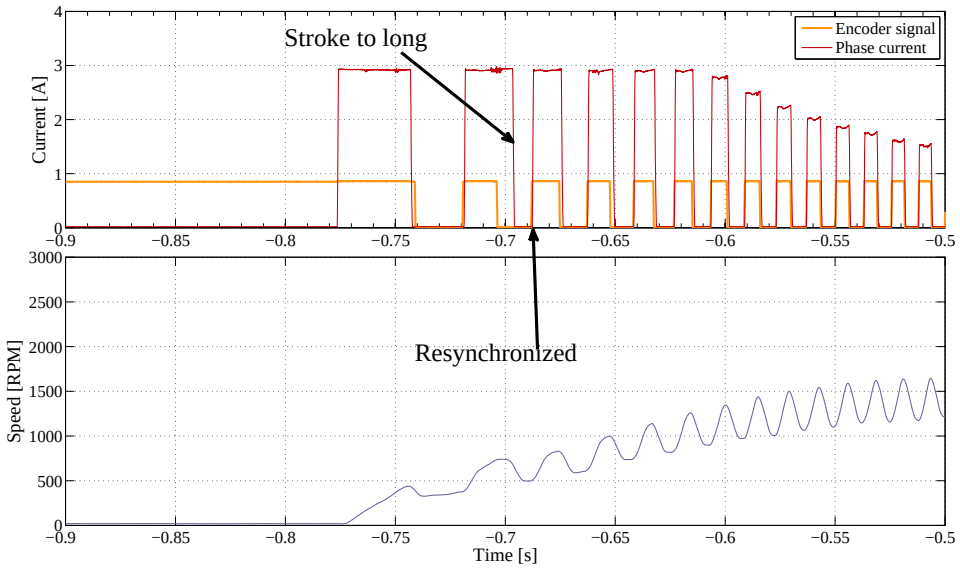

Figure 7.8: Startup is initiated and the machine spins up under position sensorless control.

much between strokes is used to calculate the time between current turn on and current turn off. This assumption is wrong after the first stroke and the next stroke will thus be affected. The rotor is resynchronized at the next zero crossing and eventually the controller is synchronized at given rotor speed.

In Fig. 7.8 it can be seen that the position sensorless controller does not estimate the correct duration for the active part of the stroke.

Since the assumption for the turn off time calculation is that the speed does not change too much, the start up will show the turn off time is not calculated correctly.But a miscalculated turn off time normally means that the speed does not increase as much as it could have, but this means that the following stroke is calculated more accurately.

Resynchronization is important, since most of the torque production occurs at the start of stroke. To achieve resynchronization the back-EMF is monitored as described before. The estimated rotor speed is too low after the first stroke and the active part of the second stroke is thus too long as seen in Fig. 7.9. The active part of third stroke is however too short and the speed does not increase significantly. As the speed increases the estimation of the speed also becomes more

accurate when the speed does not change between strokes.

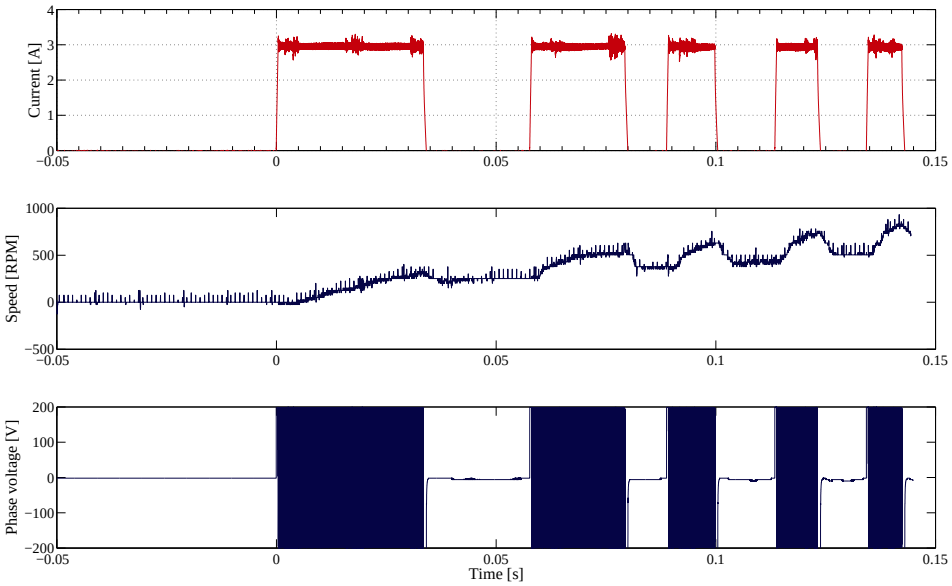

Figure 7.9: A more detailed look at the startup.

The difference between simulation and measurement in behaviour in start up is primarily caused by differences in the implementation of the initialization of the controllers in the simulation and in the micro controller. The resynchronization does however behave as expected and ensures a reliable start up despite these differences.

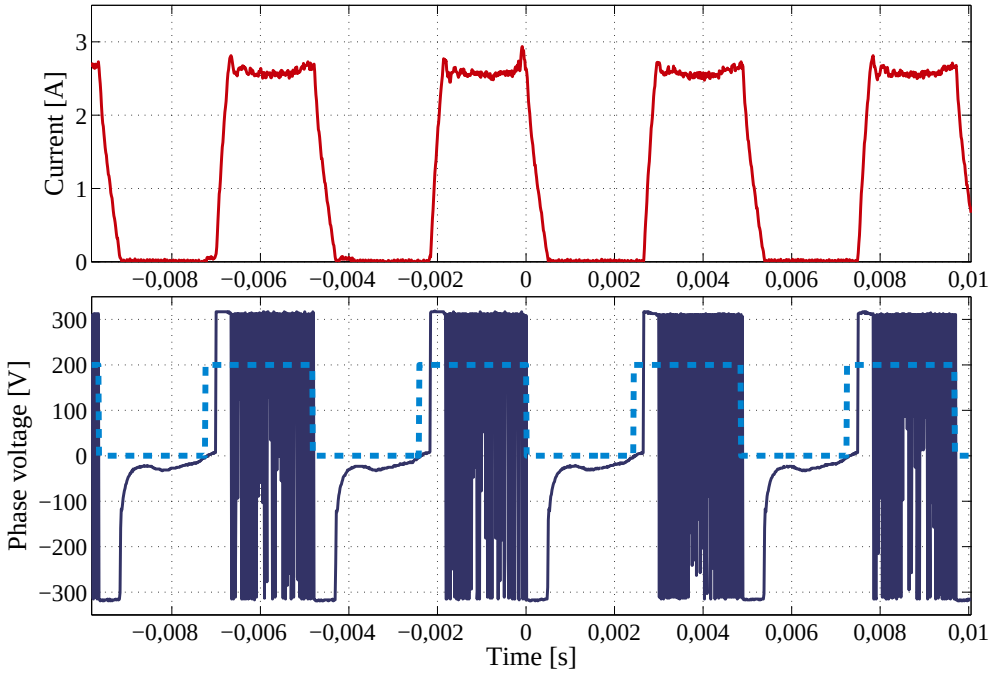

Figure 7.10: This plot shows steady state performance of the sensorless control, displaying the phase current, and phase voltage both related to the angle measured with an 8000 point encoder.

Performance after start up

The steady state performance of the position sensorless control can be seen in Fig. 7.10. To verify the position estimation, an output pin on the microcontroller was set to toggle high and low based directly on an encoder signal. The error between the sensor based estimation of the turn on angle and the position sensorless estimation is less than 1° mechanical.

The accuracy of the position sensorless controller at lower speeds will be lower than the accuracy at higher speeds, since the back EMF of the HSRM has a lower magnitude than it will have at higher speeds. The accuracy is still less than 3° mechanical at 1000 RPM as can be seen in Fig. 7.11.

The speed controller is set to toggle between 3000 RPM and 1000 RPM, and the response can be seen in Fig. 7.12.

When the defluxing current through the diodes has ceased, there is a small delay prior to the

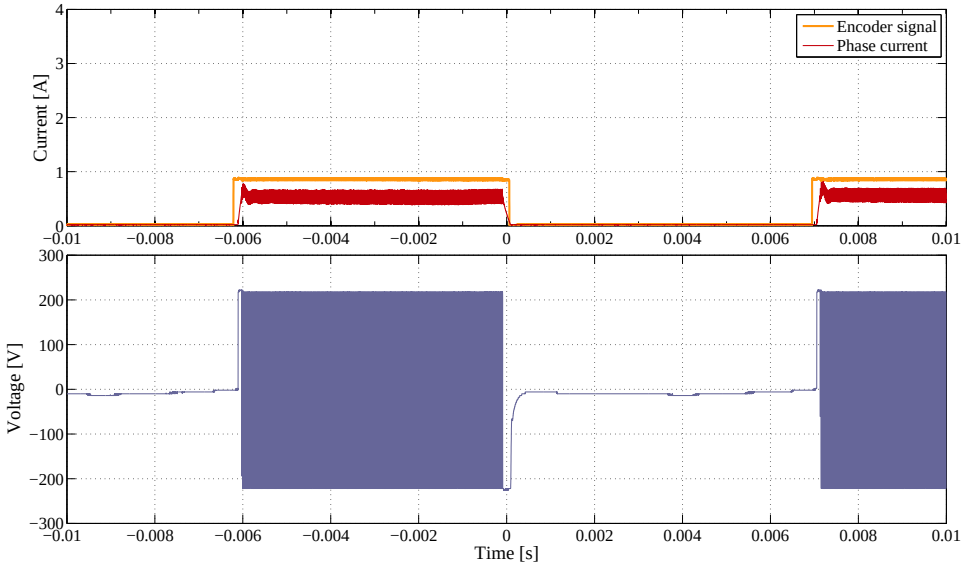

Figure 7.11: Performance of position sensorless controller at 1000 *RPM.*

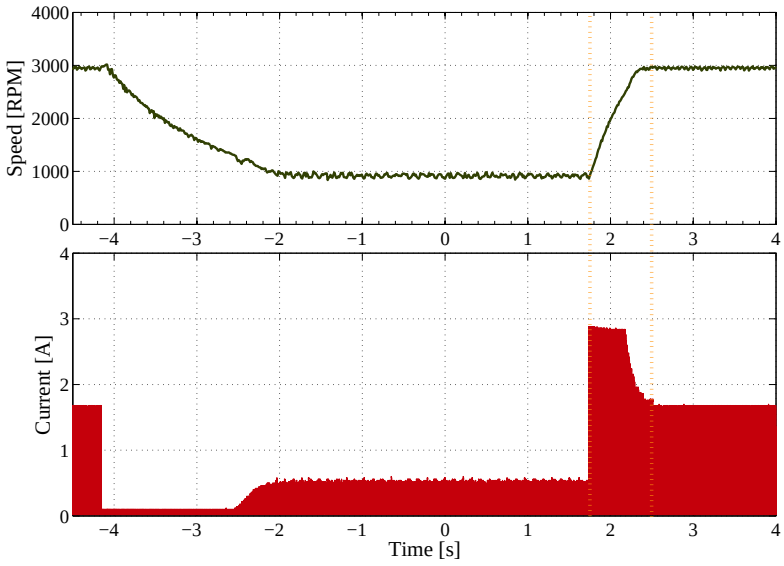

Figure 7.12: The motor is toggled between two speeds and the currents and speeds are recorded. The speed is measured using the position sensor and calculated in the micro controller and output through a low-pass filter PWM output.

voltage drop across the diodes does not affect the differential measurement. This is handled in the micro controller by waiting a fixed amount of time after the current is measured to be zero, before monitoring the BEMF. The shut-down delay can be seen in a closer look of the differential

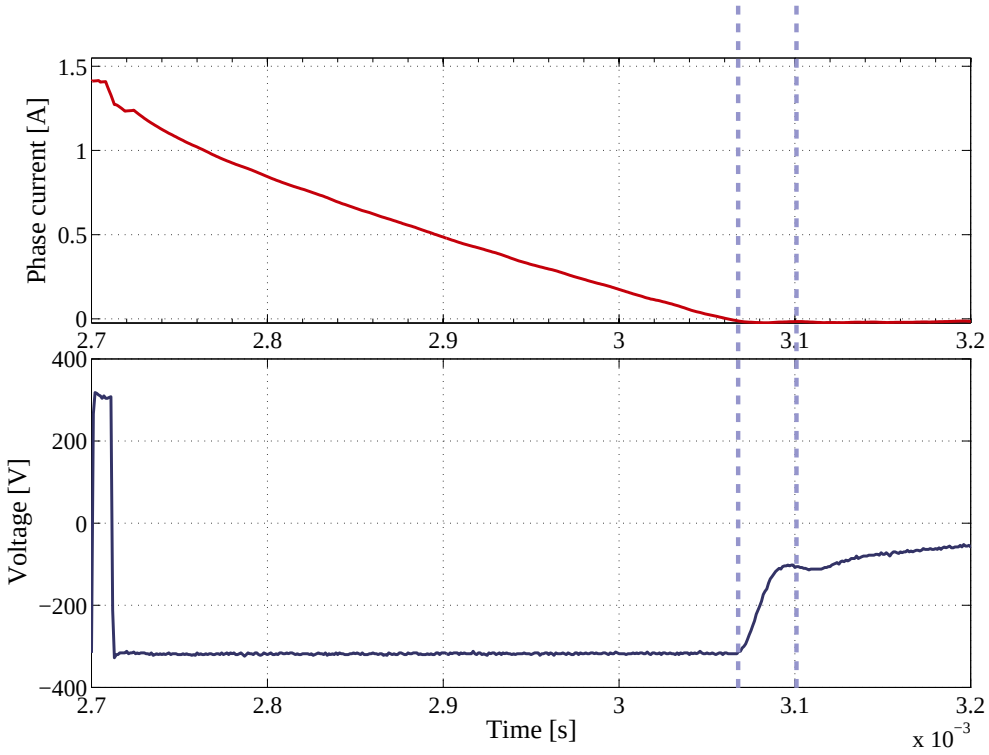

Figure 7.13: The phase voltage measured with a differential probe, shows that the diodes influences the phase voltage after the current has dropped to zero.

Table 7.1: Efficiency versus load.

Output	System eff.	Inverter eff.	Motor eff.	Copper loss/motor input
72.5 W	72 %	94 %	77 %	15 %
47.8 W	57 %	89 %	64 %	16 %
31.3 W	48 %	89 %	54 %	19 %
18.4 W	47 %	81 %	59 %	21 %

voltage and phase currents shown in Fig. 7.13.

The efficiency at different power levels is presented in table 7.1. The input power to the inverter and the output power of the inverter is measured using an Omicron D6100 power analyzer. The system efficiency is defined as the output power of the motor on the shaft versus the input DC-power. System efficiency also includes the mechanical losses of the motor and the losses in the inverter. This means that the peak efficiency of the motor alone is 77 % at 72.5 W output power, including bearing losses and iron losses.

The results are treated in the discussion later in this chapter.

7.3.2 Sensorless control of HSRM in a pump system

The second motor design presented in chapter 5 is put into a pump system as it is shown in Fig. 7.14. It was not possible to ensure that the motor did leak water during the experiments, and the motor was tested with over current protected DC-supplies which reduced the voltage available for drive testing. No encoder is connected to the shaft and the error in the rotor position can thus not be measured.

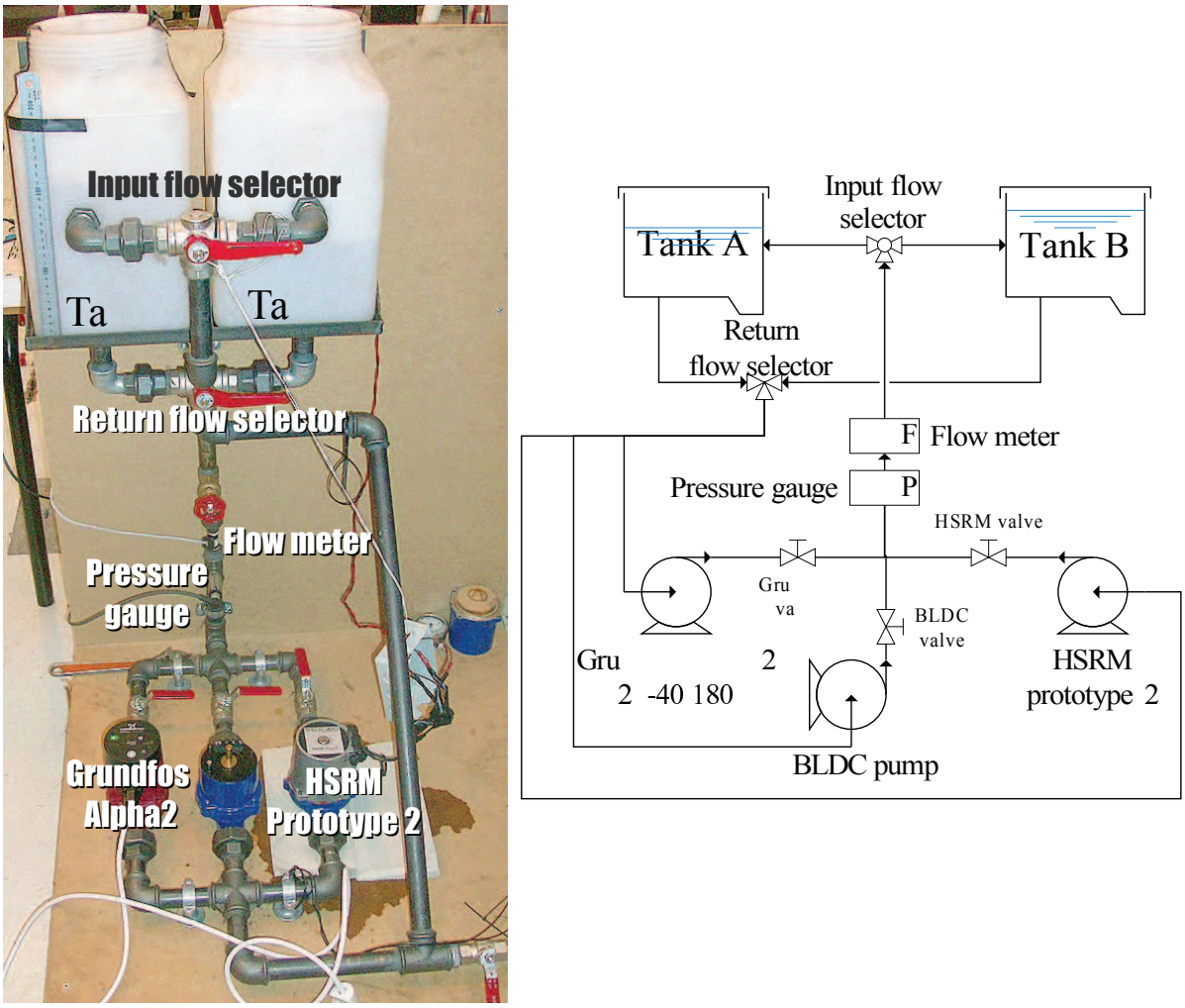

Figure 7.14: The pump test set-up used for testing the HSRM in a pump system

The sensorless control software in the micro controller is modified to handle the smaller moment of inertia and smaller torque as described in equation (7.5). The start up phase current and phase voltage is recorded as it is shown in Fig. 7.15. The HSRM starts reliably, even if the HSRM pump

motor has been disassembled, though after stiction is a bigger problem for the pump HSRM. The position sensorless controller retries are automatically handled by the sensorless controllers state machine.

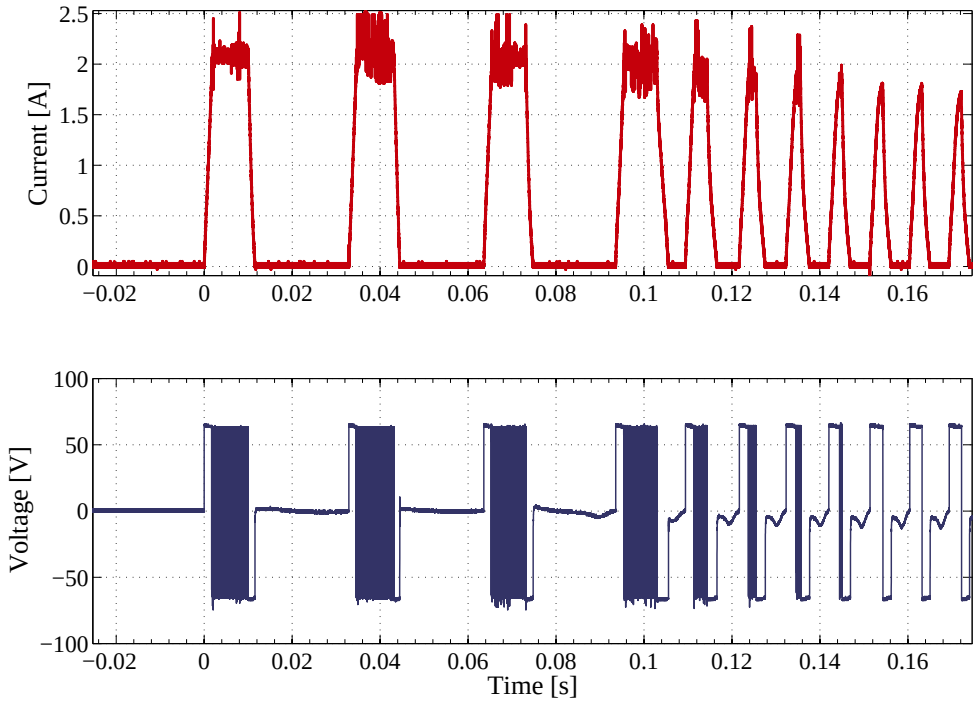

Figure 7.15: The measured current and phase voltages of the HSRM at start-up in a pump system.

.

The start up seen in Fig. 7.15, shows that the controller has to try several times before the rotor starts. Notice that the the magnitude of the back-EMF is increased after the third retry. Since back-EMF magnitude is linearly dependent on speed, it seems that the rotor is initially stuck but later released by the multiple tries. This is the expected behaviour in a pump drive, where impurities may get stuck in the bearings and in the air gap.

If the rotor speed is sufficiently low (approximately 1000 RPM), the variations in impeller speed can directly be seen in the pressure measurement. At higher speeds this (more than 1200 RPM), this phenomenon is not so obvious in the pressure measurements as can be seen in Fig. 7.17 done at approximately 1600 RPM.

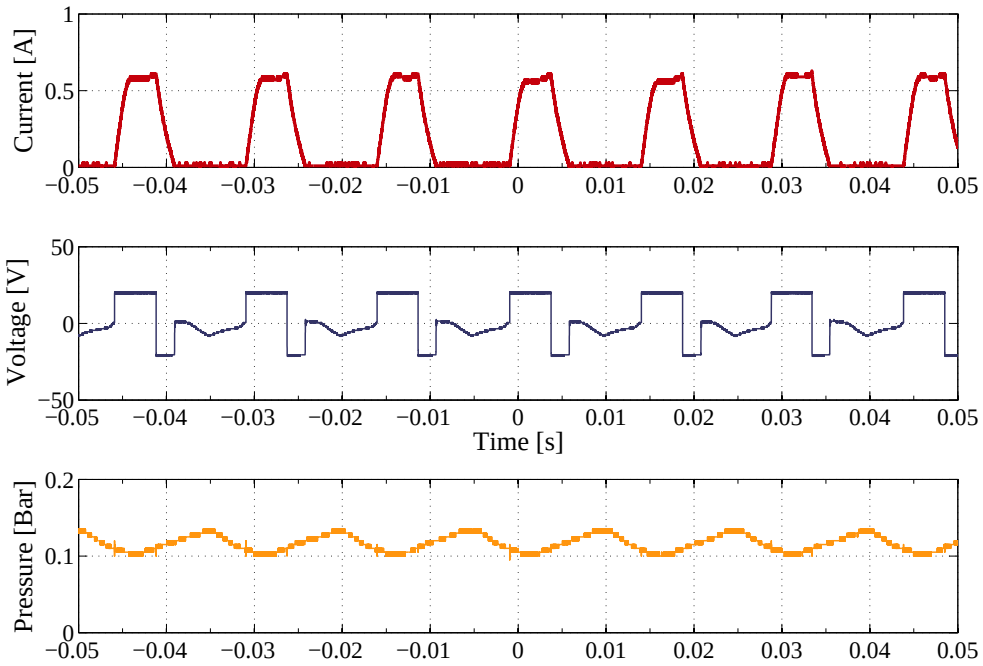

Figure 7.16: The phase current, phase voltage and pressure measurements at approximately 1000 *RPM.*

The actual level of torque produced by the motor can not be reliably be measured with this measurement set-up, since the only flow can be measured correctly. The differential pressure of the pump is not measured only the absolute pressure at a point after the pump and after a turbulent pipe-joint.

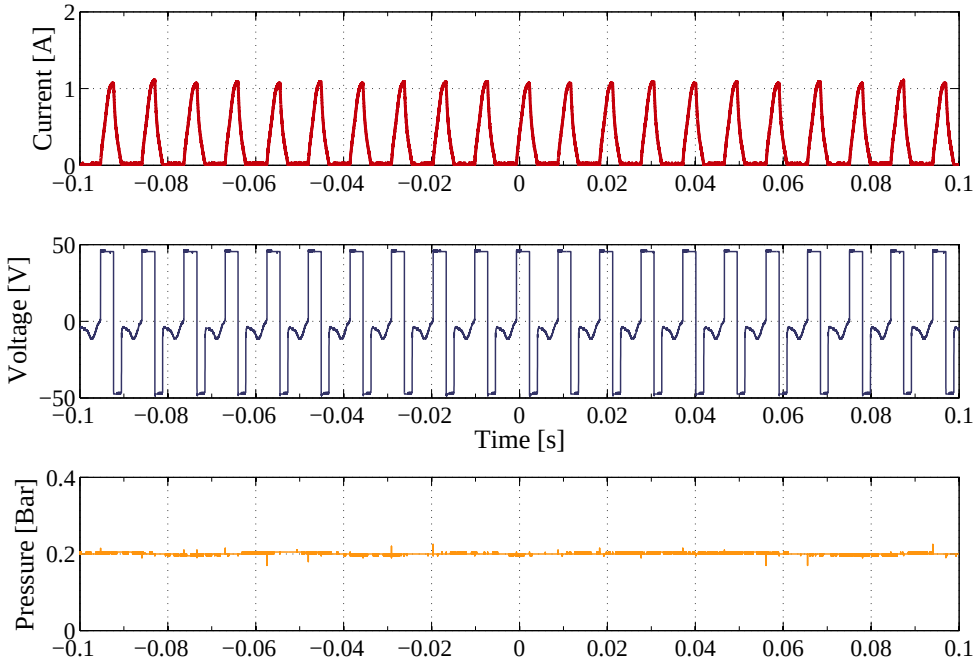

Figure 7.17: The pressure, phase current and phase voltage measured at approximately 1600 *RPM.*

7.4 Discussion

The position sensorless control tests still leaves some challenges regarding the main research question : "'*Is the hybrid switched reluctance motor suitable as a low cost, low power pump motor?*"'. Some of the remaining challenges are:

- The minimum speed for which the speed can be sensed is limited in this set-up since the measured back-EMF is optically isolated from the DSP by a HCPL 7840 optical amplifier(see appendix E for details). The measured differential voltage has to be scaled down to $+/-200\,\mathrm{mV}$ for the optical amplifier and then scaled back for use in the DSP. Removal of the isolation may reduce the magnitude of the noise floor, but the micro controller is then no longer electrically isolated from the power circuits. When the second prototype, the cable length from the inverter to the motor was in excess of $2\,\mathrm{m}$, further limiting the minimum speed for the tests. The long cables may thus also be a cause the retries seen in the sensorless start up of the pump HSRM.

- Reverse rotation was not detected during tests, but reverse rotation should be handled by the sensorless control method. A good time to detect reverse rotation, may be immediately after reaching nominal speed after start-up. If the rotor is rotating opposite the desired direction, the back-EMF shape and zero crossings points may reveal the true direction of the rotor.

7.5 Conclusion

This chapter presented a sensorless method that uses the special features of a hybrid switched reluctance motor that makes the drive especially suited for position sensor less control. The method is suitable for mass produced low cost single direction hybrid switched reluctance motor drives. The method and the motor has the following important features:

1. The motor is designed to provide good start up, by ensuring a wide range of angles, where the motor can be properly started.

2. The permanent magnets in the stator provides a clear signal that can be used for sensing the position, but special care has to be taken to measure the back-EMF properly.

3. The sensorless method does not make detailed and specific assumptions regarding the inverter, the conditions of the magnets, the phase resistance or any varying parameter but only relies on two facts: the load is dissipating energy and the moment of inertia is within a certain range.

4. The position sensorless method only uses one multiplication for the current control, but the sensorless control is handled by additions, shifts and comparisons only. This means that the controller may be implemented also in low cost controllers.

The experimental results shows the possibility of the proposed sensorless control method for fan and pump applications. No parameters needs to be retuned to fit the specific parameters for a given machine in a series produced motor, and the proposed method can thus be used in mass production. This parameter independence was tested here by using the same control implementation for two different motors with different magnetic topology and power range.

Part IV - Conclusion and Future Work

Chapter 8

Conclusion

The research in thesis is regarding the design and control of a single phase hybrid switched reluctance motor intended for a pump drive. The main point is to design a single phase hybrid switched reluctance motor that tries to match high efficiency motors regarding efficiency at a lower cost.

To achieve lower cost several aspects are considered: reduction in sensor requirements by developing a position sensorless control, a lower cost alternative to protect the windings of the motor from water, a motor design that can use simple coils for the windings, uses less copper than an existing induction motor drive, and a motor design that has full torque during start up also when running position sensorless.

8.1 Summary of thesis

The introduction described some requirements for a low power, low volume, low cost pump motor drive.

An introduction of the hybrid switched reluctance motor is presented beginning with an historical overview of the development of these motors. It is argued that NdFeB magnets will continue to increase in price for the foreseeable future and ferrite magnets are an interesting alternative

because of these cost issues.

The question to be answered for the first design was to see, if the hybrid switched reluctance motor could achieve a level of efficiency comparable with the permanent magnet synchronous motor. The peak efficiency of the HSRM is on the same level as previously reported for BLDC and PMSM in the same power range. The first design also introduces pole shaping on the stator to improve starting torque. The designed HSRM introduces a special flux concentrating arrangement of the permanent magnets, that increase the flux density in the airgap without the need for segmented stator laminations. Different flux concentrating arrangements are compared and evaluated. It is described how a too high flux concentration actually may be detrimental to the torque production. The motor uses square bobbins for the coils and has coil insertion slots to simplify the motor manufacture and possibly may simplify recycling. The HSRM was shown to achieve 70 W output power at 79.5% efficiency.

The second motor design tries to reduce the number of permanent magnets needed and fit into a conventional pump housing. Still the motor maintains the coil insertion slots used on the first prototype. The pole shaping is further developed and the positive torque production region of the permanent magnets is extended. Demagnetization for the flux concentration is discussed and considerations regarding the consequences of over current is presented. A protection method for the windings is presented that may reduce cost and losses in a pump drive where the airgap is flooded.

The control chapters describes how the cascaded variable speed drive control is implemented. This includes some considerations regarding how the time variant non linear speed controller can be used as a speed controller.

Since the motor is supposed to be a low cost alternative to a BLDC, then besides manufacturing costs, also component count has to be reduced. A hall effect sensor could have been placed in the motor for position information, but a simple voltage measurement is shown to achieve a similar result. The permanent magnets induce a back electromotoric force (BEMF) in the phase winding that can directly be monitored. The method presented in this chapter is insensitive to variations in DC-link voltage, phase resistance, temperature, variations in inductance, and

the parameters of the inverter. The sensorless method requires only simple operations . It is described how the sensorless control is implemented based on Back-EMF sensing, including how speed is estimated, how to recover from some possible failures of the sensorless method, and a simple start up method. The description includes a description of the implementation and the test results for the position sensorless method.

8.2 Main Contributions

This section describes contributions presented for this thesis, that are believed to be novel.

- A new stator pole shape improves starting, by allowing for a wider range of parking angles even with a higher static friction.

- A new permanent magnet flux concentration configuration, that increases the flux density in the airgap from ferrite permanent magnets which increase the torque density of the motor. The prices for NdFeB dropped since the turn of the millennium, but prices for the raw materials neodymium and dysprosium has increased significantly[15] and will most likely continue to do so. This makes ferrite magnets an interesting alternative to NdFeB. The proposed configuration achieves an airgap flux density using ferrite magnets that is comparable to what can be achieved using bonded Neodymium iron boron magnets (without flux concentration). The flux concentration proposed does not require the segmented stator presented in [36], and thus lowers manufacturing costs.

- The motor achieves a peak efficiency of $79.5\,\%$ at $70\,\mathrm{W}$ output power (including iron losses, copper losses and bearing losses).

- A second motor was developed that fits a conventional pump housing, but still has relatively simple and low cost coils. This simplifies manufacturing compared to a recent motor design presented in [36].

- A time variant speed controller was presented, that allows reliable control of motor with a torque ripple without making the speed control more complicated than for a DC-motor with low torque ripple.

- A softcore processor for AC-motor control was presented during the thesis period[120]. Even though not used for the thesis, it means the work during the PhD-period covers most of a single drive: motor design, control design, position sensorless control, inverter implementation and design of a motor control micro controller.

- A position sensorless method was presented that is suitable for a mass produced low cost drive:

  - Not dependent on detailed parameters of the controlled motor and the parameter variation, except some approximate knowledge about the moment of inertia and average torque for start up.
  - Change of phase resistance due to increased temperature has no impact on the sensed position.
  - Does not need to estimate the strength of the permanent magnets.
  - Requires no knowledge of parameters of the inverter (voltage drop, technology (BJT/IGBT/MOSFET), switching speeds of diodes or transistors, and so on.

- The first prototype single phase hybrid switched reluctance motor uses a smaller amount of motor materials than similar a 3 phase motor presented in [40]. Most notable is that the amount of ferrite permanent magnet material is lower than the amount of NdFeB material used in the 3 phase motor.

8.3 Conclusion

To define what defines a low cost motor depends on what kind of production capability is supposed to manufacture the drive. A low volume, low cost motor may be a different motor from a high volume, low cost motor. For the latter, some materials may become viable simply due to the volume by which the motor is produced. For a low volume motor, it is mandatory to have easy assembly without special tooling. It is also important to consider which materials are used. It may become a concern for low cost motors in the long run that the copper price seems to continue to increase, and the mostly named replacement, aluminium, also has a price/performance that discourages use. Since iron can be recycled indefinitely, and many sources are available for iron it seems that low cost efficient machines should focus on reducing use of copper rather than reducing the use of iron. If there continues to be a high interest in permanent magnet motors/generators, the price of high energy product magnets may continue to increase. The flux concentration presented in this thesis is an alternative method, but needs a larger magnet volume to achieve same flux density. Flux concentration can not make ferrite magnets achieve the same coercitivity (H_c) as NdFeB magnets, but magnets have to be enlarged in the magnetization direction. This means an further increase in volume.

The first motor design presented in this thesis, shows that a single phase hybrid switched reluctance motor (HSRM) can be used as a competitor to the two high performance permanent magnet motors, brushless DC-motor (BLDC) and permanent magnet synchronous motor (PMSM). If the application is a simple uni directional load, such as a fan and a pump, and the dynamic requirements are low, a HSRM can indeed be used without significant loss of efficiency.

The main drawbacks of this motor is still that the torque is not smooth, and the radial force changes magnitude, due to the double saliency structure. This may be the main cause of vibrations and acoustic noise for the HSRM.

Despite not being an optimized design, it performed similar to the chosen benchmark motor: three phase permanent magnet BLDC motor. The first prototype uses significantly smaller amounts of copper compared to the benchmark motor and in particular compared with single

phase induction motors. The sensorless control is possibly simpler than some of the methods used for BLDC motors, and thus there is normally no need to use a hall-sensor for this motor type in fan or pump applications.

All in all, the motor type seem to be a good candidate for some of the same applications that now uses single phase BLDC motors. If the noise from the vibrations can be reduced, then the HSRM may be a suitable candidate for low power, low cost variable speed pump drive for domestic applications. Even if the vibrations can not be reduced, then the HSRM is a suitable candidate for uni-directional applications, such as non-domestic pump applications, fans, and compressors.

Chapter 9

Future Work

There are several topics that are interesting for further study. Some of the topics are listed in the following.

- The stator vibrations are of some concern, since they generate sound in the lower audible range. It would interesting to have a thorough investigation into the source of the vibrations and suggestions for possible solutions.
- It is possible to implement current shaping to improve efficiency. The non-linear and speed dependent relationship between current torque is not optimally used with the simple current control method used in the thesis. A more advanced current control method may further improve the efficiency of the motor at little or no extra cost.
- The hypothesis for the EPDM armour on the windings, is that the main threat to long term water exposure is that heating up will increase the uptake of water, and the subsequent cooling will allow water to travel inwards towards the windings. When sufficient water has travelled inwards it may then attack the polyester and a partial discharge may eventually occur. The partial discharge may lead to an out-gassing from the polyester lacquer. This may eventually force a rupture in the EPDM, and the process may lead to a failure of the winding insulation. The real question is not if the isolation will fail, but rather when. The task is then to ensure this happens no sooner than the service life ends for the product

(approximately 10 years). Preliminary tests for partial discharges, revealed no damage to the windings due to the coating with EPDM on the windings. An interesting test, that should be performed is however a full thermal cycling, possible including thermal shocks.

- The time for motor design was limited and excluded optimization of the design in a systematic way. A parametric design model could be used to optimize the motor based on the principles described in the thesis. A particularly interesting method is proposed in [121] using a grid based search and may be altered for general use , possibly merging with the method presented in [122].

- It proved problematic to measure accurately the performance of a low torque motor, so more measurements of the motor performance should be performed.

- The time variant controllers seems to be stable, but an actual proof of the boundaries of stability would be interesting.

Chapter 10

List of publications

1. Uffe Jakobsen ; Torben N. Matzen, *"Design of a dedicated processor for AC motor control implemented in a low cost FPGA"*, IEEE Power Electronics Specialists Conference, p. 3048-3053, 2008

2. Uffe Jakobsen ; Jin Woo Ahn, *"Non Linear, Time Variant Speed Control of a Single Phase Hybrid Switched Reluctance Motor"*, 31st International Telecommunications Energy Conference, 2009

3. Uffe Jakobsen ; Jin Woo Ahn, *"Efficiency Characteristics of Low Power Hybrid Switched Reluctance Motor"*, Proceedings of the 2009 KIEE Busan Conference. The Korean Institute of Electrical Engineers, 2009

4. Uffe Jakobsen ; Jin Woo Ahn, *"Custom Processor for AC-motor Control Implemented in Spartan 3E FPGA"*, Proceedings of the 2009 KIEE Anual Conference. The Korean Institute of Electrical Engineers, 2009

5. Laszlo Mathe; Uffe Jakobsen ; Peter Omand Rasmussen ; John Kim Pedersen, *" Analysis of the Vibration Spectrum Based on the Input Voltage Spectrum"*, Proceedings of the Energy Conversion Congress and Exposition, ECCE 2009, p. 220-225, 2009

6. Uffe Jakobsen ; Kaiyuan Lu, *"Flux Concentration and Pole Shaping in a Single Phase*

Hybrid Switched Reluctance Motor Drive", Proceeding of the 25th Annual Conference on Applied Power Electronics Conference and Exposition, p. 98-102, 2010

7. Kaiyuan Lu; Uffe Jakobsen; Peter Omand Rasmussen , *"Single-phase Hybrid Switched Reluctance Motor for Low-power Low cost Applications"*, IEEE Transactions on Magnetics, 2011

8. Liang Jianing; Guoqing Xu; Linni Jian, Uffe Jakobsen and Jin-Woo Ahn, *"A Novel Single Phase Hybrid Switched Reluctance Motor Drive System"*, IEEE Energy Conversion Congress & Exposition, 2011

9. P. O. Rasmussen; Gunnar Runólfsson; Thorunn Agusta Thorsdottir; Uffe Jakobsen; Anders Hedeager Pedersen, *"E-core Transverse Flux Machine With Integrated Fault Detection System"*, International Conference on Electrical Machines and Systems, 2011

Bibliography

[1] B. K. Bose, “Power electronics and motor drives - recent progress and perspective,” *IEEE Transactions on Industrial Electronics*, vol. 56, no. 2, pp. 581–588, 2009.

[2] F. Blaabjerg, F. Lungeanu, K. Skaug, and M. Tonnes, “Two-phase induction motor drives: Low-cost topologies for tpim drives in industrial applications,” *IEEE Industry Applications Magazine*, vol. 10, no. 4, pp. 24–32, 2004.

[3] Grundfos, “Energimærkede cirkulationspumper - i en klasse for sig!,” tech. rep., Grundfos, 2006.

[4] H. Kragh, *Modelling, Analysis and Optimisation of Power Electronic Circuits for Low-Cost Drives*. PhD thesis, Aalborg University - Institute of Energy Technology, Aalborg, 2000.

[5] W. Wissmach, *Single-Phase Switched Reluctance Motors - Design and Application*. PhD thesis, École PolyTechnique Fédérale de Lausanne, 2003.

[6] M. Popescu, *Analytical Prediction of The Electromagnetic Torques in Single-phase and Two-phase AC Motors*. PhD thesis, Helsinki University of Technology, 2004.

[7] E. M. H. Kamerbeek, “De eenfasige synchrone motor met permanent magnetische rotor,” Master’s thesis, Technische Hogeschool Eindhoven, 1965.

[8] H. Schemmann, *Theoretische und experimentelle Untersuchungen über das Dynamische verhalten eines Einphasen-Synchronmotors mit Dauermagnetischem Läufer*. PhD thesis, Technisches Hogeschool Eindhoven, 1971.

[9] K. F. Rasmussen, *Efficiency Optimisation of Electric Motors*. PhD thesis, Institute of Energy Technology - Aalborg University, Aalborg, 1995.

[10] S. A. Kurt Haller, "Discussion regarding prices." Verbal communication, 2010.

[11] J. Blas and P. Smith, "Steel prices set to soar," *Financial Times*, vol. 1, p. 1, March 2010.

[12] D. C. Hanselman, *Brushless Permanent Magnet Motor Design*. Magna Physics Publishing, second edition ed., 2003.

[13] P.-W. Han, Y.-D. Chun, J. hak Choi, M.-J. Kim, D.-H. Koo, and J. Lee, "The study to substitute aluminum for copper as a winding material in induction machine," *Conference proceedings of INTELEC 2009*, vol. 1, pp. 1–3, October 2009.

[14] L. M. Exchange, "Copper charts." London Metal Exchange, Electronic, Retrieved data on 16/1/2011, http://www.lme.com/copper_graphs.asp.

[15] Y. Enokido, "Technical trends of neodymium magnets hal method," tech. rep., Dempa Shimbun High-Technology - TDK Corporation, 2010.

[16] M. of Land and R. of the Peoples Republic of China, "Minmetals chamber of commerce: Re prices will continue to rise." Ministry of Land and Resources of the Peoples Republic of China, Online, 30. december 2010, http://www.mlr.gov.cn/kczygl/kcbh/201012/t20101229_808545.htm.

[17] E. Behrmann, "Lynas, arafura shares gain after china rare earth cuts." Bloomberg, Online, 29. December 2010, http://www.bloomberg.com/apps/news?pid=newsarchive&sid=aN6ycgffqNhQ.

[18] X. Yu and F. Rong, "China to raise export taxes of some rare earths to 25% as demand increases." Bloomberg, Online, 16. December 2010, http://www.bloomberg.com/news/2010-12-16/china-will-increase-export-taxes-on-some-rare-earths-to-25-for-next-year.html.

[19] D. J. Kingsnorth, "Rare earths supply: Alternatives to china," conference presentation, Industrial Minerals Company of Australia, 2008.

[20] J. L. Burba, “Global outlook.” Molycorp Minerals LLC., Online, 30. December 2010, http://www.molycorp.com/globaloutlook.asp.

[21] T. Koishikawa, “Shin-etsu announces price increase for rare earth magnets.” Shin-Etsu Chemical Co. Ltd., Online, June 2011, http://www.shinetsu.co.jp/e/news/s20110607.shtml.

[22] T. J. E. Miller, *Brushless Permanent-Magnet and Reluctance Motor Drives*. Oxford: Clarendon Press, ISBN: 0-19-859369-4, 1989.

[23] T. J. E. Miller, *Electronic Control of Switched Reluctance Machines*. Oxford: Newnes, ISBN: 0-7506-50737, 2001.

[24] L. G. Moren, “World patent wo8606891: A reluctance motor,” tech. rep., Electrolux AB, 1986.

[25] R. Krishnan, A. M. Staley, and K. Sitipati, “A novel single-phase switched reluctance motor drive system,” in *The 27th Annual Conference of the IEEE Industrial Electronics Society*, 2001.

[26] R. Sudler and J.-F. Schwab, “German patent de2707684:ein phasen schrittmotor,” 1978.

[27] A. W. Haydon, “Us patent 3256453: Synchronous motors,” 1966.

[28] J. C. R. Smart, “Us patent 5650682: Single phase variable reluctance motor having permanent magnets embedded within a phase winding,” July 1997.

[29] J. C. Compter, “Us patent 4616165: Single phase reluctance motor,” October 1986.

[30] G. E. Horst, “Us patent 5122697: Hybrid single phase variable reluctance motor,” June 1992.

[31] V. Török, “Swedish patent se467852: Elektrisk motor,” 1992.

[32] S. E. Rauch and L. J. Johnson, “Design principles of flux-switch alternators,” *Transactions of the American Institute of Electrical Engineers - Power Apparatus and Systems, Part III*, vol. 74, no. 3, pp. 1261–1268, 1955.

[33] R. Deodhar, S. Andersson, I. Boldea, and T. Miller, "The flux-reversal machine: a new brushless doubly-salient permanent-magnet machine," *IEEE Transactions on Industry Applications*, vol. 33, pp. 925 – 934, 1997.

[34] J. Oyama, T. Higuchi, T. Abe, K. Haraguchi, E. Yamada, and F. Profumo, "Hybrid type novel switched reluctance motor," in *29th Annual IEEE Power Electronics Specialist Conference*, vol. 1, pp. 857 – 863, 1998.

[35] B. Sarlioglu and T. A. Lipo, "Nonlinear modeling and simulation of single phase doubly salient permanent magnet generator," in *Thirty-Third IAS Annual Meeting*, vol. 1, pp. 18 – 26, 1998.

[36] K. Lu, P. Rasmussen, S. Watkins, and F. Blaabjerg, "A new low-cost hybrid switched reluctance motor for adjustable-speed pump applications," in *Conference Record of the 2006 IEEE Industry Applications Conference*, vol. 2, (Tampa), pp. pp. 849–854, 2006.

[37] J. Mayer and O. Wasynczuk, "Analysis and modeling of a singlephase brushless dc motor drive system," *IEEE transactions on Energy Conversion*, vol. 4, pp. pp. 473–479, September 1989.

[38] L. Sun, Q. Feng, and J. Shang, "Drive of single-phase brushless dc motors based on torque analysis," *IEEE transactions on Magnetics*, vol. 43, pp. pp. 46–5, January 2007.

[39] H. R. Andersen, *Motor Drives for Variable-Speed Compressors*. PhD thesis, Aalborg University, 1996.

[40] C. B. Rasmussen, H. R. Andersen, E. Ritchie, and J. K. Pedersen., "Design and efficiency comparison of electric motors for low power variable speed drives with focus on permanent magnet motors," in *Proceedings of the 7th International Conference on Electrical Motors*, pp. 428–432, 1995.

[41] N. Bidstrup, G. Hunnekuhl, H. Heinrich, and T. Andersen, "Classification of circulators," Tech. Rep. 5, Europump, February 2003.

[42] H. E. Hansen, P. Kjerulf-Jensen, and O. B. Stampe, *Varme og klimateknik - Grundbog*. Dansk Selskab for Varme- og Klimateknik - Danvak ApS, 2. udgave ed., 1997.

[43] N. F. Bisgaard, *Opvarming og Ventilation - II. Varmeanlæg*. Akademisk forlag, 2. udgave ed., 1966.

[44] J. Evans, *Pump Ed 101 - Understanding Pumps, Motors, and Their Controls*. www.pumped101.com.

[45] T. Heilmann, *Systemanalyse og simulering*. Holte: Heilmanns Forlag, 2. udgave ed., 2003.

[46] H. Institute, Europump, and the U.S. Department of Energy's (DOE) Industrial Technologies Program, "Variable speed pumping - a guide to successful applications - executive summary," tech. rep., Hydraulic Institute, Europump, and the U.S. Department of Energy's (DOE) Industrial Technologies Program, 2004.

[47] M. Savar, H. Kozmar, and I. Sutlovic, "Improving centrifugal pump efficiency by impeller trimming," *Desalination*, vol. 249, no. 2, pp. 654 – 659, 2009.

[48] J. K. Tangudu, T. M. Jahns, A. M. El-Refaie, and Z. Q. Zhu, "Segragation of torque components in fractional-slot concentrated winding interior pm machines using frozen permeability," in *Proc. of IEEE Energy Conversion Congress and Exposition*, 2009.

[49] N. Bianchi and S. Bolognani, "Magnetic models of saturated interior permanent magnet motors based on finite element analysis," in *Conference Record - IAS Annual Meeting*, vol. 1, pp. 27–34, 1998.

[50] J. A. Walker, D. G. Dorrell, and C. Cosar, "Flux-linkage calculation in permanent-magnet motors using the frozen permeabilities method," *IEEE Transactions on Magnetics*, vol. 41, pp. 3946–3948, 2005.

[51] P. O. Rasmussen, *Design and Advanced Control of Switched Reluctance Motors*. PhD thesis, Aalborg University, Aalborg, 2002.

[52] P. C. Krause, O. Wasynczuk, and S. D. Sudhoff, *Analysis of Electric Machinery and Drive Systems (Second Edition)*. Piscataway: Wiley-IEEE Press, ISBN: 0-471-14326-X, 2002.

[53] H. Vasquez and J. K. Parker, "A new simplified mathematical model for a switched reluctance motor in a variable speed pumping application," *Mechatronics*, vol. 14, pp. 1055–1068, 2004.

[54] J. Liang, *Design and Analysis of Novel Boost Converter for Switched Reluctance Motor Drive*. PhD thesis, Kyunsung University, 2010.

[55] M. Barnes and C. Pollock, "Selecting power electronic converters for single phase switchedreluctance motors," in *Proceedings of the 1998 7th International Conference on Power Electronics and Variable Speed Drives*, no. 456, 1998.

[56] N. Yadlapalli, "Implementation of a novel soft-switching inverter for switched reluctance motor drives," Master's thesis, Virginia Polytechnic Institute and State University, 1999.

[57] P. O. Rasmussen and L. Østergård, "Modeldannelse of effektfaktoroptimeret styring permanent magnet switched reluktans motor anvendt i støvsugerapplikation.," Master's thesis, Institute of Energy Technology - Aalborg University, 1995.

[58] I. Boldea, *Low Cost Sub 100W Brushless Motor Drives*. University Politehnica Timisoara, 2004.

[59] Fairchild, *FCAS50SN60 - Smart Power Module for SRM*. http://www.fairchildsemi.com/ds/FC/FCAS50SN60.pdf, 2006 Seen on the 17/11/2007.

[60] A. Gray, *Electrical Machine Design - The Design and Specification Of Direct And Alternating Current Machinery*. New York: McGraw-Hill, first edition ed., 1913.

[61] J. J. Cathey, *Electric Machines - Analysis and Design Applying Matlab*. New York: McGraw-Hill, 2001.

[62] P. Upadhyay, K. Rajagopal, and B. Singh, "Design of a compact winding for an axial-flux permanent-magnet brushless dc motor used in an electric two-wheeler," *IEEE Transactions on Magnetics*, vol. 40, pp. pp. 2026 – 2028, july 2004.

[63] R. Krishnan, *Switched Reluctance Motor Drives*. Boca Raton: CRC Press, isbn: 0-8493-0838-8, 2001.

[64] A. V. Radun, "Design considerations for the switched reluctance motor," *IEEE Transactions on Industry Applications*, vol. 31, pp. pp. 1079–1087, September/October 1995.

[65] P. Vijayraghavan, *Design of Switched Reluctance Motors and Development of a Universal Controller for Switched Reluctance and Permanent Magnet Brushless DC Motor Drives*. PhD thesis, Virginia Polytechnic Institute and State University, Blacksburg, Virginia, november 2001.

[66] D. C. Meeker, *Finite Element Method Magnetics*. FEMM V4.2 (Mathematica build), April 2009.

[67] A. A. G. Requicha, "Representations for rigid solids: Theory, methods, and systems," *Computing Surveys*, vol. 12, no. 4, pp. 437–464, 1980.

[68] W. Török, W. Wissmach, and R. Schaer, "Self-starting electric brushless motor having permanent magnet and reluctance poles," 2001.

[69] A. T. de Almeida, F. J. T. E. Ferreira, J. Fong, and P. Fonseca, "Eup lot 11 motors," tech. rep., University of Coimbra, 2008.

[70] K. Binns and D. Shimmin, "Relationship between rated torque and size of permanent magnet machines," *IEE Proceedings - Electric Power Applications*, vol. 143, no. 6, pp. 417–422, 1996.

[71] T. Higuchi, J. O. Fiedler, and R. W. D. Doncker, "On the design of a single-phase switched reluctnce motor," in *IEEE International Electric Machines and Drives Conference*, pp. pp. 561–567, 2003.

[72] C. S. Kallesøe, *Fault Detection and Isolation in Centrifugal Pumps*. PhD thesis, Aalborg University, 2005.

[73] J.-H. Kim, E.-W. Lee, and J.-H. Lee, "Design of the starting device installed in the single-phase switched reluctance motor," *IEEE Transactions on Magnetics*, vol. 43, no. 4, p. 1741 – 1744, 2007.

[74] Y. Chen, S. Chen, Z. Zhu, D. Howe, and Y. Ye, "Starting torque of single-phase flux-switching permanent magnet motors," *IEEE Transactions on Magnetics*, vol. 42, no. 10, p. 3416 – 3418, 2006.

[75] A. Boglietti, A. Cavagnino, M. Lazzari, and M. Pastorelli, "Predicting iron losses in soft magnetic materials with arbitrary voltage supply: an engineering approach," *IEEE Transactions on Magnetics*, vol. 39, pp. pp. 981 – 989, March 2003.

[76] V. H. Juha Pyrhönen, Tapani Jokinen, *Design of rotating electrical machines*. John Wiley & Sons, 2008.

[77] Dupont, "Mylar - physical-thermal properties," tech. rep., DuPont Teijin Films, 2003.

[78] J. Rossum, "Fundamentals of metallic corrosion in fresh water," tech. rep., Roscoe Moss Company, 2000.

[79] R. R. Prabu, S. Usa, K. Udayakumar, M. A. Khan, and S. A. Majeed, "Electrical insulation characteristics of silicone and epdm polymeric blends – part i," *IEEE Transactions on Dielectrics and Electrical Insulation*, vol. 14, pp. 1207–1214, 2007.

[80] R. A. Orza, *INVESTIGATION OF PEROXIDE CROSSLINKING OF EPDM RUBBER BY SOLID-STATE NMR*. PhD thesis, Technische Universiteit Eindhoven, 2008.

[81] M. Cheng and W. Chen, "Experimental investigation of the stress–stretch behavior of epdm rubber with loading rate effects," *International Journal of Solids and Structures*, vol. 40, no. 18, pp. 4749–4768, 2003.

[82] A. E. Vlastos and E. Sherif, "Natural ageing of epdm composite insulators," *IEEE Transactions on Power Delivery*, vol. 5, pp. 406–414, 1990.

[83] M. Wilson, "Accelerated aging of epdm and butyl elastomers," tech. rep., Federal Manufacturing & Technologies - United States Department of Energy, 1996.

[84] Y. Xu, Y. He, F. Zeng, and R. Zhang, "Aging in epdm used for outdoor insulation," *IEEE Transactions on Dielectrics and Electrical Insulation*, vol. 6, no. 1, pp. 60–65, 1999.

[85] F. Delor-Jestin, J. Lacoste, N. Barrois-Oudin, C. Cardinet, and J. Lemaire, "Photo-, thermal and natural ageing of ethylene-propylene-diene monomer (epdm) rubber used in automotive applications. influence of carbon black, crosslinking and stabilizing agents," *Polymer Degradation and Stability*, vol. 67, pp. 469–477, 2000.

[86] C. S. Smith and P. F. E. II, "Addendum to material selection guidelines for geothermal energy utilization systems," tech. rep., U. S. Department Of Energy - Geothermal Energy, 1983.

[87] Grundfos, "Grundfos datahÆfte - grundfos alpha pro cirkulationspumper," tech. rep., Grundfos, 2005.

[88] J.-Y. Lim, Y.-C. Jung, S.-Y. Kim, and J.-C. Kim, "Single phase switched reluctance motor for vacuum cleaner," in *IEEE International Symposium on Industrial Electronics Proceedings*, vol. 2, pp. 1393 – 1400, 2001.

[89] Dyson, "Dyson airblade -the fastest, most hygienic hand dryer.." Dyson Inc., Online PDF, Retrieved 22/8-2011, media.dyson.com/downloads/US/airblade/pdf/us_brochure.pdf.

[90] S.-V. Corporation, "Shop-vac industrial." Shop-Vac Corporation, Online PDF, Retrieved 22/8-2011, http://www.shopvac.com/includes/streamPDF.asp?loc=pdf&id=Shop-Vac-Industrial-English.

[91] B. Singh and S. Singh, "State of the art on permanent magnet brushless dc motor drives," *Journal of Power Electronics*, vol. 9, pp. 1–17, 2009.

[92] K. J. Åström and T. Hägglund, *PID Controllers: theory, design and tuning*. Instrument Society of America, 1995.

[93] A. V. Oppenheim, R. W. Schafer, and J. R. Buck, *Discrete-Time Signal Processing*. Prentice Hall, 1999.

[94] P. H. S. Ole Jannerup, *Reguleringsteknik*. Polyteknisk forlag, ISBN: 87-502-0826-8, 2000.

[95] K. Meyberg and P. Vachenauer, *Höhere Mathematik 1*. Berlin: Springer Verlag, 2003.

[96] I. Boldea, “Control issues in adjustable speed drives,” *IEEE Industrial Electronics Magazine*, vol. 2, pp. 32 – 50, 2008.

[97] C. J. Bateman, B. C. Mecrow, A. C. Clothier, P. P. Acarnley, and N. D. Tuftnell, “Sensorless operation of an ultra high-speed switched reluctance machine,” in *2009 IEEE Energy Conversion Congress and Exposition, ECCE 2009*, (San Jose, CA, United states), pp. 3992 – 3999, 2009.

[98] J. Zambada and D. Deb, “Sensorless field oriented control of pmsm motors - an1078,” tech. rep., Microchip, 2010.

[99] Z. Li, Z. Cheng, L. Xu, and T. Li, “Nonlinear fitting by using a neural net algorithm,” *Analytical Chemistry*, vol. 65, no. 4, pp. 393–396, 1993.

[100] C. A. Hudson, N.S.Lobo, and R.Krishnan, “Sensorless control of single switch-based switched reluctance motor drive using neural network,” *IEEE Transactions on Industrial Electronics*, vol. 55, no. 1, pp. 321–329, 2008.

[101] P. Niazi, *Permanent Magnet Assisted Synchronous Reluctance Motor Design and Performance Improvement*. PhD thesis, Texas A&M University, 2005.

[102] L. I. Iepure, G. D. Andreescu, D. Iles, F. Blaabjerg, and I. Boldea, “Novel position and speed estimator for pm single phase brushless d.c. motor drives: Validation with experiments,” in *Proceedings of the 2010 IEEE International Symposium on Industrial Electronics*, pp. 1389–1394, 2010.

[103] D. Swierczynski, *Direct Torque Control with Space Vector Modulation (DTC-SVM) of Inverter-Fed Permanent Magnet Synchronous Motor Drive*. PhD thesis, Institute of Control and Industrial Electronics - Warsaw University of Technology, 2005.

[104] J. Luukko, *Direct Torque Control of Permanent Magnet Synchronous Machines- Analysis and implementation*. Lappeenranta: Lappeenrannan teknillinen korkeakoulu, 2000.

[105] D. Ocen, “Direct torque control for a permanent magnet synchronous motor,” Master’s thesis, Kungliga Tekniska högskolan, set den 23/3/06 2005.

[106] S. B. Ozturk, "Modelling, simulation and analysis of low-cost direct torque control of pmsm using hall-effect sensors," Master's thesis, Texas A&M University, 2005.

[107] O. Wallmark, *Control of Permanent Magnet Synchronous Machines in Automotive Applications*. PhD thesis, Chalmers University of Technology, 2006.

[108] E. Kreyszig, *Advanced Engineering Mathematics*. New York: John Wiley and Sons, ISBN: 0-471-15496-2, 1999.

[109] L. A. de S. Ribeiro, M. C. Harke, and R. D. Lorenz, "Dynamic properties of back-emf based sensorless drives," in *Conference Record of the 2006 IEEE 41st IAS Annual Meeting*, pp. 2026 – 2033, 2006.

[110] T.-H. Kim and M. Ehsani, "Sensorless control of the bldc motors from near-zero to high speeds," *IEEE Transactions on Power Electronics*, vol. 19, no. 6, pp. 1635–1645, 2004.

[111] K.-W. Lee, D.-K. Kim, B.-T. Kim, and B.-I. Kwon, "A novel starting method of the surface permanent-magnet bldc motors without position sensor for reciprocating compressor," *IEEE Transactions on Industry Applications*, vol. 44, no. 1, pp. 85–92, 2008.

[112] K.-Y. Cheng and Y.-Y. Tzou, "Design of a sensorless commutation ic for bldc motors," *IEEE Transactions on Power Electronics*, vol. 18, no. 6, pp. 1365–1375, 2003.

[113] L. Zhang, W. Xiao, and W. Qu, "Sensorless control of bldc motors using an improved low-cost back emf detection method," in *37th IEEE Power Electronics Specialists Conference*, 2006.

[114] P. Grasblum, "Sensorless bldc motor control using mc9s08aw60," tech. rep., Freescale Semiconductor, 2007.

[115] W. Wang, Z. Wu, W. Jin, and J. Ying, "Sensorless control technology for single phase bldcm based on the winding time-sharing method," in *Record of Industrial Electronics Society*, pp. 1732–1736, 2005.

[116] G. Gallegos-Lopez, P. C. Kjaer, and T. J. E. Miller, "A new sensorless method for switched reluctance motor drives," *IEEE Transactions on Industry Applications*, vol. 34, no. 4, pp. 832–840, 1998.

[117] J. F. Wakerly, *Digital Design - Principles and Practices*. Pearson Education International, 2006.

[118] S. Rajagopalan, *Detection of Rotor and Load Faults in Brushless Dc Motors Operating under Stationary and Nonstationary Conditions*. PhD thesis, Georgia Institute of Technology, 2006.

[119] M. D. Negrea, *Electromagnetic Flux Monitoring for Detecting Faults in Electrical Machines*. PhD thesis, Helsinki University of Technology, 2006.

[120] U. Jakobsen and T. Matzen, "Design of a dedicated processor for ac motor control implemented in a low cost fpga," *Power Electronics Specialists Conference*, vol. 1, pp. 3048 – 3053, June 2008.

[121] D. Iles-Klumpner, *Automotive Permanent Magnet Brushless Actuation Technologies*. PhD thesis, University Politehnica Of Timisoara - Faculty Of Electrical Engineering, 2005.

[122] D.-H. Kim, D. Lowther, and J. Sykulski, "Smooth boundary topology optimisation applied to an electrostatic actuator," *IET Science, Measurement and Technology*, vol. 2, no. 6, pp. 427–433, 2008.

[123] K. Ha, C. Lee, J. Kim, R. Krishnan, and S.-G. Oh, "Design and development of low-cost and high-efficiency variable-speed drive system with switched reluctance motor," *Ieee Transactions on Industry Applications*, vol. 43, pp. 703–713, may/june 2007.

[124] Z. Zhou, T. Li, T. Takahashi, and E. Ho, "Implementation of complete ac servo control in a low cost fpga and subsequent assp conversion," in *Nineteenth Annual IEEE Applied Power Electronics Conference and Exposition, 2004. APEC apos;04.*, vol. 1, pp. pp. 565–570, 2004.

[125] Z. Zhou, T. Li, T. Takahashi, and E. Ho, “Fpga realization of a high-performance servo controller for pmsm,” in *Nineteenth Annual IEEE Applied Power Electronics Conference and Exposition, 2004. APEC ’04.*, vol. 3, pp. pp. 1604–1609, 2004.

[126] C.-W. C. Ying-Shieh Rung, Pin-Ging Huang, “Development of a sopc for pmsm drives,” in *Circuits and Systems, 2004. MWSCAS ’04. The 2004 47th Midwest Symposium on, IEEE*, no. 47, 2004.

[127] Y.-S. Kung, C.-S. Chen, K.-I. Wong, and M.-H. Tsai, “Development of a fpga-based control ic for pmsm drive with adaptive fuzzy control,” in *31st Annual Conference of IEEE Industrial Electronics Society, IECON 2005.*, pp. pp. 1544–1549, 2005.

[128] K. J. A. ström and B. Wittenmark, *Computer-Controlled Systems*. Upper Saddle River, NJ, USA: Prentice Hall, ISBN: 0-471-84910-3, 1990.

[129] R. Andraka, “A survey of cordic algorithms for fpga based computers,” in *Proceedings of the Sixth ACM/SIGDA International Symposium on Field-Programmable Gate Arrays (FPGA ’98)*, no. 6, 1998.

[130] B. Parhami, *Computer Arithmetic - Algorithms and Hardware Designs*. New York, USA: Oxford University Press, ISBN: 0-471-84910-3, 2000.

Chapter 11

Nomenclature

β_s	Stator pole arc
β_{rs}	Arc of the saturated part of the rotor
β_{ru}	Arc of the unsaturated part of the rotor
Δi	Current difference between two current control updates
Δt	Time between two control updates
ε	Result of error calculation
ε'	Result of simplified error calculation
$\hat{U}_{back-emf}$	Peak back EMF at rotor speed of $\omega_{nominal}$
ω	Motor speed in rad/s
ω_{min}	Minimum speed where back-EMF can be reliably detected
$\omega_{nominal}$	Nominal rotor speed
ω_{ref}	Reference speed
Ψ	Phase fluxlinkage
Ψ_0	Initial fluxlinkage/permanent magnet fluxlinkage
Ψ_{bias}	Unaligned bias flux linkage at zero current
$\Psi_{PM}(\theta)$	Permanent magnet fluxlinkage
τ_{em}	Torque generated by the HSRM

$\tau_{friction}$	Viscous friction torque
τ_{load}	Torque load
θ	Rotor angle
θ_a	Aligned rotor angle
θ_u	Unaligned rotor angle
$\tilde{\omega}$	Average speed
$\tilde{u}$	Average voltage vector
B	Coefficient for viscous friction
B_{fric}	Coefficient of frictional load (fan/pump)
$counter_{on}$	Number of switching frequency periods where inverter is fluxing HSRM
D_{duty}	PWM duty cycle
f_s	Switching frequency
H_c	Permanent magnet coercivity
i	Phase current
i_{max}	Maximum current
i_{ref}	Current reference
int	Integrator controller output
J	Moment of intertia
k_i	Integral gain
k_p	Proportional gain
L	Phase inductance

n	Motor speed in RPM
P_r	Number of rotor poles
P_s	Number of stator poles
$prop$	Proportional controller output
$prop'$	Output of time variant proportional controller
R	Phase resistance
t_1	Time for start of a stroke
t_2	Time for end of a stroke
u	Phase voltage
W_Ψ	Energy stored in the magnetic flux
W_{cap}	Energy in the DC-link capacitor
W_{co}	Co-energy
W_{cu}	Energy lost due to coil winding resistance
W_{el}	Electrical energy from the supply
W_{Fe}	Iron loss energy
$W_{field}(\Psi, \theta)$	Field energy
W_{fric}	Frictional energy losses
W_J	Energy stored in the rotational mass
W_m	energy supplied to the motor load.
W_{supply}	Energy from the supply

Part V - Appendix

Appendix A

Parameters for first prototype

Table A.1: Machine parameters

Output power (measured)	70 W
Outer stator length	96.4 mm
Airgap	0.4 mm
Rotor radius	24.2 mm
Shaft diameter	10mm
Stack length	30 mm
Lamination thickness	0.35 mm
Silicon iron weight	1.153 kg
Permanent magnet volume	$17.54\,\mu\text{m}^3$
Permanent magnet weight	94.7 g
Permanent magnet quality	C5
Phase resistance at DC	$4.2\,\Omega$
Number of turns	300
Wire	3×0.355 mm
Copper weight	185 g

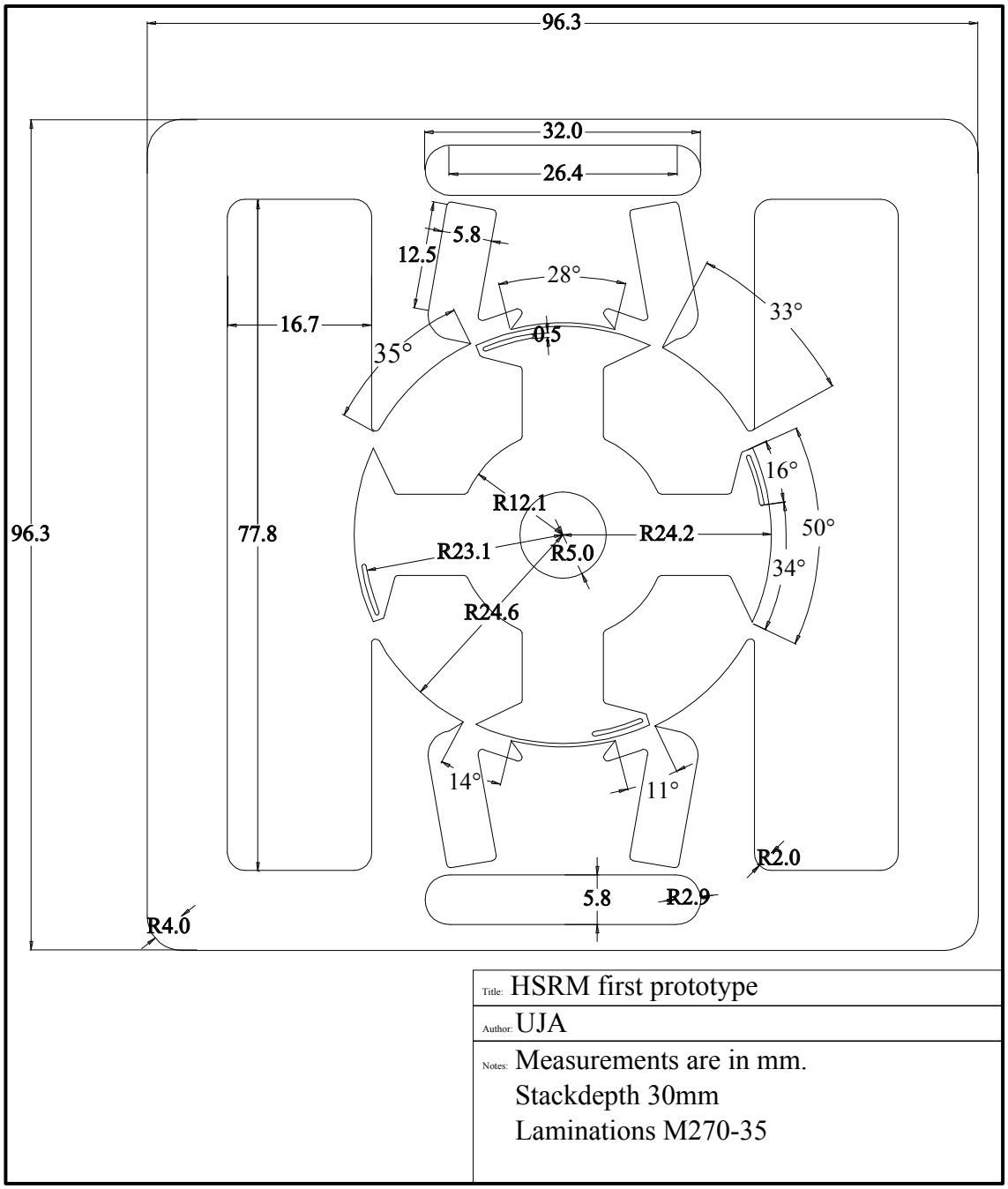

Figure A.1: Key measurements for first prototype

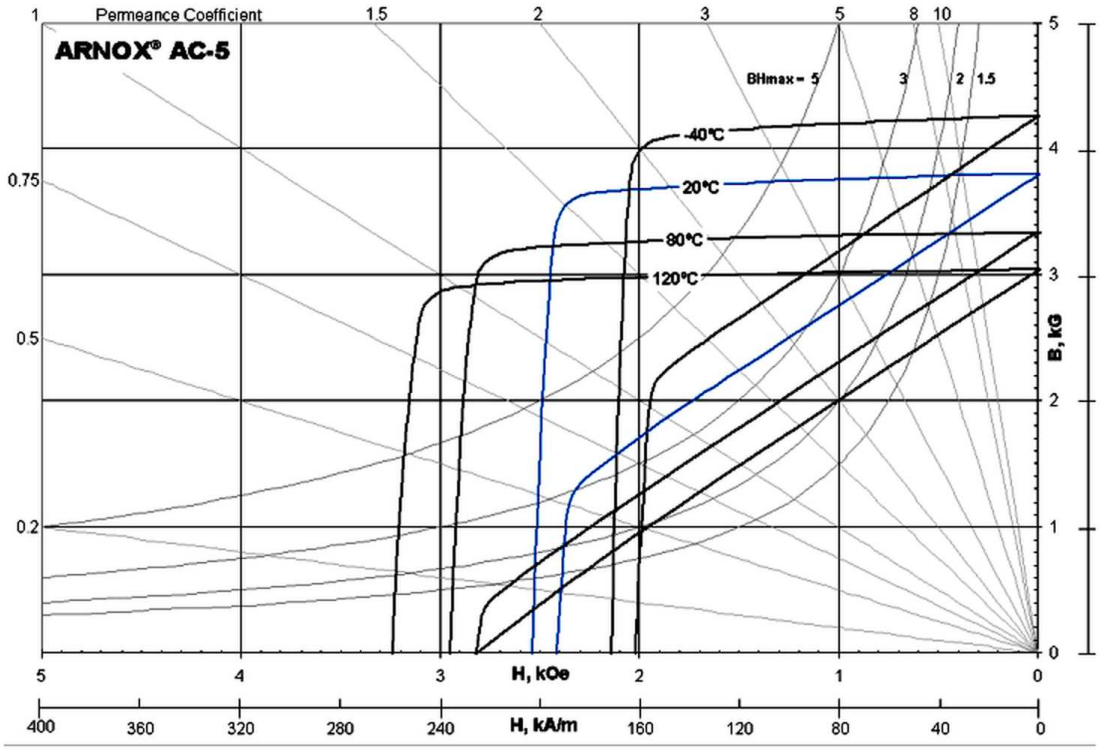

Figure A.2: Data for C5 magnets

Table A.3: Magnet parameters for C5

$\mathbf{B_r}$	$0.380\,\mathrm{T}$
$\mathbf{H_c}$	$191\,\mathrm{kAm^{-1}}$
Intrinsic coercive field $\mathbf{H_{ci}}$	$203\,\mathrm{kAm^{-1}}$
Maximum energy product $\mathbf{BH_{max}}$	$27.1\,\mathrm{kJm^{-3}}$

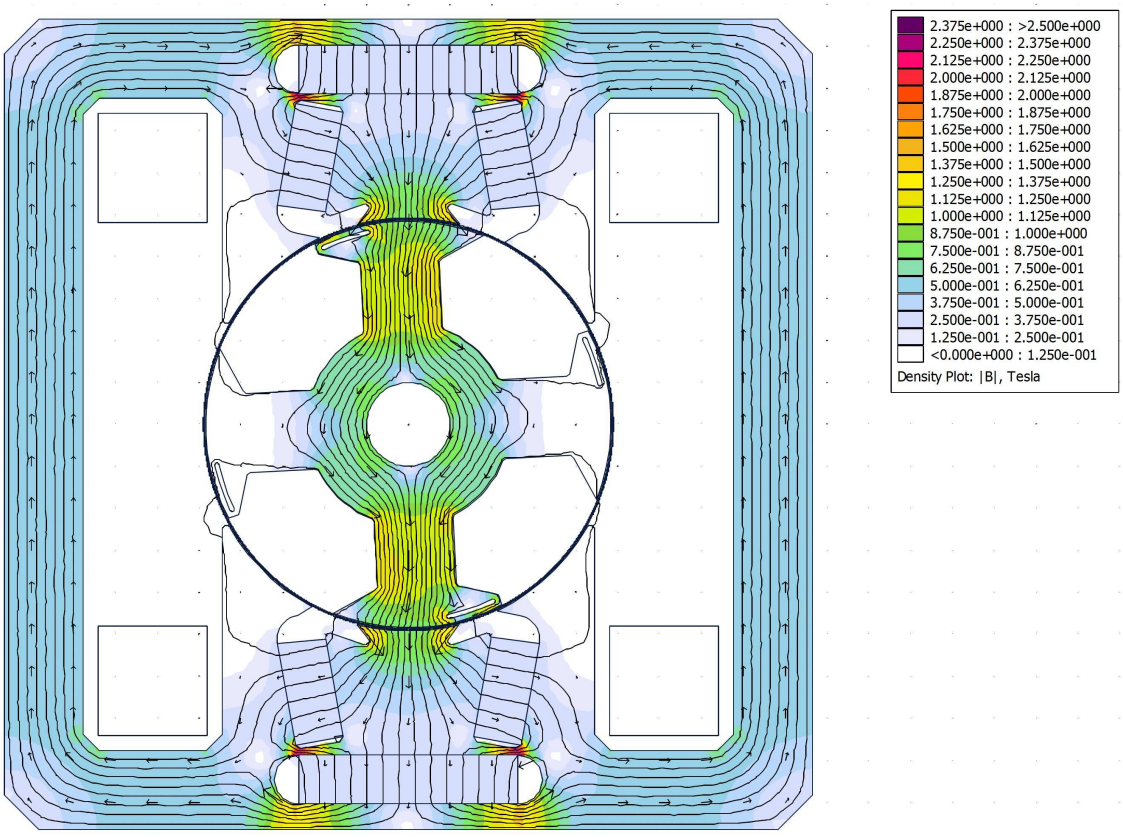

Figure A.3: First prototype motor with rotor rotated to 3 *degrees with* 0 *A phase current*

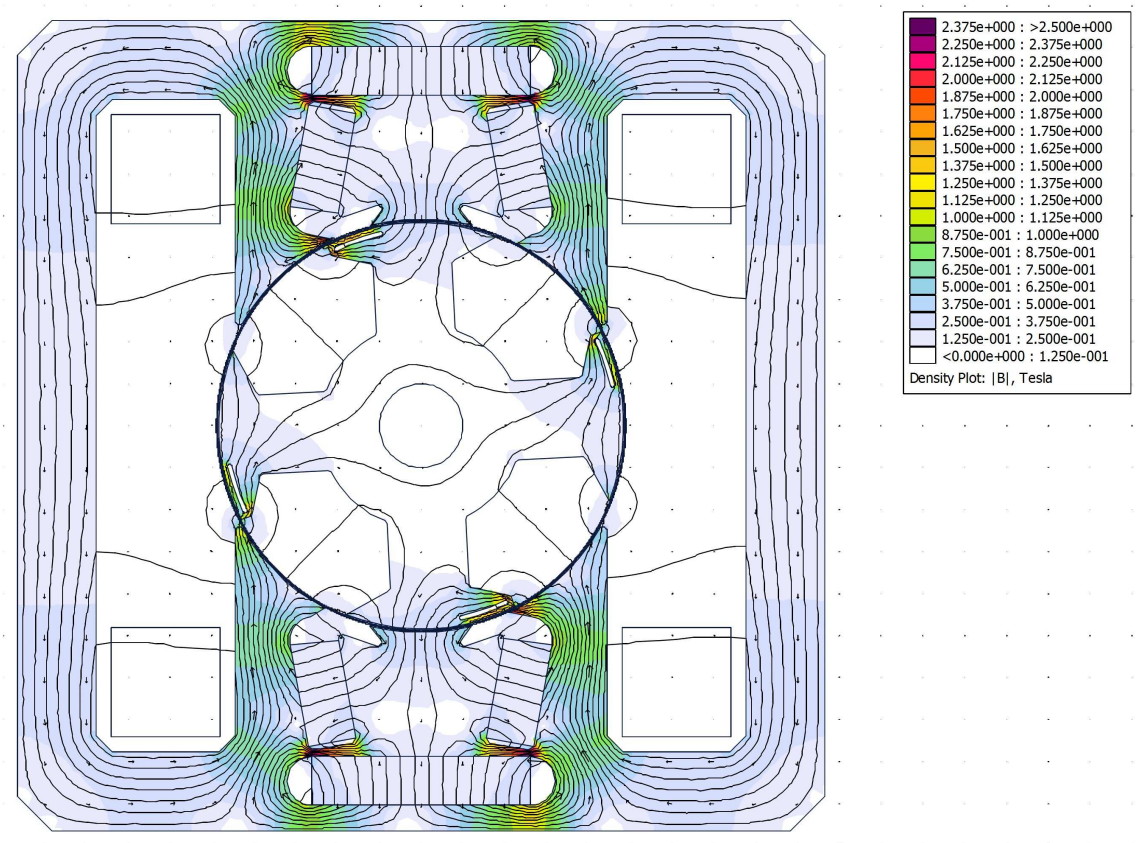

Figure A.4: First prototype motor with rotor rotated to 3 *degrees with* 4 *A phase current*

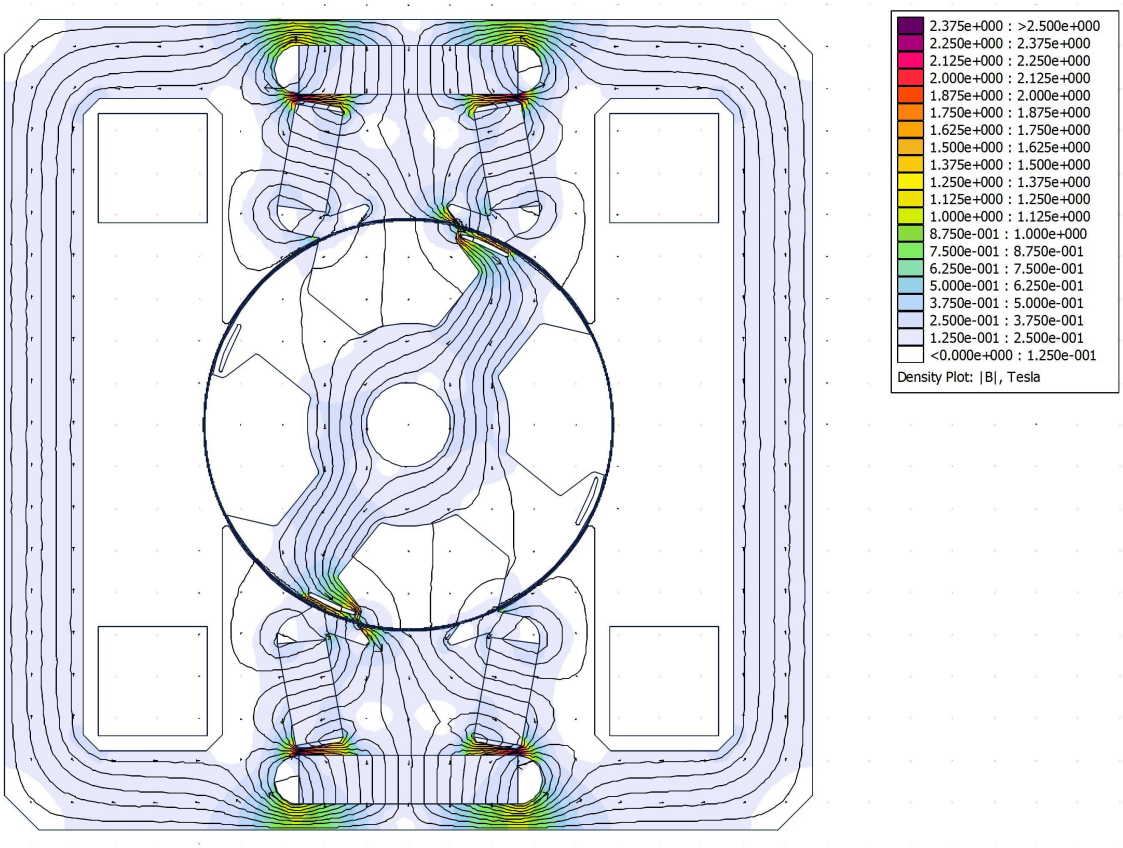

Figure A.5: First prototype motor with rotor rotated to 48 *degrees with* 0 *A phase current*

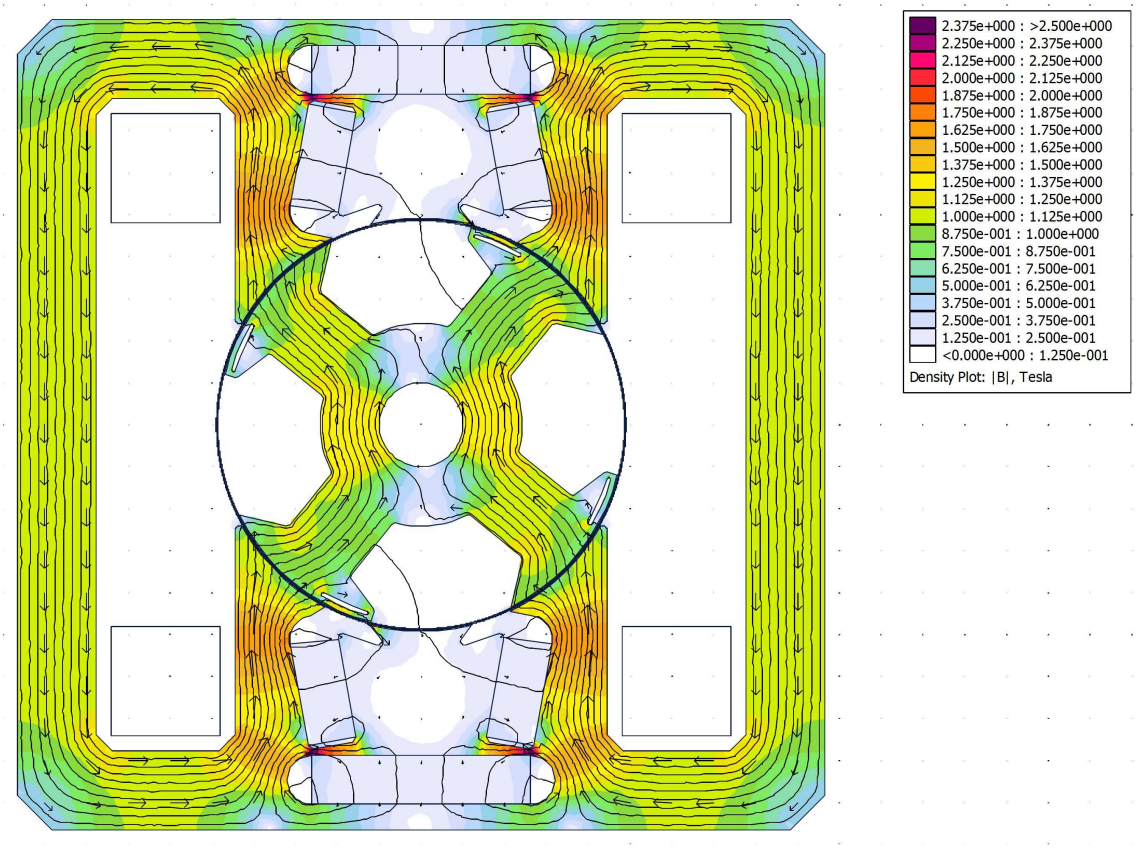

Figure A.6: First prototype motor with rotor rotated to 48 *degrees with* 4 *A phase current*

Appendix B

Parameters for second prototype

Table B.1: Machine parameters

Output power	30 W
Outer stator length	80 mm
Airgap	0.4 mm
Rotor radius	16.8 mm
Shaft diameter	12mm
Stacklength	25 mm
Lamination thickness	0.35 mm
Iron weight	0.442 kg
Permanent magnet volume	$7.93\,\mu\mathrm{m}^3$
Permanent magnet weight (effective)	42.822 g
Permanent magnet quality	C8
Phase resistance at DC	$6.1\,\Omega$
Number of turns	400
Wire	2×0.355 mm
Copper weight	117 g

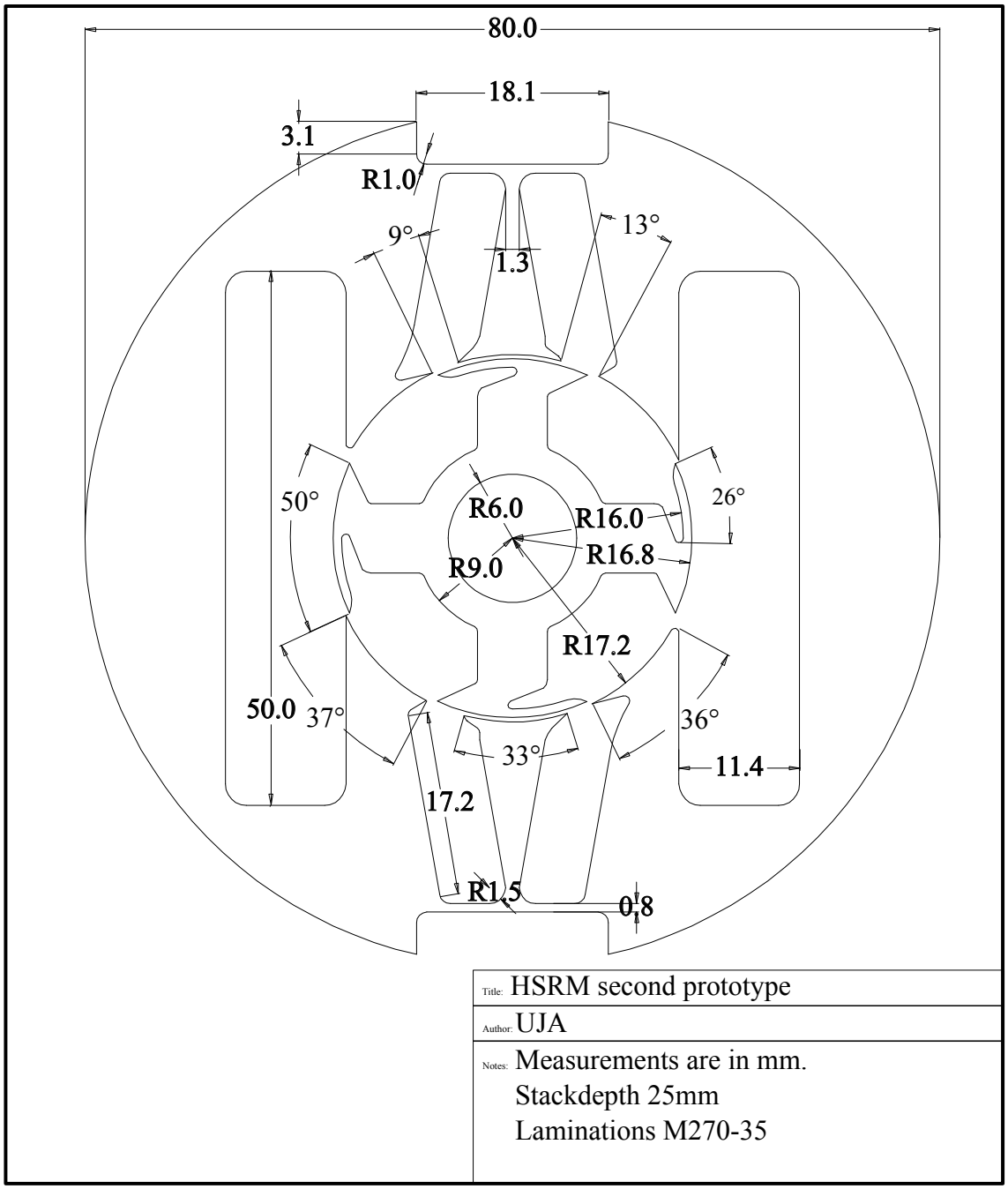

Figure B.1: Key measurements for first prototype

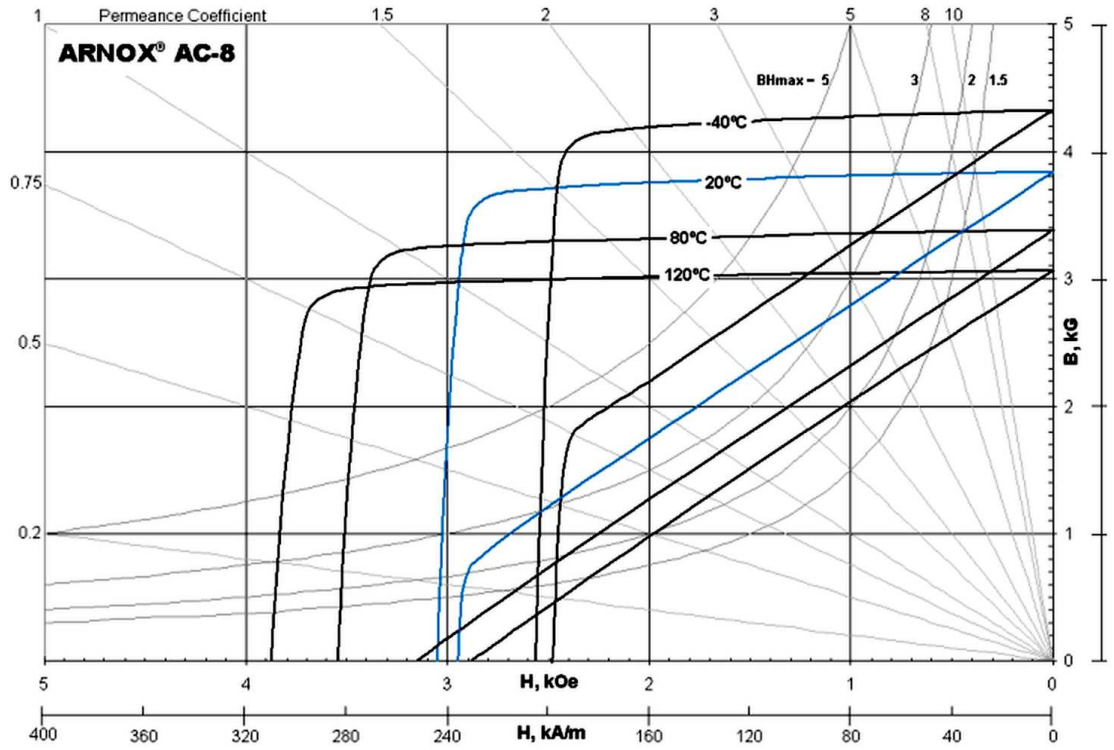

Figure B.2: Data for C5 magnets

Table B.3: Magnet parameters for C8

$\mathbf{B_r}$	$0.385\,\mathrm{T}$
$\mathbf{H_c}$	$235\,\mathrm{kAm^{-1}}$
Intrinsic coercive field $\mathbf{H_{ci}}$	$243\,\mathrm{kAm^{-1}}$
Maximum energy product $\mathbf{BH_{max}}$	$27.9\,\mathrm{kJm^{-3}}$

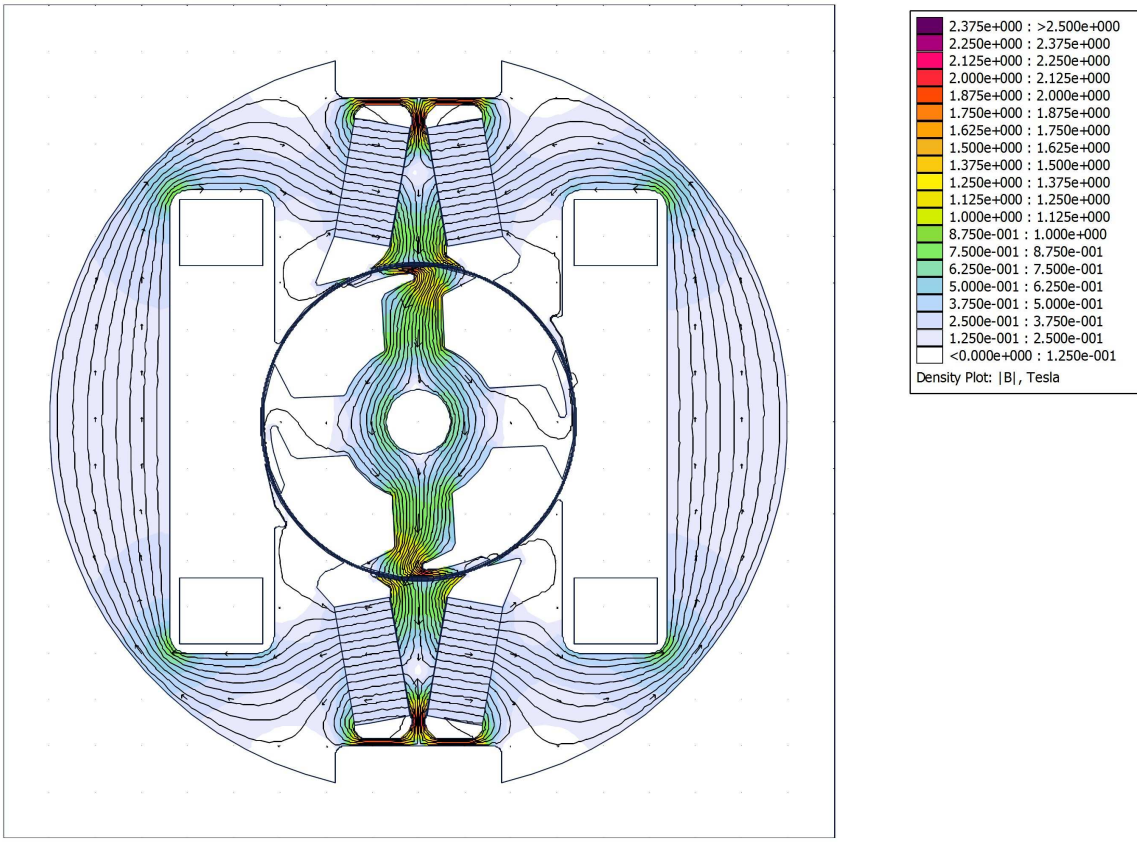

Figure B.3: First prototype motor with rotor rotated to 3 *degrees with* 0 *A phase current*

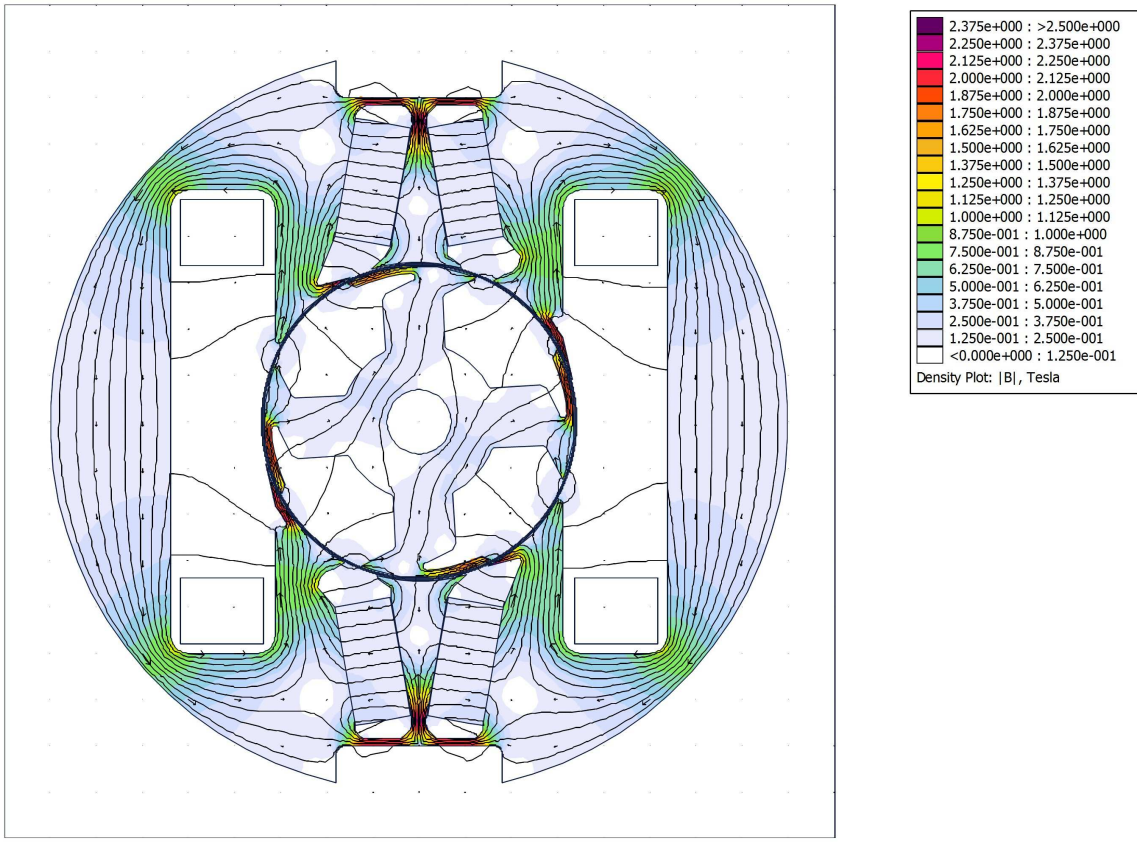

Figure B.4: First prototype motor with rotor rotated to 3 *degrees with* 3 *A phase current*

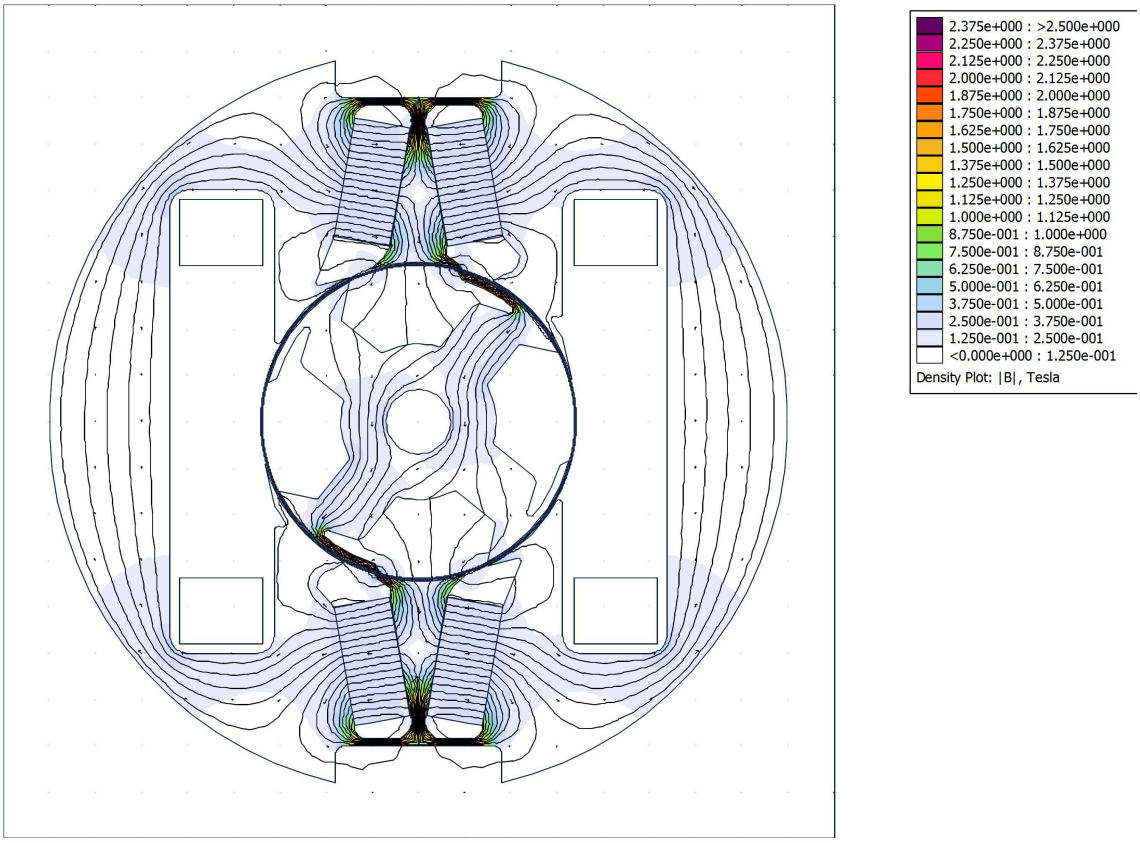

Figure B.5: First prototype motor with rotor rotated to 51 *degrees with* 0 *A phase current*

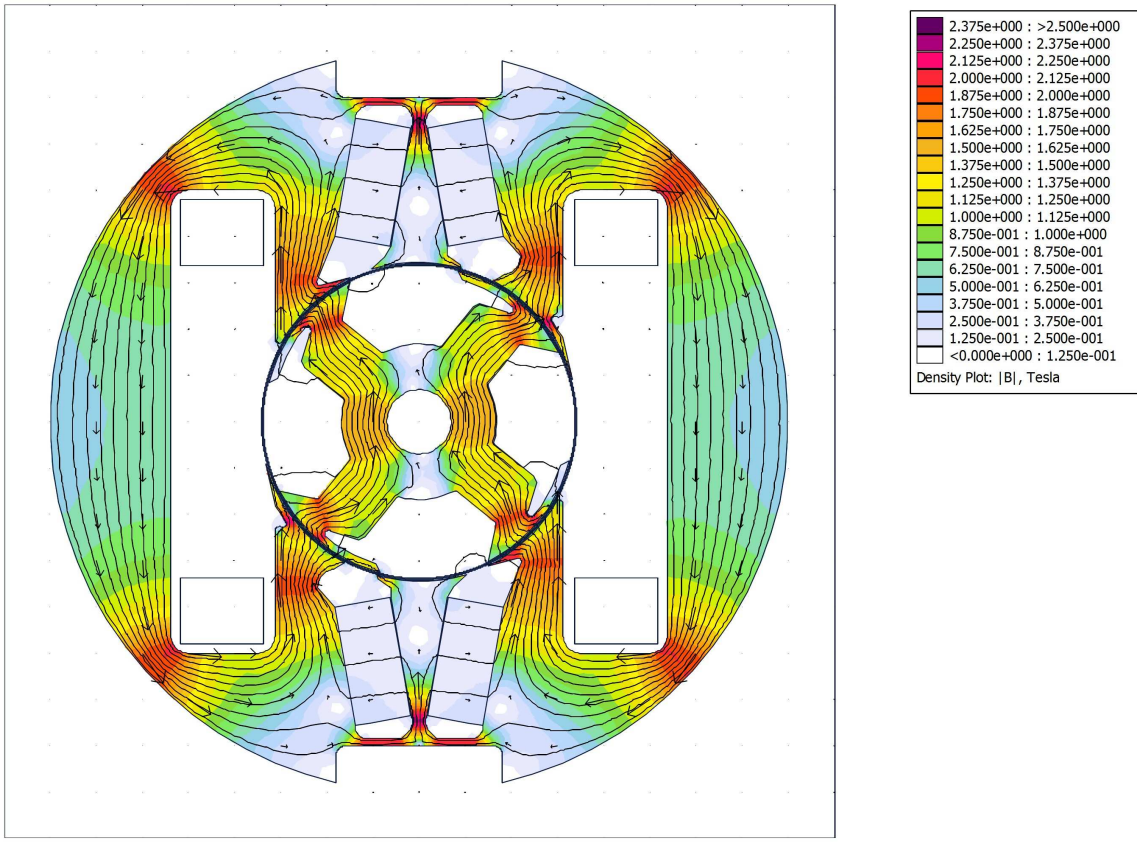

Figure B.6: First prototype motor with rotor rotated to 51 *degrees with* 3 *A phase current*

Appendix C

Simulink model

The hybrid switched reluctance motor (HSRM) is simulated as three interconnected subsystems: a mechanical subsystem, a control subsystem, and an electrical subsystem as shown on Fig. C.1. The HSRM model is based on the equations described in section 3.2.

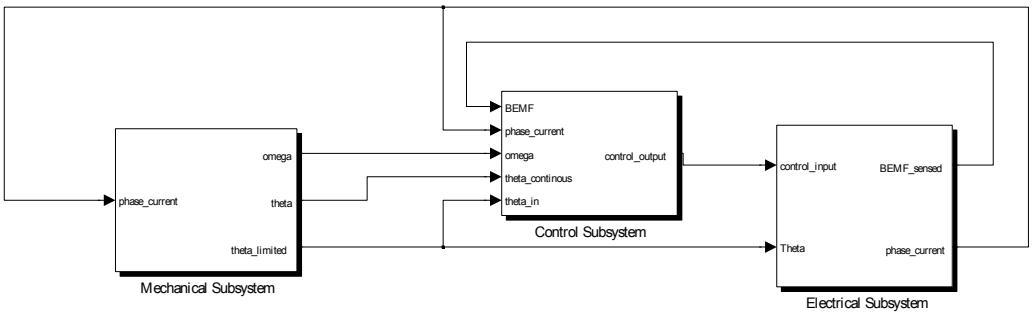

Figure C.1: The combined system is composed of three components

The mechanical subsystem, shown in Fig. C.2, calculates the rotor speed and rotor angle based on the HSRM phase current and rotor angle. The friction simulation includes a non linear stiction model and a simple friction model. The HSRM phase current is used together with the rotor angle as index into a torque look up table based on the finite element model of the HSRM. Since the finite element model only has a finite number of points, linear interpolation is used between points.

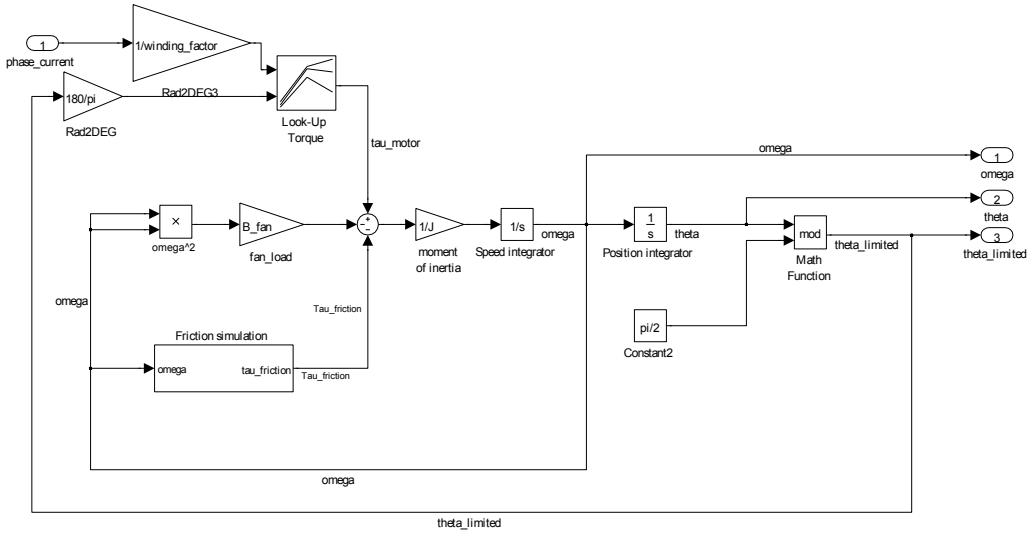

Figure C.2: The mechanical systems also handles the fan load, and calculation of friction (stiction and viscous friction).

The control subsystem shown in Fig. C.3 has two main sub systems: a speed controller and a current controller. The current controller is for the position sensorless control extended into the position sensorless state-machine described in chapter 7.

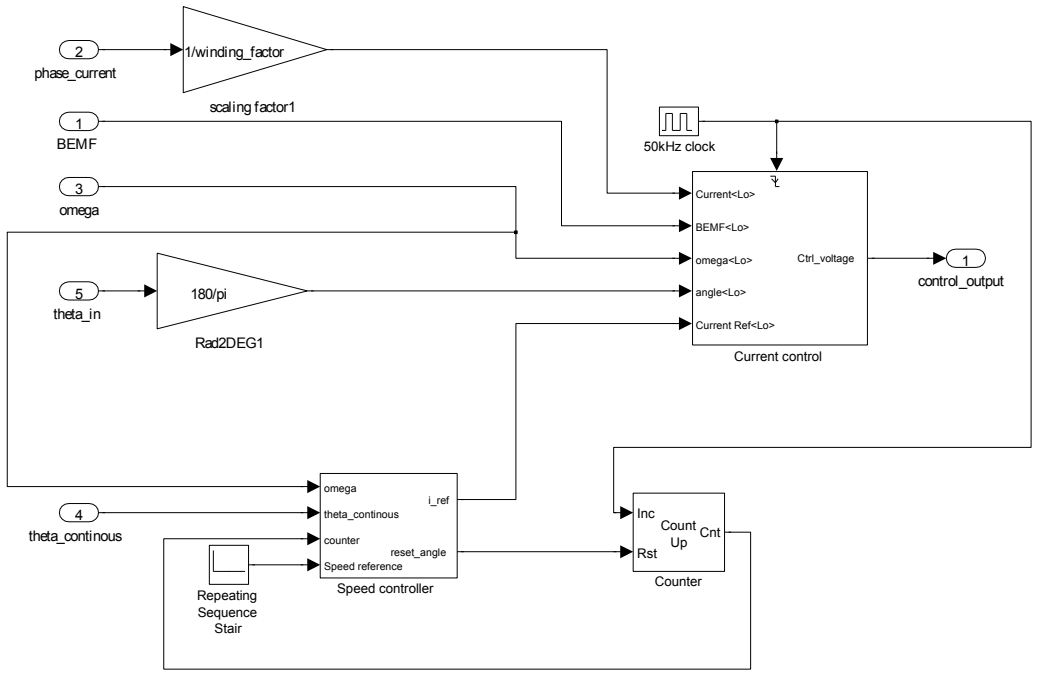

Figure C.3: The control subsystem is made of two main subsystems: the speed controller and the current controller.

The actual controllers are implemented as triggered subsystems with embedded m-scripts. The embedded m-scripts does not emit a properly defined output until they are initialized. There is unfortunately no way of defining the initial state when used together with triggered subsystems. This means that the initial control actions made by the controllers differ from the initial control actions made by the actual controllers in the microcontroller. This had an impact mostly on the position sensorless controller. The position sensorless controller is depending on the initial stroke to reach sufficient speed for proper sensing of the back-EMF to synchronize with the rotor position. This also means that the initial behaviour of the simulation differs from he experimental results, but the position sensorless control method is robust towards these errors as described in the chapter regarding position sensorless control.

The speed controller calculates the current reference used by the current controller. The speed controller is updated synchronized with the rotor angle as shown in Fig C.4. The continuous angle is compared against a trigger angle to generate a trigger signal that triggers an update of the speed controller. The separation is done to emulate the behaviour of the implementation in the microcontroller. In the microcontroller is the speed controller implemented in the "main" loop, and the current controller as a timer interrupt synchronized with the switching frequency. The current controller or the position sensorless controller signals the speed controller when it is time for an update of the speed controller. When running with a position sensor, a shaft encoder is used to measure the rotor position used as a trigger. When running position sensorless the subsystem is trigger by the position sensorless controller. When running position sensorless the current controller is replaced with the position sensorless controller, since the position sensorless controller also handles current control.

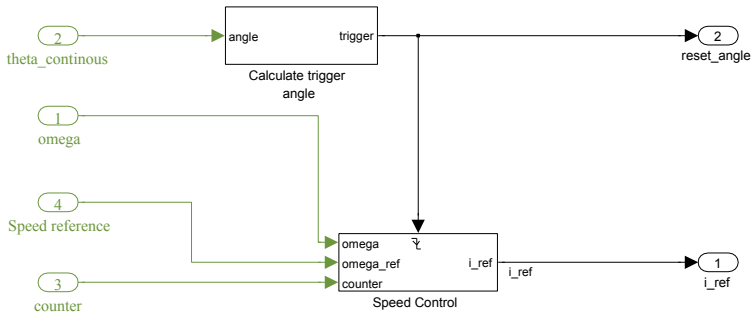

Figure C.4: The speed controller

The electrical subsystems contains a simple inverter model that calculates the voltage applied to the HSRM. The electrical subsystem uses look up tables from the finite element simulation, where the permanent magnet flux linkage is treated separately from the flux linkage generated by the coils. The winding factor is used to scale the current

The inverter assumes that the inverter is run with hard switching and only considers an average voltage model of the inverter. The inverter uses the phase current together with the control signals to determine if the applied DC-link voltage is positive or negative.

The back EMF calculation shown in Fig. C.7, uses the control signals to calculate the differential voltage across the HSRM terminals. The back-EMF can only be measured directly, when there

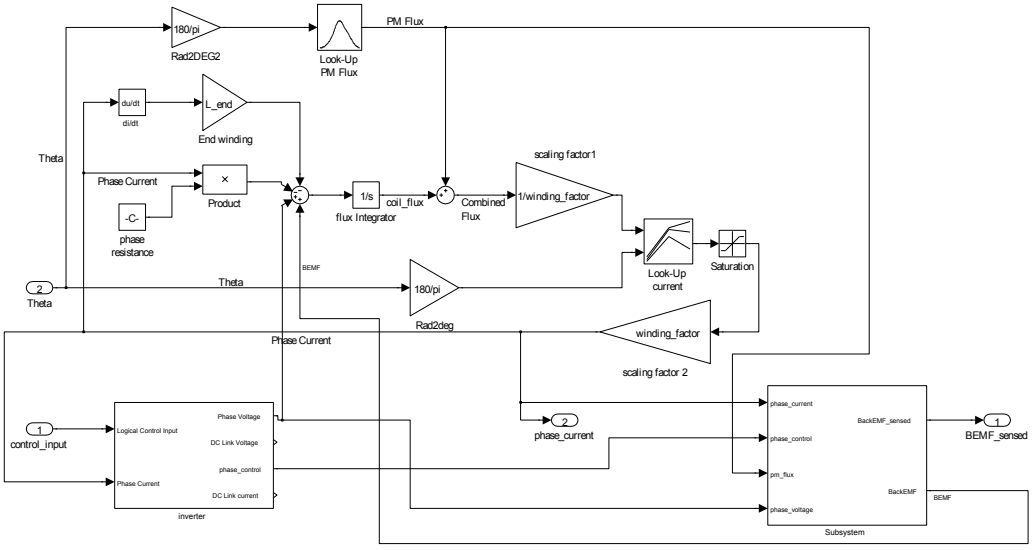

Figure C.5: The eletrical system also uses two subsystems: one subsystem to calculate back EMF and one subsystem to handle inverter dynamics

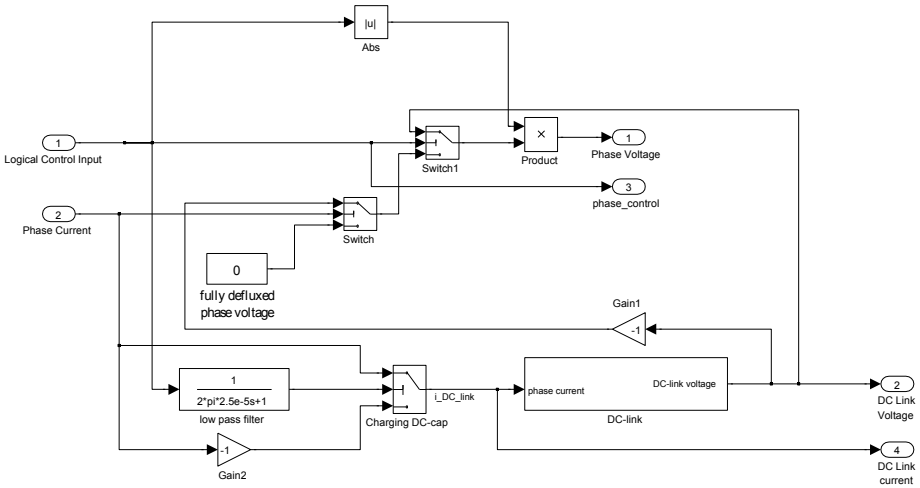

Figure C.6: The inverter subsystem accepts dutycycles between -1 to +1 and uses this to generate appropriate average applied phase voltage

is no phase current. The back-EMF calculation does not handle the common mode rejection rate of the measurement circuit.

DC-link dynamics is simulated with a power sim model of the capacitor as shown in Fig. C.8. The DC-link simulation only simulates the major fluxing and defluxing of the capacitor, and does not handle the switching dynamics when the inverter is operated with either hard-switching PWM or soft-switching.

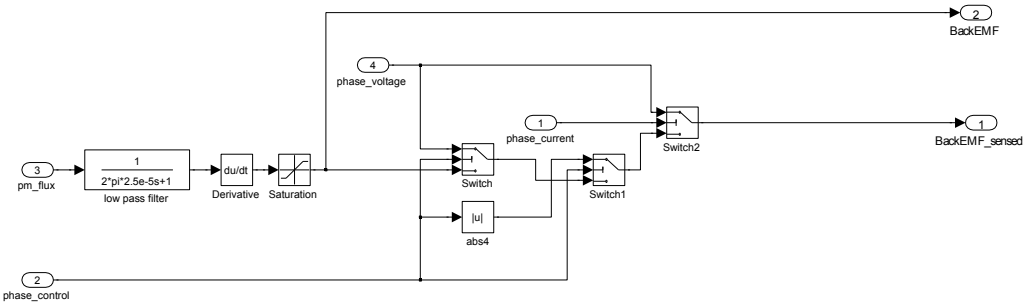

Figure C.7: The back EMF is calculated by using the a differential of a lowpass filtered value of the BEMF. It also handles the applied phase voltage, to simulate the disturbing effect of the inverter.

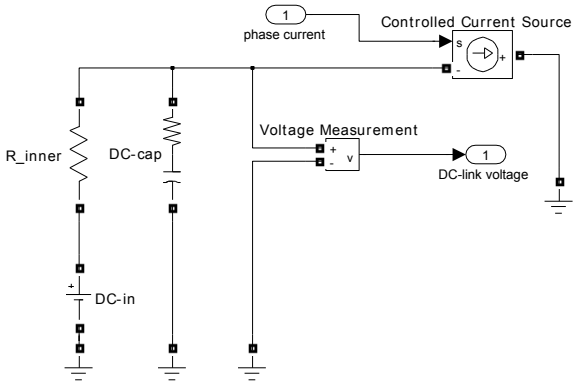

Figure C.8: DC-link

Appendix D

Laboratory set-ups

Introduction

To verify the performance of the motor designs and the control methods various measurements the motors have been made. Static performance measurements were made for the first prototype motor (flux linkage and torque) to validate the performance of the HSRM design. The dynamic measurements included efficiency measurement and performance measurements of the implemented controllers.

Static measurements

The static parameters of torque and flux linkage of the hybrid switched reluctance motor was measured in two static test set-ups.

Torque measurement

The torque was measured using a strain gauge, a stepper motor with an integrated gearbox. a strain gauge measurement amplifier with a display and serial port, a balanced aluminium beam,

some standard weights, and a DC power supply. The strain gauge amplifiers readings were calibrated using the aluminium beam and the standard weights. The standard gravitational acceleration for Denmark is $g = 9.82\,\mathrm{m/s^2}$ and is used in $\tau = m_{weight} \cdot g \cdot l$, where m_{weight} is a calibration weight, τ is the torque, and l is the distance from the centre where the weights are placed (here it is $0.5\,\mathrm{m}$). The motor is fitted to the strain gauge instead of the balanced aluminium beam and using a DC-supply. The current is adjusted and using the stepper motor the rotor angle is chosen. The torque is recorded for the torque envelope using the setup shown in Fig. D.2.

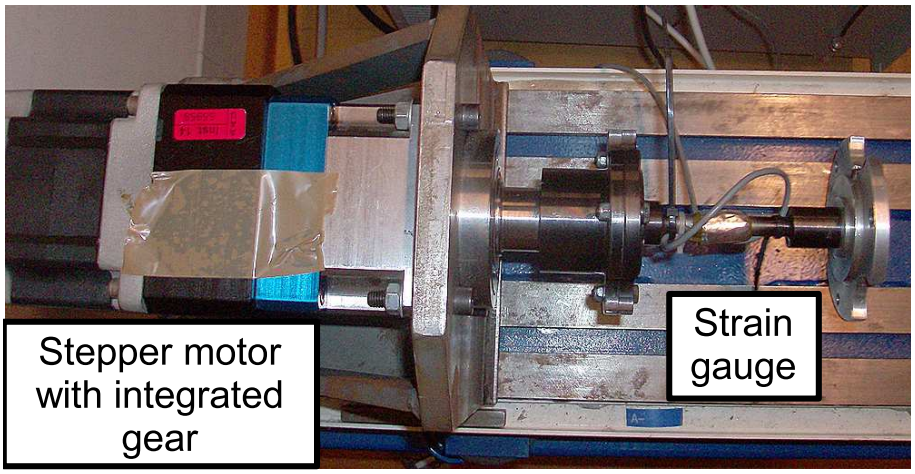

Figure D.1: The strain gage is connected to an amplifier that samples and reads out the calculated torque. The stepper motor holds the HSRM rotor at a desired angle (θ) for both the static torque test and the flux linkage test.

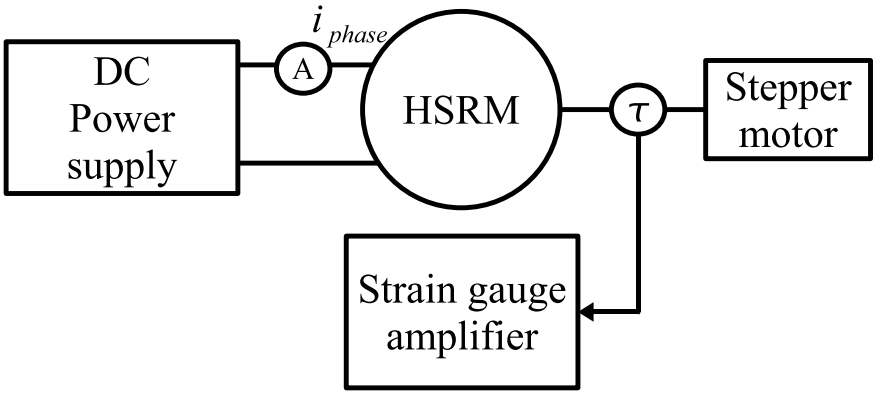

Figure D.2: The static torque measurement set-up

Flux linkage measurement

Flux linkage is measured for minimum and maximum reluctance positions, with a Chroma programmable power supply, an oscilloscope and the stepper motor fixing the rotor at angle (θ). The power supply is programmed to give a voltage step, where current and voltage is recorded on the oscilloscope. The desired magnitude of the voltage step is given by $U_{step} = R_{phase} \cdot I_{desired}$, where U_{step} is the desired voltage step magnitude, R_{phase} is the phase resistance, and $I_{desired}$ is the desired steady state current magnitude. The transient voltage (u) and current (i) is recorded and the flux linkage ($\Psi(i,\theta)$) is calculated based on: $\Psi = \int u - R \cdot i dt$.

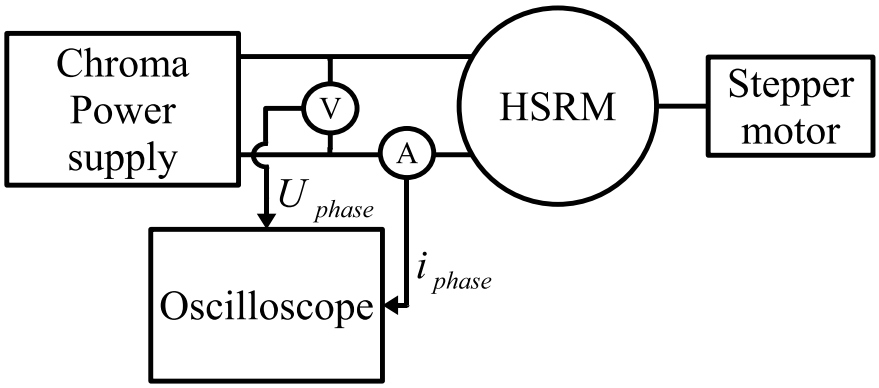

Figure D.3: The test set-up for flux linkage tests

Efficiency measurements

A fan from an induction motor was used a simple to use load to test the performance of the first prototype. The chosen motor fan dissipates energy, as a function of the rotational speed as it is shown in Fig. D.4 using the experimental set-up shown in Fig. D.5.

The DC-motor is run at specific speeds with and without the fan, while the input power and phase current is measured. The fan losses are calculated based on a DC-motor model as described in [123].

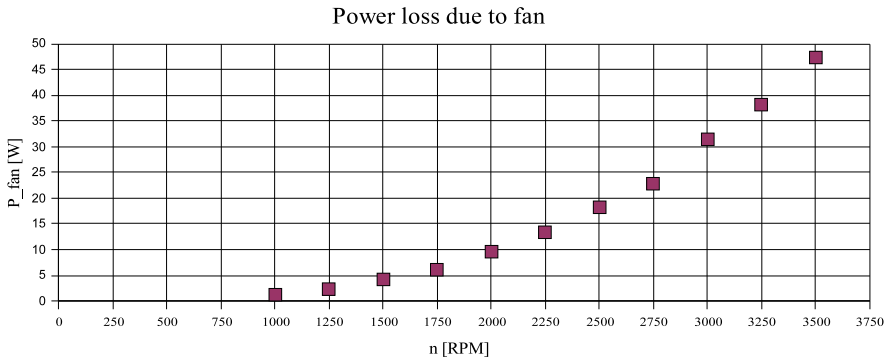

Figure D.4

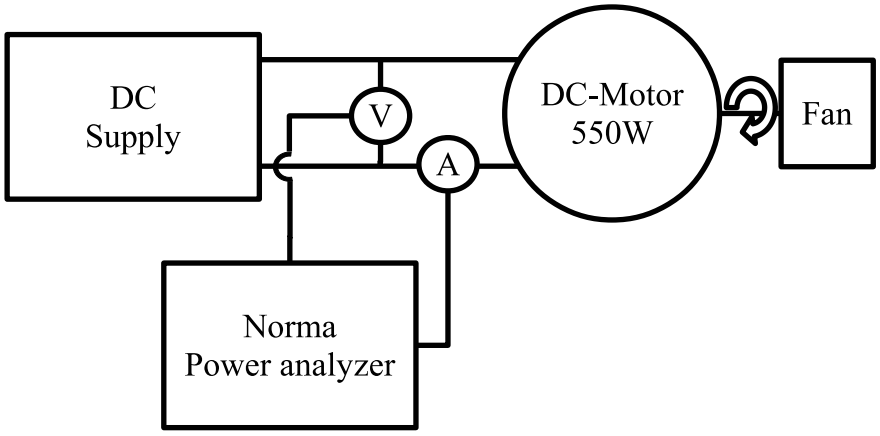

Figure D.5: Lab setup for fan loss measurement

The losses for the hybrid switched reluctance motor was measured with the fan load, as it can be seen in Fig. D.6. The power analyzer used for these experiments was the Norma D6100 wide band power analyzer and the waveforms and signals were recorded using a Tektronix TDS3014B oscilloscope. Rotational speed was found from the recorded current waveforms. When testing the position sensorless control, the encoder is not connected to the DSP, except for verification purposes. The schematics for the electronics can be seen in appendix E.

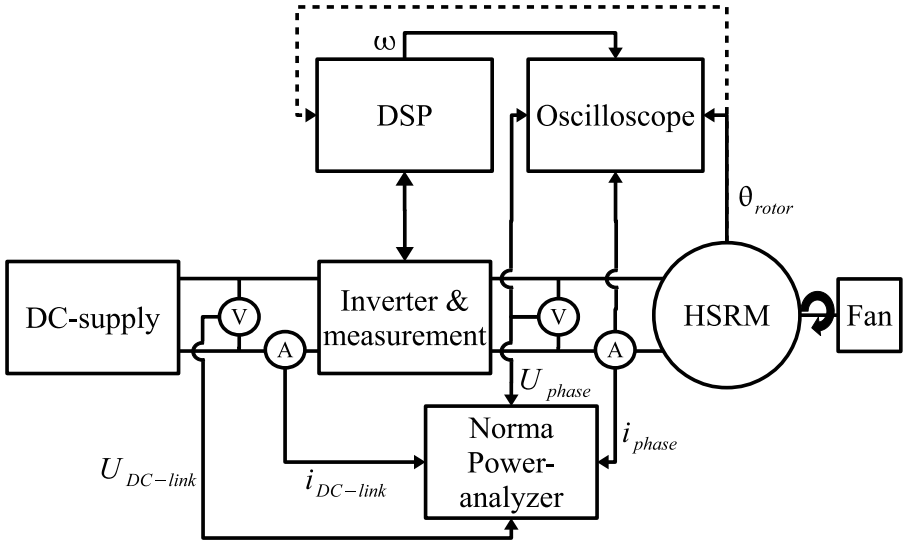

Figure D.6: The loss measurements were done using a Norma D6100 wide band power analyzer, and recorded on Tektronix TDS3014B oscilloscope.

Appendix E

Electronic schematics

The different boards were added to an EZDSP TMS320F2812 board, as they were needed. The TMS320F2812 microcontroller/DSP is running at a clock frequency of 150 MHz connected to a board with optical transmitters for optical transmission of the PWM signals for the inverter.

First a current measurement and encoder interface (See Fig. E.2) was added to enable motor control, together with an inverter (see Fig. E.1). The microcontroller has two separate channels to each of the two inverter MOSFETS. An over current protection circuit monitors a shunt resistor, and a D-latch shuts the inverter down until it is reset. The over current protection circuit is not using the sensor board current measurement, since that would not ensure isolation between the inverter and the microcontroller. As described in the thesis, a low cost implementation would not have such an isolation and probably also would not have a separate over-current protection.

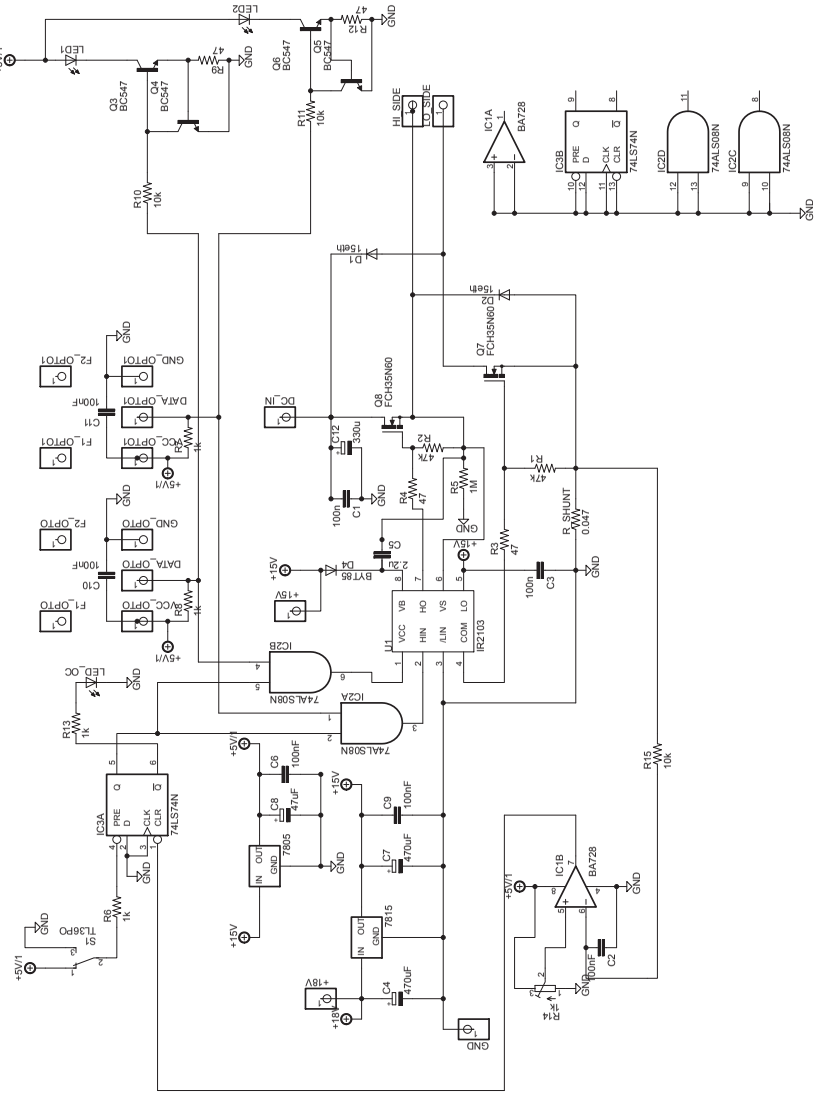
+5V/1
LED1
LED2
Q3 BC547
Q4 BC547
Q5 BC547
Q6 BC547
R9 47
R12 47
R10 10k
R11 10k
HI SIDE
LO SIDE
IC1A BA728
IC3B 74LS74N
IC2D 74LS08N
IC2C 74LS08N
GND
D1 15eth
D2 15eth
Q7 FCH35N60
Q8 FCH35N60
DC_IN
C12 330u
R2 47k
R1 2k7
47k
R4 47
R5 1M
C1 100n
C5 2n2
R3 47
R_SHUNT 0.047
C3 100n
+15V
BYT85 D4
U1 IR2103
VB HO VS VCC HIN /LIN COM LO
IC2B 74AL S08N
IC2A 74AL S08N
LED_OC
R13 1k
IC3A 74LS74N
PRE D CLK CLR Q /Q
C6 100nF
C8 47uF
C9 100nF
C7 470uF
7805
7815
C4 470uF
+18V
R15 10k
IC1B BA728
C2 100nF
R7 3k3
R6 1k
S1 TL36PO
C11 100nF
C10 100nF
R8 1k
R14 1k
F1_OPTO1
F2_OPTO1
F1_OPTO
F2_OPTO
GND_OPTO1
DATA_OPTO1
VCC_OPTO1
GND_OPTO
DATA_OPTO
VCC_OPTO
+5V/1

Figure E.1

The sensor board, shown in Fig. E.2 handles current measurement and interface with the encoder connected to the motor shaft. The current measurement is low pass filtered to remove switching noise, but a running average is also filtering the measurement, since the microcontroller ADC is sensitive to noise.

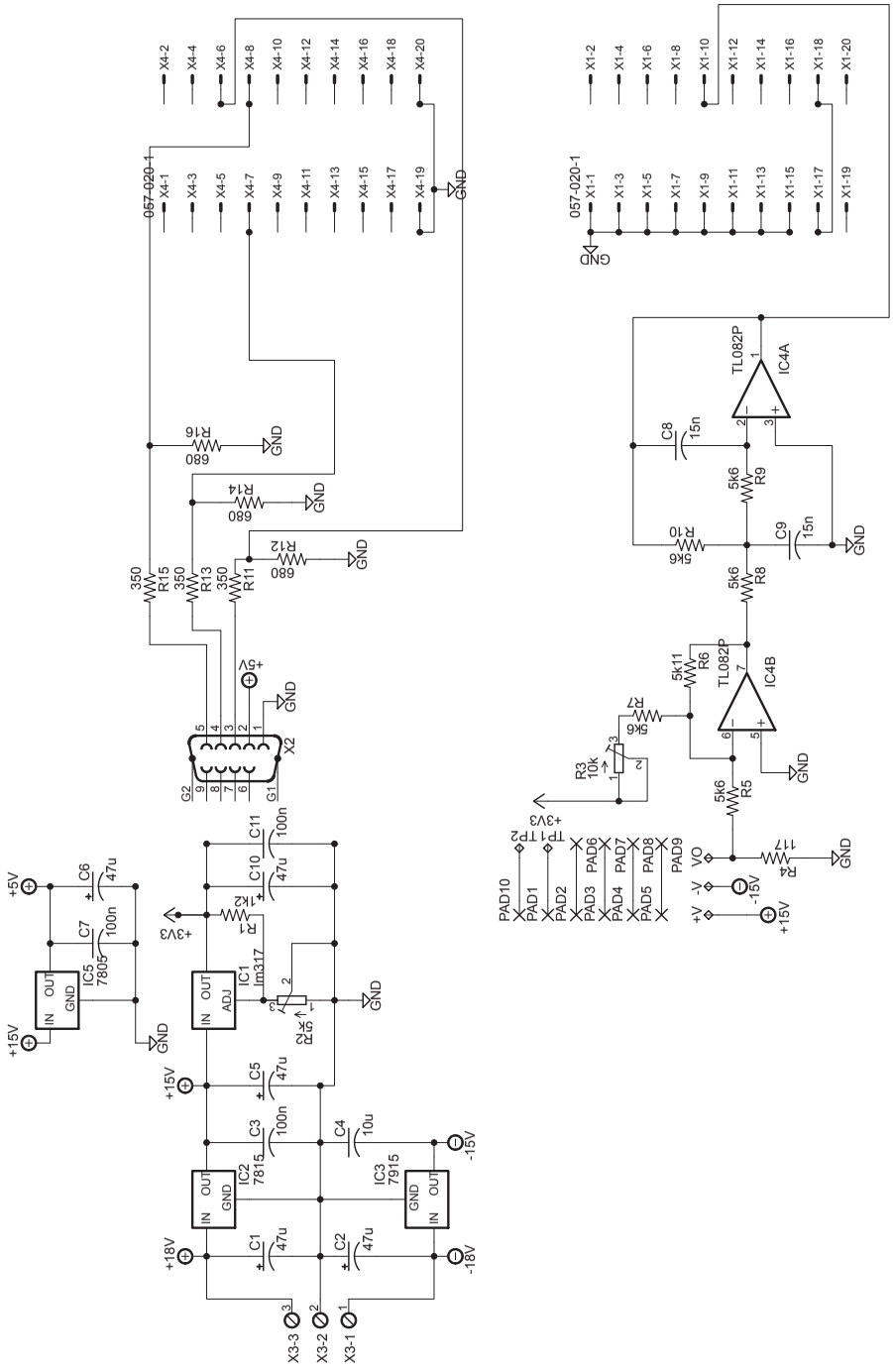

Figure E.2

To enable sensorless control an optically isolated differential measurement of the phase voltage was implemented as seen in Fig. E.3, and then connected to an ADC on the DSP through Fig. E.4.

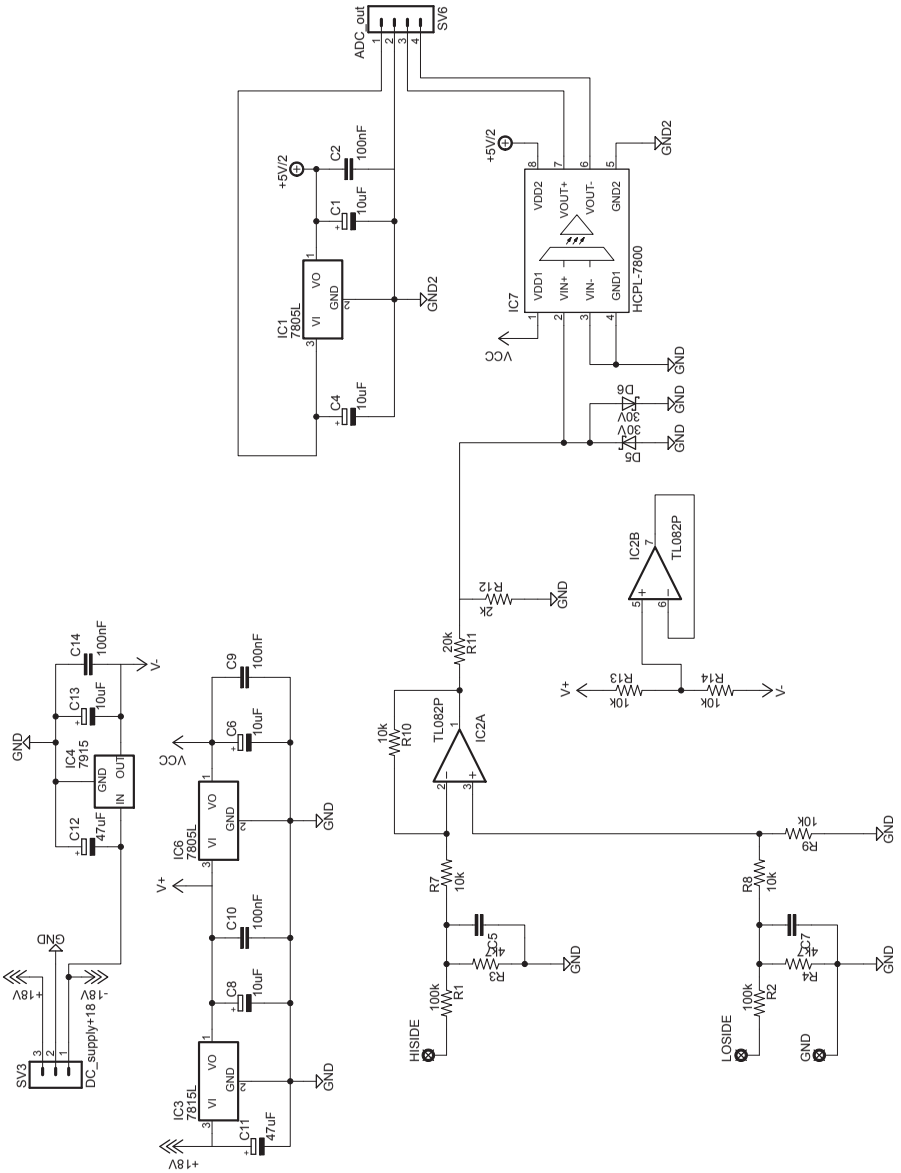

Figure E.3

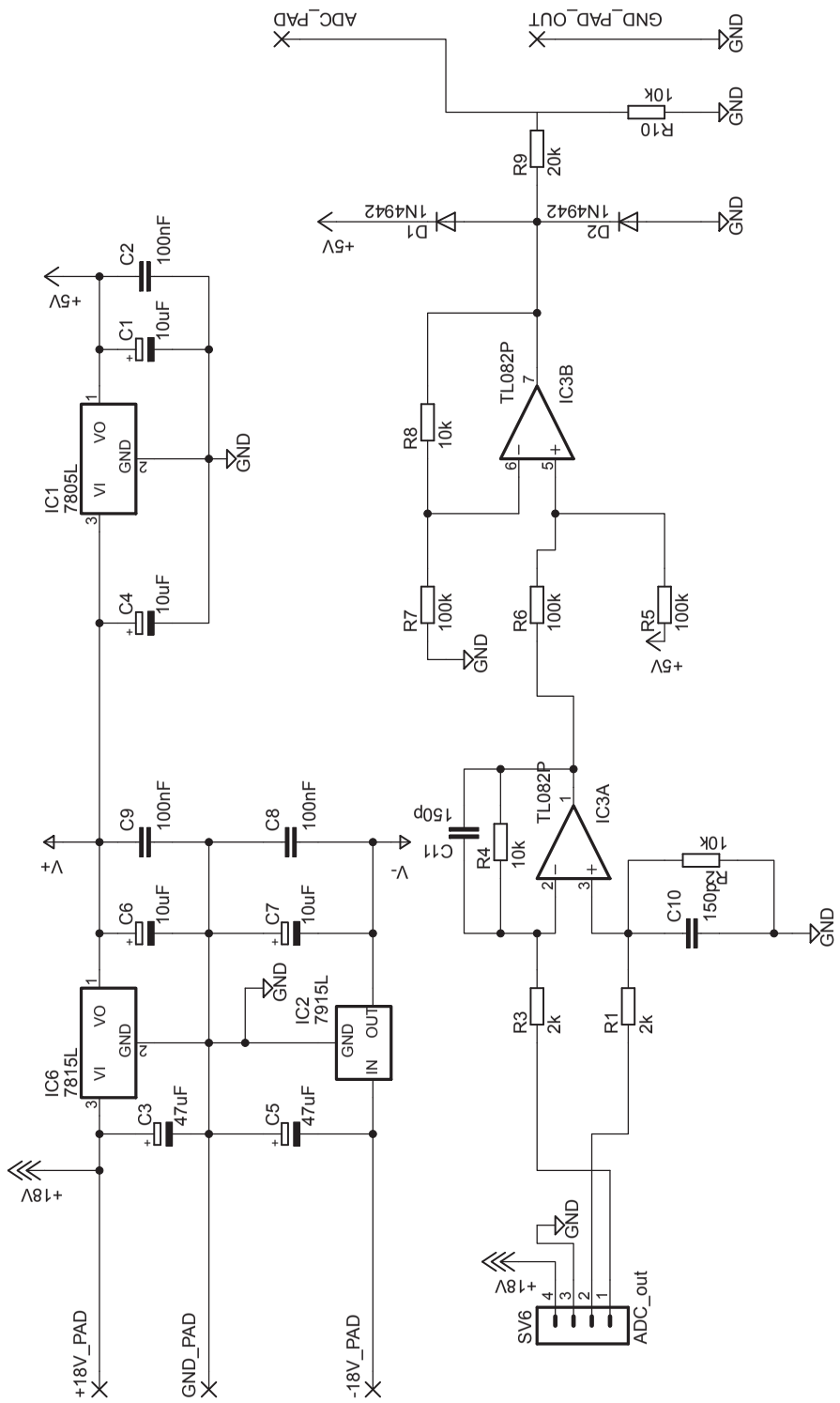
ADC_PAD
GND_PAD_OUT
GND
10k
R10
R9
20k
1N4942
D1
D2
+5V
C2
100nF
C1
10uF
IC1
7805L
VI
VO
GND
C4
10uF
R8
10k
TL082P
IC3B
R7
100k
R6
100k
R5
100k
C9
100nF
C8
100nF
C11
150p
R4
10k
IC3A
V+
V-
C6
10uF
C7
10uF
C10
150pF
IC2
7915L
IN
OUT
IC6
7815L
C3
47uF
C5
47uF
R3
2k
R1
2k
+18V
SV6
ADC_out
+18V_PAD
GND_PAD
-18V_PAD

Figure E.4

Appendix F

Sensorless state machine flowchart

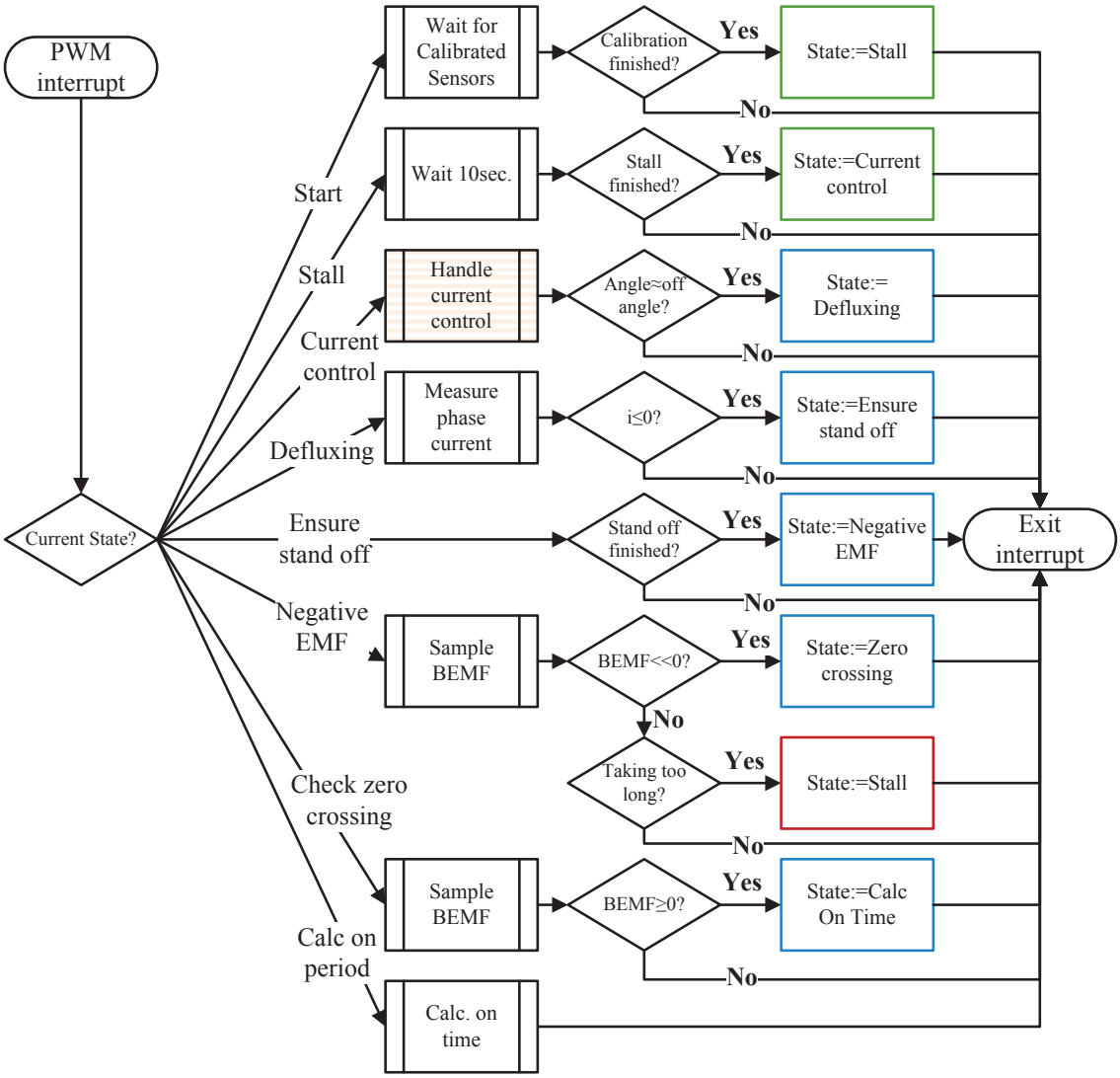
PWM interrupt
Current State?
Start
Stall
Current control
Defluxing
Ensure stand off
Negative EMF
Check zero crossing
Calc on period
Wait for Calibrated Sensors
Wait 10sec.
Handle current control
Measure phase current
Sample BEMF
Sample BEMF
Calc. on time
Calibration finished?
Stall finished?
Angle≈off angle?
i≤0?
Stand off finished?
BEMF<<0?
Taking too long?
BEMF≥0?
Yes
No
State:=Stall
State:=Current control
State:= Defluxing
State:=Ensure stand off
State:=Negative EMF
State:=Zero crossing
State:=Stall
State:=Calc On Time
Exit interrupt

Figure F.1

Appendix G

Softcore processor for FPGA

G.1 Introduction

To control an AC machine a DSP or a micro controller is typically used. While they are excellent, their architecture is not directly targeted for motor control, since they do not feature an instruction set dedicated to motor control. The micro controller is typically not sufficient for vector control schemes. For some applications even a fast DSP may be too slow, an example can be to replace an analog hysteresis controller as the inner control loop with a digital implementation. The FPGA has for some time been used for signal processing and the use of the FPGA for motor control has been explored before. There seems to be at least two different approaches used: [124] and [125] uses an approach based on signal flow. They implemented the control loop by making custom elements for each part. These elements are then connected to form the closed loop. [126] And [127] used a general purpose soft core connected to custom external elements needed for the control of a PMSM.

The signal flow approach, also known as dataflow processing, has a hardwired setup which requires synthesis of a new processor if the control loop is modified to accomodate e.g. sensorless control. This issue is addressed by using the more flexible approach of connecting external blocks to a general purpose soft core. However a general purpose softcore can be difficult to

modify, since most of them are either proprietary tied to a specific FPGA vendor or open source with limited documentation and test results. Furthermore having direct access to the softcore enables a more flexible hardware-software co-design, since everything inside the soft core can be changed to simplify or speed up the software algorithm. This paper presents a proposed new processor, which allows easy extension. Two different implementations are presented: one processor customized for a permanent magnet synchronous machine (PMSM) and another customized for a hybrid switched reultance machine (HSRM).

G.2 Design method for PMSM soft core instruction set

To design the soft core for the PMSM instance, first a quick evaluation of the instructions needed for vector control, also known as field oriented control (FOC). This section describes the thoughts regarding the instruction set design, the numerical format, custom instructions, and finally the peripheral functions.

Instructions needed for vector control

The key to vector oriented control for AC machines is the concept of rotating coordinate systems. In synchronous machines it can be advantageous to fix the coordinate system to the rotor. Update the control equations in this rotating reference frame (dq-reference frame), and transform back to the fixed stator coordinates ($\alpha\beta$ reference frame). To achieve this current measurement from the three phases needs to be sampled and transformed into the rotating reference frame. See G.1 for this transform. Assuming $0 = i_a + i_b + i_c$:

$$\begin{bmatrix} i_d \\ i_q \\ i_0 \end{bmatrix} = \frac{2}{3} \cdot \begin{bmatrix} \cos(\theta_e) & \cos\left(\theta_e - \frac{2\pi}{3}\right) & \cos\left(\theta_e - \frac{2\pi}{3}\right) \\ \sin(\theta_e) & \sin\left(\theta_e - \frac{2\pi}{3}\right) & \sin\left(\theta_e + \frac{2\pi}{3}\right) \\ \frac{1}{2} & \frac{1}{2} & \frac{1}{2} \end{bmatrix} \cdot \begin{bmatrix} i_a \\ i_b \\ i_c \end{bmatrix} \tag{G.1}$$

The control equations can be handled by signed multiplications and additions as shown in [128].

The angle of the voltage vector in the stator $\alpha\beta$ reference frame is given by:

$$\angle v_{\alpha\beta} = arctan(vq/vd) + \theta_e \tag{G.2}$$

The magnitude of the voltage vector in the stator $\alpha\beta$ reference frame:

$$|\vec{v}_{\alpha\beta}| = |\vec{v}_{dq}| = \sqrt{v_d^2 + v_q^2} \tag{G.3}$$

Finally this allows for generation of the PWM duty times using e.g. center based space vector modulation: Given a switch period T_s, $|\vec{v}_{\alpha\beta}|$, and $\angle v_{\alpha\beta}$:

$$\begin{aligned} t_a &= \frac{2\cdot\sqrt{3}}{\pi}\cdot|\vec{v}_{\alpha\beta}|\cdot T_s\cdot sin(\frac{\pi}{3} - \angle v_{\alpha\beta}) \\ t_b &= \frac{2\cdot\sqrt{3}}{\pi}\cdot|\vec{v}_{\alpha\beta}|\cdot T_s\cdot sin(\angle v_{\alpha\beta}) \\ t_0 &= t_7 = \frac{1}{2}(T_s - t_a - t_b) \end{aligned} \tag{G.4}$$

Equations G.1, G.2,G.3, and G.4 determines the operations needed for vector control. It is also clear that there is only need for signed operations.

G.3 Soft core Architecture

The soft core consists of four distinct modules and two multiplexers, as it is shown on figure G.1. A synchronous design is used for the soft-core, with two state machines governing the behaviour. One state machine is used for the control block and the other is for the algorithmic logic unit. Microcode is not used for control of soft core behaviour, but rather uses hardwired logic. The major task for the control block is control the program counter and to prohibit writes during compare instructions. The ALU performs all calculations and access to custom instructions and external blocks. The two multiplexers determine the source of the operands for the algorithmic and logic unit (ALU). The register bank contains control logic and storage for the four registers (R0,R1,R2, and R3). The memory block is a standard two port memory block, enabling a Harvard structure for the processor.

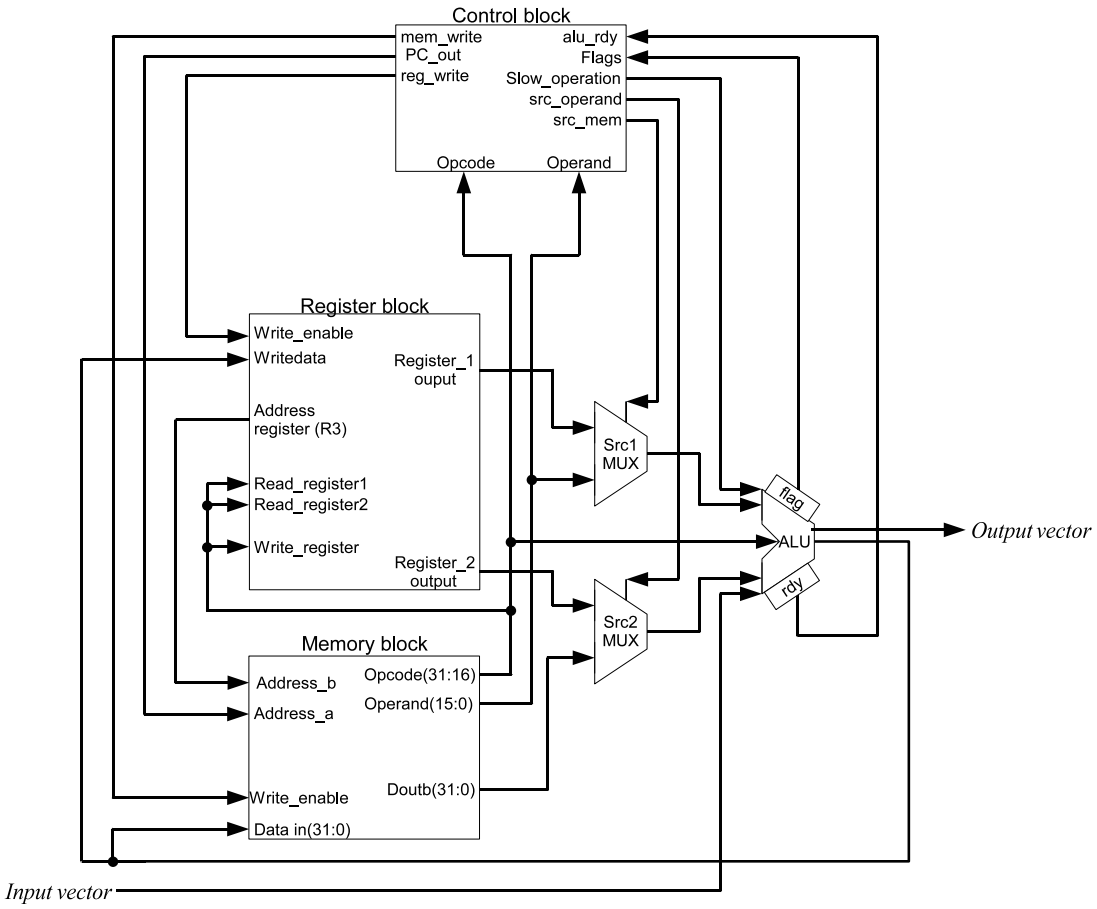

Figure G.1: The layout of the soft core.

G.4 instruction set

A custom instruction set is implemented to enable a simple mapping from the equations needed in AC-motor control to the actual machine code operations. The closer the instruction set is to the task, the fewer instructions are needed. This is balanced against the flexibility of implemented instructions and the speed of a complex instruction as well as the FPGA resource consumption of an instruction. To lessen the impact of complex instructions on the core structure of the processor, it was decided to enable the use of "external" instructions. Instructions which performed complex functions could then be tested separately and their influence on the soft core could be isolated. The mechanism for these custom instructions is described later but first a description of the design of the instruction set and the fixed point number format used in the soft core.

Design of instruction set

The functionality needed:

- Registers for intermediate values
- Timers with PWM output capability
- ADC-capabable input
- Quadrature decoder for rotor position
- Multiplication, addition and subtraction
- Cosine, sine, and rectangular to polar conversion

To enable design of more complex programs, logical functions (AND, OR, XOR), a compare, and conditional/unconditional branches were added. Finally two move instructions were added alongside three input/output instructions.

This leads to the set of instructions shown on table G.1.

There is eight different addressing modes for all three operand instructions, four addressing modes for all two operand instructions and two addressing modes for all one operand instructions.

Fixed point number format

Even though the soft-core is a 32 bit processor, the fixed point is set at 32768 for unity. This means to transform from decimal to to the fixed point format the following transform is needed:

$$number_{fixed} = number_{decimal} \cdot 32768 \tag{G.5}$$

Similarly for angles in degrees the transform is given as:

$$angle_{fixed} = angle_{degrees} \cdot 16384/180 \tag{G.6}$$

Table G.1: Instruction set of the proposed AC control processor.

Instruction	Meaning
ANG	Calculates angle of a 2D-vector
ABS	Calculates magnitude of a 2D-vector
COS	Cosine
SIN	Sine
PWM	Set PWM-timers, wait and return rotor-pos.
SCL	Fixed point multiplication
ADD	Addition
SUB	Subtraction
MUL	Integer multiplication
SWP	Swap upper and lower part of number
ORB	Logical OR
AND	Logical AND
XOR	Logical XOR
CMP	Compare two operands
Bxx	Conditional branch
JMP	Unconditional jump
MOV	Copy first operand
MVY	Copy second operand
LTC	Latch and roll input
OUT	Output masked value
INP	Input masked value

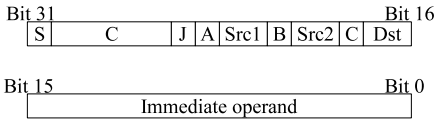

Figure G.2: The instructions all follow a single format with some bit patterns directly connected to e.g. multiplexers. Since no exception exist to this format, the control logic can be kept simple.

Instruction set format

There is only one format for instructions, which is shown on figure G.2

J is one:

This is a jump/branch command, and the immediate operand is copied to the program counter (PC) if the branch is taken. The command indicates the type of branching.

J is zero:

If S is 1 this is a slow operation. This is described in the section regarding custom instructions. The command field indicates the type of operation to be performed.

A is zero:

The register defined by Reg1 is used as first source for instructions.

A is one:

The immediate operand is used as first source for instructions.

B is zero:

The register defined by Reg2 is used as second source for instructions.

B is one:

The memory content indirectly indicated by R3 is used as second source for instructions.

C is zero:

The register defined by Dest is used as destination.

C is one:

The memory content indirectly indicated by R3 is used as destination.

Custom Instructions

To enable custom instructions a simple strategy was used. Bit 31 tells the state machines of the soft core, that a slow operation is to be performed. And slow is here defined as more than 3 cycles for completion. The control block will then wait for the ALU to finish. The ALU would wait for the external function to finish, latch in the result and allow the control block to continue. So the processor is effectively stalled when a custom instruction is executing. The state-machines implementing this behaviour can be seen on figure G.4 and figure G.3

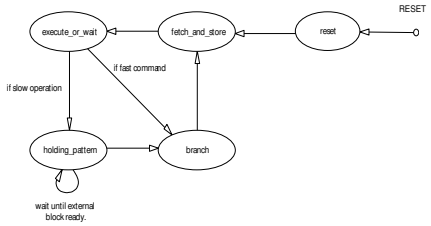

Figure G.3: The control block state machine.

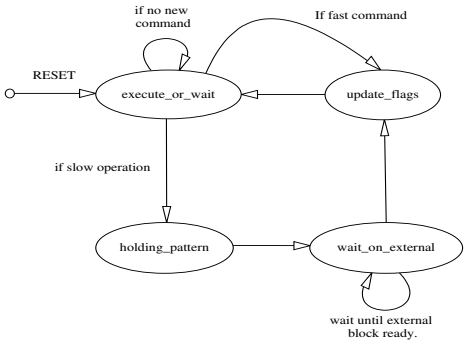

Figure G.4: The ALU block state machine.

This is also used to implement synchronization with PWM timers. The PWM instruction waits for the timer A to reach zero before it latches the rotor position and allows the ALU to continue.

CORDIC functions

To approximate the sine, cosine and the rectangular to polar functions a coordinate rotation digital computer (CORDIC) was implemented. CORDIC was chosen for the implementation since it is simple to implement and hardware efficient [129]. The implemented CORDIC functions are accurate to approximately 12 bits. This number is the result of simulation of all combinations of inputs. The only exception is the angle calculation which only is accurate to the same number bits as the input vector values. Thus the shorter vector, the greater the inaccuracy in the calculation of the vector angle. This is an inherent feature of the CORDIC functions. To ensure that the results are usable in all four quadrants of operation, extra rotations are done after the actual CORDIC operations. Compensation for the CORDIC expansion factor is done before the CORDIC approximations. A complete discussion of CORDIC can be found in [130]

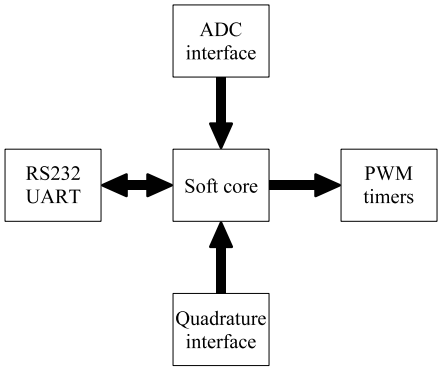

Figure G.5: The peripheral connections with the soft core.

Peripheral functions

The peripheral blocks are arranged in a typical system on a chip layout as shown on figurefig:soc

PWM timers:

To control the three phase inverter three identical PWM timers are instantiated. The PWM command sets the duty cycles for the three timers. They are implemented as timers with a fixed period, constantly counting up and down to enable classical SVM.

Quadrature decoder:

To get the rotor position a quadrature interface was implemented. The PWM command returns the current encoder value.

ADC interface:

Since the FPGA used has no ADC internally, an external SPI interface was implemented. The communication is achieved by the two commands OUT and LTC.

RS232 UART:

To make a simpler interface to the assembler an UART for RS232 was implemented. The use of the UART for programming is described in the section regarding the programming tools.

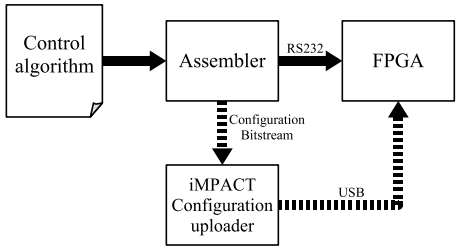

Figure G.6: The FPGA can be initialised from the assembler by uploading a preconfigured bit stream to the FPGA as indicated by the dashed line. The assembler control algorithm can then be uploaded to the soft core as indicated by the black line.

G.5 Programming Tools

A basic assembler was designed with an integrated editor. The assembled machine code program can be uploaded to the soft core using the assembler RS232 interface on the PC-side and a simple download program in the soft core. A download monitor program is contained in the synthesized image uploaded to the FPGA. That way a faster edit-assemble-debug cycle is possible. The upload of the synthesized image can also be performed from the assembler and effectively acts as a reset of the soft core. The programming model is shown on figure G.6.

G.6 Implementation results

PMSM instance with Software Logic for the ADC

For the PMSM the soft-core is kept as presented in the article, and the current loops are implemented in a synchronous reference frame. The loop times for the current loop is measured in a VHDL simulation is presented in table G.2, and will differ slightly if an overflow needs to be handled by the integrator part of the PI-control. A loop time for a complete FOC of 71127 ns, is more than 10 times slower than the 5400 ns presented in [124]. But most of this is due the fact that this is a sequential implementation and the CORDIC functions are not optimized. This is partly due to the fact that this is a sequential implementation and the CORDIC functions are

Table G.2: Times for a vector control loop (FOC). The times are given using a 50 MHz clock.

Functional element	Time in nanoseconds
Get measurements from ADC	38178
Transform to dq reference frame	11277
Control updates	8117
Transfrom to $\alpha\beta$	5246
SVM	8309
Complete FOC	71127

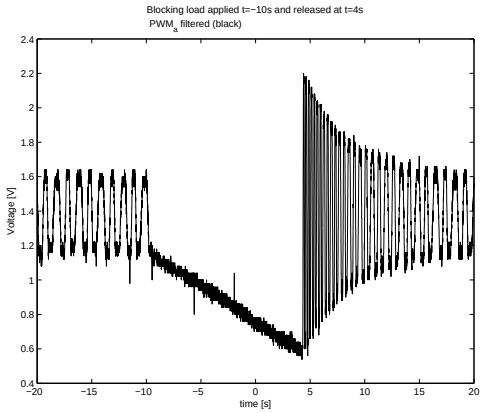

Figure G.7: The proportional part of the PI-speed controller is disabled and a blocking load is applied. The response on one of the phase voltages is measured using the low pass filtered signal to the inverter stage.

not optimized, but first and foremost because the ADC SPI input was implemented in assembler and not VHDL. The entire system for a PMSM consumes 35% of the resources in a Spartan 3E FPGA (xc3s500e-5fg320). See table G.2 for details. The details regarding resource usage is presented in table G.4 under ”CCPU/PMSMM, SW-ADC”.

PMSM instance with Hardware Logic for the ADC

For the PMSM the soft-core is kept as presented in the article, and the current loops are implemented in a synchronous reference frame. The loop times for the current loop is measured in a VHDL simulation is presented in table G.2, and will differ slightly if an overflow needs to be handled by the integrator part of the PI-control. A loop time for a complete FOC of 71127 ns, is

Table G.3: Times for a vector control loop (FOC) using extra logic for control af ADC. The times are given using a 50 MHz clock.

Functional element	Time in nanoseconds
Get measurements from ADC	120
Transform to dq reference frame	11277
Control updates	8117
Transfrom to $\alpha\beta$	5246
SVM	8309
Complete FOC	33249

more than 10 times slower than the 5400 ns presented in [124]. But most of this is due the fact that this is a sequential implementation and the CORDIC functions are not optimized. The entire system for a PMSM consumes 37% of the resources in a Spartan 3E FPGA (xc3s500e-5fg320). See table G.3 for details. The details regarding resource usage is presented in table G.4 under ”CCPU/PMSMM, HW-ADC”.

HSRM instance

For the single phase HSRM only a very simple voltage control is implemented. The loop time of 981 ns is therefore also much lower. The commands COS, SIN, ABS and ANG are removed from the soft core and the resource usage drops to 14% in the same Spartan 3E FPGA (xc3s500e-5fg320). The timers are updated so they can perform soft-switching with a minimal effort from the program. In soft-switching, the asymmetrical halfbridge switches are controlled independently allowing for zero voltage vectors. By embedding this control in the hardware and updating the PWM command, the assembler control loop can be kept simple. The details regarding resource usage is presented in table G.4 under ”CCPU/HSRM, SW-ADC”.

The current and voltage waveforms can be seen on figure G.8

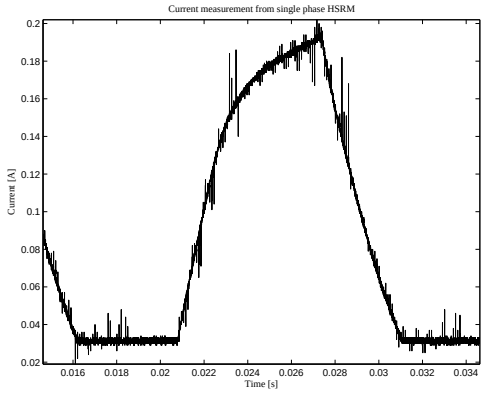

Figure G.8: The current measured for the single phase HSRM under voltage control.

Table G.4: Comparative table regarding resource usage, using a Spartan-3E C3S500E-5 FPGA at 50 MHz, with 20 blocks of on chip RAM, 4656 slices of logic and a total of 20 hardware multipliers (HW-mul.). All implementations were compiled using Xilinx WEB-ISE 9.1I VHDL compiler with a mixture of behavioural and register transfer logic.

Type	Slices used	Mem used	HW-mul used
CCPU/PMSM, SW-ADC	1629	8	4
CCPU/PMSM, HW-ADC	1718	8	4
CCPU/HSRM, SW-ADC	691	8	1

G.7 Conclusion

This paper presents a new processor for motor control and discusses the design and implementation of such a processor in three different forms. The three instantiations, demonstrates that the custom soft-core can be used for different types of motor control. By allowing for easy modifications various control requirements can be accommodated. This enables a wider range of control strategies without redesign of the synthesized image on the FPGA unlike signal flow methods, yet it maintains a decent speed on a small FPGA since the soft-core is design for AC motor control.

Future work

- The assembler should choose between different predefined soft-cores to minimize the use FPGA resources.
- A compiler should be developed to generate the assembly language code. A simple compiler is currently in the works.
- A simulator should help decide whether a functionality should be implemented as a hardware function or the functionality could be implemented as software.

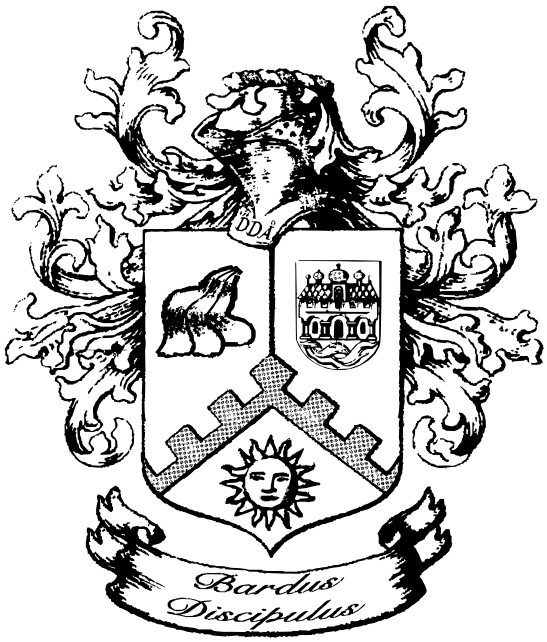
DDA
Bardus
Discipulus